

LIBRARY Michigan State University

This is to certify that the dissertation entitled

SPINTRONICS WITH METALS: CURRENT PERPENDICULAR-TO-THE-PLANE MAGNETO-TRANSPORT STUDIES IN METALLIC MULTILAYERS AND NANOPILLARS

presented by

Amit Sharma

has been accepted towards fulfillment of the requirements for the

PhD	degree in	Physics
		Ban
	Major Profe	ssor's Signature
		9/08
		Date

MSU is an Affirmative Action/Equal Opportunity Employer

PLACE IN RETURN BOX to remove this checkout from your record.

TO AVOID FINES return on or before date due.

MAY BE RECALLED with earlier due date if requested.

DATE DUE	DATE DUE	DATE DUE

5/08 K:/Proj/Acc&Pres/CIRC/DateDue.indd

SPINTRONICS WITH METALS: CURRENT PERPENDICULAR-TO-THE-PLANE MAGNETO-TRANSPORT STUDIES IN METALLIC MULTILAYERS AND NANOPILLARS

 $\mathbf{B}\mathbf{y}$

Amit Sharma

A DISSERTATION

Submitted to
Michigan State University
in partial fulfillment of the requirements
for the Degree of

DOCTOR OF PHILOSOPHY

Physics

2008

ABSTRACT

SPINTRONICS WITH METALS: CURRENT PERPENDICULAR-TO-THE-PLANE MAGNETO-TRANSPORT STUDIES IN METALLIC MULTILAYERS AND NANOPILLARS

By

Amit Sharma

In this thesis, we present studies to produce new information about three topics: current perpendicular to the plane magnetoresistance (CPP-MR), spin transfer torque (STT), and antiferromagnetic spintronics.

Large values of CPP-MR interface parameters - - specific interface resistance (Area times resistance), $2AR^*$, and scattering asymmetry, γ - - are desirable for the use of CPP-MR in devices. Stimulated by a nanopillar study by the Cornell Group, we first discovered that Py/Al had an unusually large $2AR^*$, but a small γ . In the hope of finding metal pairs with large values of both the interface parameters, the Py/Al studies led us to study the following interfaces: (a) F/Al with F: Py (= Ni₈₄Fe₁₆), Co, Fe, Co₉₁Fe₉, and (b) F/N: Py/Pd, Fe/V, Fe/Nb and Co/Pt. None of the metal pairs looks better for CPP-MR devices.

The Cornell group also found that bracketing Al with thin Cu in Py/Al/Py nanopillars, gave an MR similar to Py/Al/Py rather than to Py/Cu/Py. To try to understand this result, we studied the effect of Cu/Al/Cu spacers on $A\Delta R = AR(AP) - AR(P)$ of Py exchange biased spin valves (EBSVs). Here AR(AP) and AR(P) are the specific resistances in the anti-parallel (AP) and parallel (P) configurations of the F layers.

Intriguingly, fixing the Al thickness $\mathbf{t}_{Al}=10$ nm and varying \mathbf{t}_{Cu} has no effect on A Δ R, but fixing $\mathbf{t}_{Cu}=10$ nm and varying \mathbf{t}_{Al} significantly affected A Δ R. These unusual behaviors are probably due to strong Al and Cu intermixing, with probable formation of some fraction of ordered alloys.

Recent calculations predicted that 2AR of Al/Ag interfaces would vary substantially with orientation and with alloying. The latter is a special potential problem, because Al and Ag interdiffuse at room temperature. To compare with the calculations, we determined 2AR of sputtered Al/Ag interfaces with (111) orientation. Our estimate agrees with calculations that assume 4 monolayers of interfacial disorder, consistent with modest intermixing

To aid in understanding the physics underlying spin transfer torque in F/N/F trilayers, we devised a simple test, where we change the transport properties of only the N-spacer from ballistic to diffusive. To try to minimize effects of systematic errors, we compare ratios of results for diffusive and ballistic transport with calculations. The ratios disagree with predictions of those models that were expected to be most reliable.

Recently, it was predicted that spintronics effects: magnetoresistance, and spin transfer torque induced magnetization switching, should be observable in systems where ferromagnets are replaced by antiferromagnets. We have done the first experiments to search for those predicted antiferromagnetic spintronics effects. We find effects of large current densities on exchange bias, but no clear evidence for antiferromagnetic giant magnetoresistance.

COPYRIGHT

AMIT SHARMA

2008

To,

 $Alok\ Sharma$

My brother, friend and mentor

ACKNOWLEDGEMENTS

It is a great pleasure to acknowledge all who have helped me throughout the graduate program. Firstly, I would like to acknowledge my advisors Prof. Jack Bass and Prof. William P. Pratt Jr. for their excellent support and guidance. I owe them for teaching me the art and science of scientific experimentation and writing. I have really enjoyed working with them.

I would like to thank Dr. Reza Loloee for teaching me many techniques and helping me numerous times, always with a smile. My special thanks to Dr. Nikoleta Theodoropoulou, with whom I have worked on many projects. I acknowledge the help and support of Dr. B. Bi on micro-fabrication.

My sincere thanks to Z. Wei, J. Basset and Prof. M. Tsoi, at University of Texas, Austin, for the collaborative work on antiferromagnets. I thank Dr. A. S. Nunez, Dr. P. M. Haney, Dr. R. A. Duine and Prof. A. H. MacDonald for collaborating for theory on the antiferromagnet projects. I also thank Dr. M. Stiles and Dr. J. Xiao, for collaborating on the ballistic vs. diffusive project. My sincere thanks to Prof. A. Fert and Dr. H. Jaffres, for collaborating on Py/Al project. I thank T. Haillard, J. A. Romero, and R. Acharyya for collaborating on the F/Al and F/N projects. I would like to thank Prof. M. Crimp and Dr. J. Zhang at Michigan State University, and Prof. D. Cullen and Prof. D. Smith at Arizona State University, for the structural studies. Thanks to Prof. N. Birge for encouraging me to organize the Labview course. Thanks to Prof. S. D. Mahanti for his help throughout the program.

My special thanks to the secretaries - - Debbie, Kim, Lisa and Cathy, for helping

me numerous times. I thank the machine shop and the electronic shop for their support. My thanks to NSF through grants DMR 05-01013 and DMR 08-04126, Seagate Technology, CSM, and KMF for supporting me throughout the program.

I thank all my colleagues and friends, both here and in India, who have been a constant source of encouragement and motivation. Lastly I would like to thank my parents, my siblings, and my wife for their constant love, care and support.

Contents

Ll	ST (OF TA	BLES
LI	ST (OF FIG	GURES xi
1	Intr	oducti	ion
	1.1	Spintr	ronics
	1.2	Backg	round
		1.2.1	Spin Dependent Transport
		1.2.2	Giant Magnetoresistance (GMR)
			1.2.2.1 Current geometries and effect on MR
			1.2.2.2 Simple 2 current model of GMR
		1.2.3	Control of magnetic order
	1.3		nt perpendicular to the plane magnetoresistance : Parameters
	_,,		neir prior values
	1.4		ransfer torque (STT)
	1.5		erromagnetic Spintronics
	1.6		Thesis
	1.0	1.6.1	CPP-MR studies
		1.6.2	Spin transfer torque studies
		1.6.3	Antiferromagnetic spintronics studies
		1.6.4	-
		1.0.4	Conclusions
2	Cur	rent p	perpendicular to the plane magneto-transport studies in
		_	nultilayers
	2.1		MR Samples
		2.1.1	Fabrication, Processing & Measurement
		2.1.2	Types of samples
	2.2		MR: Models and equations
		2.2.1	Two current series resistor model (2CSR) No Spin relaxation
			in the layers and no spin flipping at the interfaces
		2.2.2	Valet-Fert (VF) model Including spin relaxation in the layers,
		2.2.2	and sometimes spin flipping at the interfaces
	2.3	Exper	riments involving Non-magnetic metal (N1) / Non-magnetic metal
	2.0		interfaces
		2.3.1	
		2.0.1	2.3.1.1 Introduction
			2.3.1.2 Experiment
			Z.J.I.Z Experiment

			2.3.1.3	Results	45
			2.3.1.4	Conclusions	46
		2.3.2	Specific	interface resistance of sputtered Al/Cu interfaces	47
			2.3.2.1	Introduction	47
			2.3.2.2	Experiment	47
			2.3.2.3	Results	55
			2.3.2.4	Conclusions	57
	2.4	Exper	iments in	volving Ferromagnetic / Non-magnetic metal interfaces	59
		2.4.1	-	resistance and scattering asymmetry parameter of F/Al	
				es $(F:Py (= Ni_{84}Fe_{16}), Co, Fe \& Co_{91}Fe_{9}) \dots$	61
			2.4.1.1	Introduction	61
			2.4.1.2	Experiment	62
			2.4.1.3	Results	62
			2.4.1.4	Conclusions	70
		2.4.2	_	resistance and scattering asymmetry parameter of Py/Pd	l,
				e/Nb, and Co/Pt interfaces	72
			2.4.2.1	Introduction	72
			2.4.2.2	Experiment	73
			2.4.2.3	Analysis	74
			2.4.2.4	Results	78
			2.4.2.5	Conclusions	79
		2.4.3		f Cu/Al/Cu sandwiches on the magnetoresistance of Py	
			_	e biased spin valves	81
			2.4.3.1	Introduction	81
			2.4.3.2	Experiment	81
			2.4.3.3	Interpretation of the data	82
			2.4.3.4	Conclusions	84
3	Spir		-	ue studies	85
	3.1			transfer torque (STT)	86
	3.2		-	apple fabrication and measurement	92
		3.2.1	_	llar fabrication process	93
		3.2.2		llar Measurement	101
	3.3			allistic vs. diffusive transport in the N layer	103
		3.3.1		n of N metals	103
		3.3.2		ters	104
		3.3.3		s and Data	105
		3.3.4		or systematic errors	109
		3.3.5			111
		3.3.6		tions	111
		3.3.7		of uncertainties	113
	3.4	Summ	ary		114
4	Ant		_	spintronics studies	116
	4.1	Exch	ange Bias	3	117

4.2	Theoretical predictions	119
4.3	AFM samples and measurement	121
4.4	Experiments to study the effect of current on exchange bias	123
	4.4.1 AFM= FeMn (= $Fe_{50}Mn_{50}$), F = CoFe (= $Co_{91}Fe_{9}$)	123
	4.4.2 AFM=IrMn (= $Ir_{20}Mn_{80}$), F = CoFe (= $Co_{91}Fe_{9}$)	126
	4.4.3 AFM=FeMn (= $Fe_{50}Mn_{50}$) and IrMn (= $Ir_{20}Mn_{80}$),	
	$F = Py (=Ni_{84}Mn_{16}) \dots \dots \dots \dots \dots \dots \dots \dots \dots$	127
	4.4.4 Effect of current on exchange bias Analysis	129
4.5	f	
	effects (AGMR)	133
	· · · · · · · · · · · · · · · · · · ·	137
4.6	Summary	138
5 Co	nclusions	141
A .		146
A.1	Van der Pauw resistivity measurement	146
A.2	Estimates of diffusion distances of various metals in Al and vice-versa	148
A.3	Estimating $2AR_{Nb/Fe}$ and ρ_{Fe} by the CPP technique	150
	Recipe for optical lithography	151
A.5	Recipe for e-beam lithography	152

List of Tables

1.1	Reference values from old estimates of resistivity (ρ_{old}) , spin diffusion length (l_{sf}) , and bulk asymmetry parameter (β) , for metals used in the present study. Except for the resistivities of Nb and V, all the other values were determined at 4.2 K. Since Nb and V are superconductors at 4.2 K, their resistivities were measured at 12 K	14
1.2	$2AR(exp)$ versus rounded no-adjustable-parameter calculations for close packed interfacial layers. $2AR$ (Perfect) represents a perfect interface and $2AR(2 \text{ monolayer disorder})$ represents an interface with two monolayers randomly mixed 50-50. For Co/Cu and Fe/Cr, the experimental values represent $2AR^*$. The values listed above (below) the double line are for lattice matched metal pairs with $\Delta a/a < (>)1\%$. Except for Pd/Pt, the values are taken from ref [59]. The values of Pd/Pt are taken from ref [48].	16
1.3	Calculated specific interface resistance of Al/Ag. The third column lists the values for perfect interfaces and the fourth column lists the values with interface disorder modeled as two layers of a 50-50 alloy in 10 x 10 lateral supercells. The table is after Ref. [60]	16
2.1	Van der Pauw resistivities of sputtered Al and Cu multilayers with atomic $\%$ similar to Al ₂ Cu and AlCu ₃ . In some cases, only a single sample has been processed at different temperature and time. In others, multiple samples have been processed similarly. In the latter case, the specified uncertainities are the standard deviation of measurements.	49
2.2	The structure, measured resistivity (ρ_{new}) , and earlier estimates of resistivity, ρ_{old} , for metals used in the present study. The residual resistivities of V and Nb were measured at 12K and all others were measured at 4.2K. For Co, one of the samples gave $\rho_{Co} = 230 \text{ n}\Omega\text{m}$, but the surface was mottled, leading us to neglect it. For Fe, we did CIP measurements and an independent CPP based estimation (see text); the values and uncertainties listed are the average of both measuring techniques. For Co/Pt analysis, we use the ρ_{Pt} (and corresponding l_{sf}) from [48], which is within mutual uncertainties of our new measurement, but smaller than the values in [45]	60
	surement, but smaller than the values in [45]	υU

2.3	Our estimates of renormalized interface specific resistance (2AR*), and scattering asymmetry parameter (γ), for F/Al interfaces. The values for Co/Al (b) were estimated by taking spin flipping (with spin flip parameter $\delta_{F/Al}=1.8\pm0.5$) into account (see text for details). For comparison, we also show values for Py/Cu	70
2.4	Our estimates of values of $\gamma_{F/N}$, $2AR_{F/N}^*$, and the product $\gamma_{F/N}2AR_F^*$ for Co/Pt, Py/Pd, Fe/V and Fe/Nb interfaces. For comparison we also list the corresponding parameters for $Co_{91}Fe_{9}/Al$ and Py/Cu. The difference between the values for Fe/Nb (a) and (b) are explained in the text	F/N 79
3.1	The resistivity (ρ) , mean free path (λ) and spin diffusion lengths (l_{sf}) for Cu and CuGe at 295 and 4.2 K. We also list the ratios $\mathbf{r} = \lambda/10\mathrm{nm}$ and $\mathbf{r}^* = l_{sf}/10\mathrm{nm}$ for reference.	104
3.2	The values from a joint data set (see text). The numbers in the brackets show the number of samples. The $Cu(7)$ and $CuGe(6)$ samples gave good switching at both 295 K and 4.2 K. The remaining samples gave good switching only at 295 K. The uncertainties are twice the standard deviation of the mean. The table is after [110, 111]	110
3.3	The subset data for my samples only. The numbers in the brackets show the number of samples. The Cu(3) and CuGe(2) samples gave good switching at both 295 K and 4.2 K. The uncertainties are twice the standard deviation of the mean	110
3.4	Calculated estimates of $X = \Delta I_{CuGe}/\Delta I_{Cu}$ and I_c^+/I_c^- for Cu and CuGe samples. The calculations based on the Ballistic Slonczewski model are for: (a) no spin flipping, and (b) with spin flipping. For comparison we also list in bold the estimates from our experiments based on the joint data set. The data listed in this table are taken from Refs. [110, 111]	112
A.1	Our estimates of diffusion distances $d(nm)$ for $t=1$ min and $t=1$ week at both 300 K and 450 K for dilute concentrations of various metals in Al and vice versa	148

List of Figures

4	The sign convention we will follow \uparrow = Moment of the electron is along the moment of the ferromagnet. \downarrow = Moment of the electron is opposite to the moment of the ferromagnet	1.1
5	A schematic drawing of R versus H curve for $(Fe(30 \text{ Å})/Cr(9\text{Å}))_{60}$ multilayers, measured at 4.2 K. The figure is after [5]	l. 2
6	CPP-MR/CIP-MR ratio for Co/Ag multilayers showing CPP-MR is much greater than CIP-MR (after figure 3, ref [30]). The inset shows the CPP and CIP current directions in a metallic multilayer	1.3
8	Two F layers in the parallel and antiparallel orientations. The dashed lines show how electrons with moments along or opposite to the local magnetization are scattered as they traverse the layers.	l. 4
9	The layers with arrows denote ferromagnets with moments pointing in the direction of the arrows. The thin layer in between is the N layer. The top figure represents an anti-parallel configuration and the bottom figure shows the parallel configuration after a high magnetic field is applied	1.5
10	AR vs. H plot for a typical F/N multilayer sample. The low resistance at saturating fields corresponds to the parallel (P) state. The maximum resistance is for the as-grown state, which has been argued to most closely approximate the anti-parallel (AP) state. Sweeping fields back from saturation gives intermediate maximum of resistance	1.6
11	AR vs. H plot for a typical EBSV sample, showing clear parallel and anti-parallel states. A Δ R is also shown.	l. 7
13	A cartoon showing a 'qualitative' model of spin diffusion length(l_{sf}) the mean distance electrons diffuse between spin-flipping collisions. The exact representation of l_{sf} is as given in equations 1.2 and 1.3. The hollow arrows represent 'mean free paths' the mean distance electrons travel between scattering events. The sum of all the hollow arrows represents the mean distance an electron travels before flipping its spin spin flip length (λ_{sf})	1.8

1.9	A cartoon showing the spin transfer torque and damping for a ferromagnet (free layer) with moment M_2 . The direction of the spin transfer torque depends on the direction of the current. H sets the direction of the moment of the polarizing 'fixed' ferromagnet	19
2.1	The left figure is a mask used to deposit CPP samples. The CPP substrate holder can accommodate 1 substrate and the mask is changed from position (1) the closed position, where the substrate is not exposed, to positions (2)-(4) to deposit the superconducting crossed strips and the multilayers. The figure on the right shows a CIP mask. The CIP substrate holder can accommodate 2 substrates. The mask is rotated to bring the open position (shown as position (2)), over position (1) to expose one substrate. After the deposition, the open position is brought over position (4) to close the substrates. To deposit the second substrate, the open position is moved over position (3). After the deposition, the open position is brought back over position (2) to close the substrates	26
2.2	A cartoon showing uniform current density in our samples where the thickness of the multilayer is much smaller than the widths of the Nb strips	27
2.3	The left figure is an optical image of the sample used for CPP measurements. The right figure shows the profile of typical superconducting crossed strip, measured by a Dektak profilometer, that is used to compute the area through which the CPP current flows	29
2.4	A schematic drawing of the ultra sensitive superconducting quantum interference device (SQUID) based potentiometer bridge circuit that we use to measure the resistance of our CPP samples	30
2.5	AR vs. H plot for a typical N1/N2 multilayer sample	32
2.6	X-ray diffraction patterns for: (a) Ag, (b) Al, (c) and (d) Al/Ag bilayers (n = 60)	41
2.7	${\rm AR}^T$ vs. n for Al/Ag Multilayers. The different symbols denote different sputtering runs. The filled symbols are initial measurements and the open symbols are measurements after significant time (~ 2 years).	45
2.8	X-ray diffraction pattern for an Al/Cu multilayer sample with $n=60$.	48
2.9	X-ray diffraction of a multilayer with very thin Al and Cu layer in an attempt to make an Al ₂ Cu (thin) sample. The dashed curve is the diffraction pattern after annealing at 450 K for 1 min.	51

2.10	X-ray diffraction of a multilayer with very thin Al and Cu layer in an attempt to make an AlCu ₃ (thin) sample. The dashed curve is the diffraction pattern after annealing at 450 K for 1 min	52
2.11	Plot of AR against n for: (a) Multilayer samples, and (b) Multilayer in EBSV samples	55
2.12	Plot of A Δ R against n for multilayer in EBSV samples	56
2.13	(a) $AR(AP) \approx AR^{\circ}$ (the maximum resistance for the as-sputtered state) against n for F/Al (F=Py, Co, CoFe(=Co ₉₁ Fe ₉), Fe) multilayers. The straight lines are fits to the data. The Py/Cu data (filled circles) are shown for comparison. (b) AR vs H hysteresis loops for some of the n=30 multilayers in (a) F/Al multilayer data. The figure is from [94]	63
2.14	(a) $A\Delta R$ against t_{Al} for $F/t(_{Al})/F$ (F=Py, Co, CoFe (= Cog ₁ Fe ₉), Fe) EBSVs. The corresponding datum for a Py/Cu EBSV (filled circle) is shown for comparison. Note the scale break for this datum. (b) AR vs H hysteresis loops for some of the t_{Al} =10 nm EBSVs as shown in (a). The figure is from [94]	65
2.15	The effects of aging and annealing on: (a) AR(Peak), and (b) $A\Delta R$ on remeasured F/Al (F=Py,Co,Cog ₁ Fe ₉ ,Fe) multilayers. The number of bilayer repeats for each multilayer is shown after each F/N. The number in the bracket below shows the time after which the sample was remeasured. The figure is from [94]	67
2.16	The effects of aging on: (a) AR(AP), and (b) $A\Delta R$ on remeasured F/Al/F (F=Py,Co,Cog ₁ Fe ₉ ,Fe) EBSVs. The number in the bracket below shows the time after which the sample was remeasured. The figure is from [94]	69
2.17	(a) AR(P) vs n data for the multilayer samples of the metal pairs under present study Co/Pt, Fe/Nb, Fe/V, and Py/Pd. Dashed lines show data for Py/Cu and Cog ₁ Fe ₉ /Al for comparison. The solid curves are based on the calculations from fits to the average values of AR(P) at $n=30$ and the EBSV data. (b) The corresponding hysteresis loops (AR vs. H) for $n=30$ multilayer samples. The figure is after ref [104]	75
2.18	(a) $A\Delta R$ vs t_N data for EBSV samples with the trilayer structure ${\rm Co/t}_{Pt}/{\rm Co}$, ${\rm Fe/t}_{Nb}/{\rm Fe}$, ${\rm Fe/t}_V/{\rm Fe}$ and ${\rm Py/t}_{Pd}/{\rm Py}$. For comparison, we show data for F/Cu (Fe/Cu data from [107], Py/Cu data from [57], and Co/Cu data from [52]). The $A\Delta R=0$ data for $t_{Pt}=5$ nm is hardly visible. (b) The corresponding hysteresis minor loops (AR vs. H) for some of the $t_N=10$ nm EBSV samples. The figure is from ref	
	[104].	76

2.19	(a) Plot of $A\Delta R$ against t_{Cu} for fixed $t_{Al}=10$ nm. For comparison, we also show $A\Delta R$ data for a $t_{Cu}=10$ nm EBSV. (b)Plot of $A\Delta R$ against t_{Al} for fixed $t_{Cu}=10$ nm	82
3.1	A cartoon to show the spin transfer torque in a F/N/F trilayer. The left F layer is a thicker layer than the right thin F layer. (a) The case when electrons propagate from the thicker F layer toward the thinner F layer (b) The case when electrons propagate from the thin F layer to the thick F layer. In (c) we show a typical differential resistance (dV/dI) vs. I plot of spin transfer torque induced switching. We show the higher resistance AP state, lower resistance P state, and the critical switching currents I_C^+ and I_C^- at which the magnetic configuration changes from P to AP and vice versa	87
3.2	A cartoon showing our nano-pillar fabrication process. (a) The sputtered multilayer. (b) The Al pillar $\sim 70 \times 130~\text{nm}^2,$ as a ion-mill mask, is evaporated onto the sputtered multilayer. (c) The sample is ion-milled approximately until the middle of the N layer. (d) SiO is evaporated 'in-situ' onto the ion-milled substrate. (e) The sample is ion-milled from sides. (f) The top Au pads are evaporated and the nano-pillar is ready to measure. In (f) we also show schematically the leads connected to measure the nano-pillar resistance	94
3.3	Optical microscope image of a $1/2$ " chip with leads. The right picture is a blow up of the central region.	95
3.4	The window for sputtering by e-beam lithography. This image is taken by an optical microscope.	96
3.5	The top figure is the optical image of nano-pillar holes after e-beam lithography. The bottom inset is an image of one of the Al nano-pillars taken by electron microscope.	97
3.6	Optical image of the substrate with the sputtered multilayer. The dashed lines schematically show the windows generated by e-beam lithography on a real multilayer for ion-mill calibration	98
3.7	The atomic force microscope scan of a ion-mill calibration sample	99
3.8	Optical image of the substrate after SiO liftoff. The dashed lines schematically show the window generated by e-beam lithography for ion-mill by sides	100
3.9	The optical image of the sample with top Au leads. The current and voltage leads to measure the resistance are marked as I^+ , I^- , V^+ and I^-	102

3.10	A cartoon of the finished nano-pillar. \hdots	102
3.11	An example of: (a) Magnetoresistance, and (b) Spin torque induced switching for a Cu sample measured at 295 K. The parabolic nature of the background dV/dI curve, and the asymmetry about $I=0$, are probably due to Joule heating and the Peltier effect [141]	106
3.12	An example of: (a) Magnetoresistance, and (b) Spin torque induced switching for a Cu sample measured at 4.2 K. The spin torque induced switching is noisy but still the sharp transition from P to AP and vice-versa could be identified	107
3.13	An example of: (a) Magnetoresistance, and (b) Spin torque induced switching for a CuGe sample measured at 295 K	107
3.14	An example of: (a) Magnetoresistance, and (b) Spin torque induced switching for a CuGe sample measured at 4.2 K.	108
3.15	An example of switching from P to AP in two steps. We exclude such data from our analysis.	109
4.1	A cartoon showing the effect of exchange bias at an F/AFM interface on hysteresis. The left figure shows a hysteresis curve for a F layer. The middle figure shows the hysteresis curve for a $F+AFM$ layer, but without any exchange bias. The right curve shows the hysteresis curve for $F+AFM$ layer with exchange bias. As mentioned in the text, the exchange bias is induced by heating the sample above the blocking temperature of the AFM and then cooling in a field	118
4.2	A cartoon showing AFM orientations for an antiferromagnetic GMR effect. The arrows represent the orientations of the individual moments. (a) The moment orientations adjacent to the middle N layer are parallel parallel configuration. (b) The moment orientations adjacent to the middle N layer are anti-parallel anti-parallel configuration	120
4.3	A cartoon of the point contact measurement setup. The inset shows a blowup of the point contact and the multilayer region. The figure is courtesy of Prof. M. Tsoi, University of Texas, Austin	122
4.4	Resistance vs. magnetic field for a series of applied currents for a $FeMn(8)/ CoFe(3)/ Cu(10) / CoFe(10)$ sample. All layer thicknesses are in nm. The solid black curves are down sweeps (positive to negative magnetic fields) and grey curves are up sweeps (negative to positive magnetic fields). The figure is from [17]	194

Grey scale plots of resistance vs magnetic field for different values of current. Here white represents the maximum R and black represents minimum R. The data shown is for an down sweep positive to negative magnetic field. The lines show linear fits to the data at 30% (dashed white), 50% (solid white) and 70% (dashed black) of full scale [100% = R(AP) - R(P)]. The three plots are for: (a) an FeMn(8)/CoFe(3)/Cu(10) / CoFe(10) sample (same as that of figure 4.4); (b) CoFe(10)/Cu(10) / CoFe(3)/FeMn(8) sample (inverted); and (c) FeMn(8)/CoFe(3)/Cu(10) / CoFe(3) sample. All layer thicknesses are in nm. The figure is from [17]	125
Grey scale plots of resistance vs magnetic field for different values of current for an $IrMn(8)/CoFe(3)/Cu(10)/CoFe(10)$ sample. All layer thicknesses are in nm. Here white represents the maximum R and black represents minimum R. The upper figure is for an up sweep negative to positive magnetic field, and the bottom figure is for a down sweep. The lines show linear fits to the data at 30% (dashed white), 50% (solid white) and 70% (dashed black) of full scale $[100\% = R(AP) - R(P)]$. The figure is from $[18]$	127
Grey scale plots of resistance vs magnetic field for different values of current for an FeMn(8)/ Py(10)/ Cu(10) / Py(3) sample. All layer thicknesses are in nm. Here white represents the maximum R and black represents minimum R. The upper figure is for an up sweep- negative to positive magnetic field, and the bottom figure is for a down sweep. The lines show linear fits to the data at 30% (dashed white), 50% (solid white) and 70% (dashed black) of full scale [100% = R(AP) - R(P)]. The figure is from [18]	129
Grey scale plots of resistance vs magnetic field for different values of current for $IrMn(8)/Py(10)/Cu(10)/Py(10)$ sample. All layer thicknesses are in nm. Here white represents the maximum R and black represents minimum R. The upper figure is for an up sweep-negative to positive magnetic field, and the bottom figure is for a down sweep. The white lines show linear fits to the data at 50% of full scale [100% = $R(AP) - R(P)$]. The figure is from [18].	130
	current. Here white represents the maximum R and black represents minimum R. The data shown is for an down sweep positive to negative magnetic field. The lines show linear fits to the data at 30% (dashed white), 50% (solid white) and 70% (dashed black) of full scale [100% = R(AP) - R(P)]. The three plots are for: (a) an FeMn(8)/CoFe(3)/Cu(10) / CoFe(10) sample (same as that of figure 4.4); (b) CoFe(10)/Cu(10) / CoFe(3)/FeMn(8) sample (inverted); and (c) FeMn(8)/CoFe(3)/Cu(10) / CoFe(3) sample. All layer thicknesses are in nm. The figure is from [17]

4.9	A schematic model showing the effect of the current on exchange bias. The grey color represents F metal and the black color represents an AFM metal. The vertical arrows at the F/AFM interface are fixed moments that give the exchange-bias. The tilted light grey arrows at the F/AFM interface are free moments, exchange coupled to the black AFM domain indicated by the dotted box. As current rotates this domain, the free grey moments rotate with it. Electrons going from F to AFM rotate the AFM domain toward the vertical, increasing the exchange-bias. Electrons going from AFM to F rotate the AFM domain away from vertical, decreasing the exchange-bias. The figure is taken from [17]	130
4.10	Point-contact magnetoresistance at different bias currents for a 1.3 Ohm point contact to sample $CoFe(10)/FeMn(8)/Cu(10)/FeMn(8)/CoFe(3)$. All layer thicknesses are in nm. The solid traces show point-contact resistance versus applied magnetic field for a series of applied currents. The figure is from [19].	134
4.11	The maximum change in resistance, ΔR , vs. point contact resistance at I = 30 mA for down-sweeps. The open symbols show data for four different F1/AFM1/N/AFM2/F2 samples with $t(F_1)=10$ nm, $t(F_2)=3$ nm and $t(AFM1, AFM2)=(3,3), (3,8), (8,3)$ and $(8,8)$. All layer thicknesses in nm. F1 = F2 = CoFe and AFM = FeMn. The error bars are smaller than the symbol sizes. We also show, for comparison, data for F1/AFM1/N/AFM2/F2 samples with $t(F_1)=t(F_2)=3$ nm (solid symbols). Note that the MRs for F1/F2 = 3/3 are much less than that for F1/F2 = 10/3. The figure is after [19]	135
4.12	The maximum change in resistance, ΔR , vs. point contact resistance at I = 30 mA for down-sweeps. The open symbols show same data as shown in figure 4.11. The filled symbols show data for samples with F (= CoFe) = 10nm sandwiched between different metals, as shown in the legend. The error bars are smaller than the sizes of the symbols. The figure is from [19].	137
A.1	A schematic drawing of a film used to do Van der Pauw resistivity measurement. The shaded central region is the sputtered film. The small irregular regions on the edges represent the Indium contacts	147
A.2	AR versus \mathbf{t}_{Fe} plot for Nb(150nm)/ Fe(\mathbf{t}_{Fe})/Nb(150 nm) multilayers. The slope of the best-fit straight line gives $\rho_{Fe}=95\pm6$ n Ω m and the intercept gives $2\mathrm{AR}_{Nb/Fe}=7.6\pm0.8$ f Ωm^2 . The value of the intercept agrees with the prior estimates of Bozec et al [54] and Zambano et al [53]. The figure is from [104]	150

Chapter 1

Introduction

1.1 Spintronics

Spintronics [1], an acronym for spin transport electronics, also known as magnetoelectronics, is a rather new subject of research based on 'spin angular momentum'
or 'spin' of the electron. Such electronics is to be contrasted with conventional electronics, which is based solely on the charge of the electron. The ground-work for the
subject was set by earlier studies of spin dependent scattering in metallic ferromagnetic (F) alloys [2], study of spin-relaxation in the non-magnetic metal Al [3], and
studies of polarization in ferromagnetic metals [4]. Ferromagnets are magnetically
ordered materials with net magnetic moment even in the absence of a magnetic field.
Modern spintronics started with the discovery of giant magnetoresistance (GMR) in
metallic ferromagnetic/ non-magnetic (F/N) multilayers independently by Fert [5]
and Grünberg [6] in 1988. For this discovery, they were awarded the 2007 Nobel prize
in physics [7]. Almost a decade later (1996), the subject was augmented by the prediction of a complementary phenomenon of spin transfer torque (STT) by Slonczewski
[8] and Berger [9]; subsequently followed by experimental observations [10, 11, 12].
Both GMR and STT have been extensively studied in metallic multilayers composed

of ferromagnetic and non-magnetic metals. Effects similar to ferromagnetic GMR and STT were recently predicted with antiferromagnets (AFM) [13, 14, 15, 16] -- magnetically ordered materials with net magnetic moment zero in the absence of a magnetic field. Our first subsequent experiments [17], and then ones by us [18, 19] and others [20, 21, 22], have shown current mediated effects on exchange bias involving F/AFM interfaces; but the predicted effects on bulk antiferromagnets are yet to be observed. Apart from metallic systems, spin dependent transport has been studied in systems containing insulators and semiconductors. We do not discuss these two systems.

This thesis describes projects intended to generate new information about each of the three topics noted above: (a) GMR, and (b) STT, both with metallic ferromagnets, and (c) spintronics effects with metallic antiferromagnets. Chapter 1 provides background about the topics to be covered and ends with an overview of the specific projects included. Chapters 2-4 then contain details of the projects.

1.2 Background

Historically, studies of the effect of magnetism on electrical resistance date back to the 1850s. Lord Kelvin, a British physicist, showed in 1856 [23] that the resistance of a ferromagnetic conductor increases as a magnetic field is applied along the current flow and decreases when applied across the current flow - - an effect now known as anisotropic magnetoresistance (AMR). Non-magnetic metals also exhibit magnetoresistance (MR), due to the Lorentz force that arises from the applied magnetic field [24]. Traditionally, MR is defined as the percentage change in resistance upon application of a magnetic field.

1.2.1 Spin Dependent Transport

The underlying principle of spintronics is spin dependent transport - - transport depending on the spin of the electron, apart from its charge. The electron has spin quantum number s = 1/2, which corresponds to two projection states $s_z = \pm 1/2$. We denote these two spin states as *spin up* and *spin down*. The spin angular momentum has an associated magnetic moment m_z given as

$$\langle \mathbf{m}_{\mathbf{Z}} \rangle = -\frac{e}{2m_e} g \langle \mathbf{s}_{\mathbf{Z}} \rangle$$
 (1.1)

where -e is the charge of the electron, m_e is the mass of the electron, g is the electron g factor (≈ 2) and $< s_z >$ and $< m_z >$ are the expectation values of s_z and m_z respectively. The minus sign in equation 1.1 implies that, with reference to a quantization axis, the magnetic moments are oriented opposite to the spin states. We refer to the two magnetic moment states of the electron as up moment and down moment. In the present notation, spin up and down moment, and spin down and up moment, each refer to the same state of the electron. Unless specifically mentioned otherwise, we will discuss spin dependent transport in terms of electron moments.

If an electron is passing through a ferromagnet (F), its moment can be along or opposite to the moment of the F. For simplicity, we will denote the state with electron moments along the F moment by \uparrow , and the state with electron moments opposite to the F moment by \downarrow . Figure 1.1 shows a schematic drawing of the sign convention. The electron moments themselves are represented by thick grey arrows with an 'e' in the center, and the ferromagnet moments are represented by empty arrows.

The first predictions of spin dependent transport were given by Mott in 1936

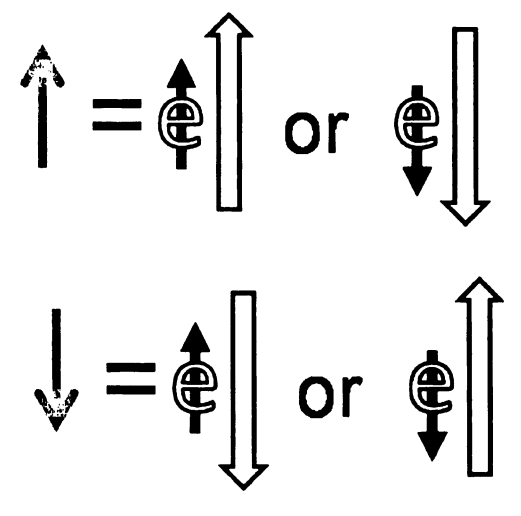


Figure 1.1: The sign convention we will follow - - \uparrow = Moment of the electron is along the moment of the ferromagnet. \downarrow = Moment of the electron is opposite to the moment of the ferromagnet.

[25]. He proposed that the electrical resistance of a ferromagnetic transition metal is mainly due to scattering in which current-carrying s electrons jump to d bands where electron motion is more sluggish. He proposed that, absent any spin flipping, such scattering is **spin selective** - - electrons jump only to d states with the same spin, and the scattering out of s states becomes stronger as more d states are available. The two spin states carry electrical currents in parallel.

For ferromagnets in the s-d model, the d band density of states near the Fermi level for the $down\ moment$ channel is generally larger than the density of states for the $up\ moment$ channel [24, 26]. Due to the unequal density of states, the resistivity of \downarrow state electrons is greater than resistivity for \uparrow state electrons - - $\rho_{\downarrow}^{F} > \rho_{\uparrow}^{F}$, since the main current carrying s electrons can be scattered more often into sluggish d states. In non-magnetic metals, the d band density of states near the Fermi energy (E_F) is equal for both the channels [24, 26] and the resistivities for \downarrow and \uparrow states

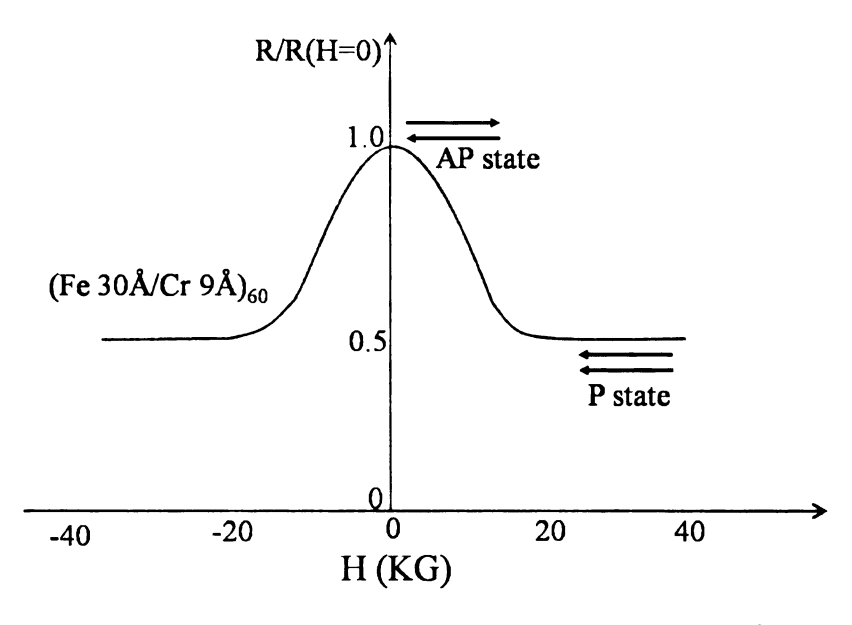


Figure 1.2: A schematic drawing of R versus H curve for $(Fe(30 \text{ Å})/Cr(9\text{Å}))_{60}$ multilayers, measured at 4.2 K. The figure is after [5].

are equal - -
$$\rho_{\uparrow}^N = \rho_{\downarrow}^N$$
.

1.2.2 Giant Magnetoresistance (GMR)

Giant Magnetoresistance (GMR) was discovered independently by Grunberg [6] and Fert [5] in 1988, using epitaxially grown Fe/Cr multilayers. In epitaxial growth, the atomic layers grow in registry with each other. The multilayers had very thin Cr layers (~ 1 nm), which had previously been shown to couple alternate Fe layers antiferromagnetically [27, 28]. We discuss more on magnetic ordering in section 1.2.3. The resistance of the as-grown antiferromagnetically coupled samples dropped as the moments of the Fe layers were aligned parallel by applying a large magnetic field. The drop in the resistance measured at 293 K was a few % in trilayer samples at saturation fields ~ 300 Oe [6]. The drop in resistance measured at 4.2 K was up to

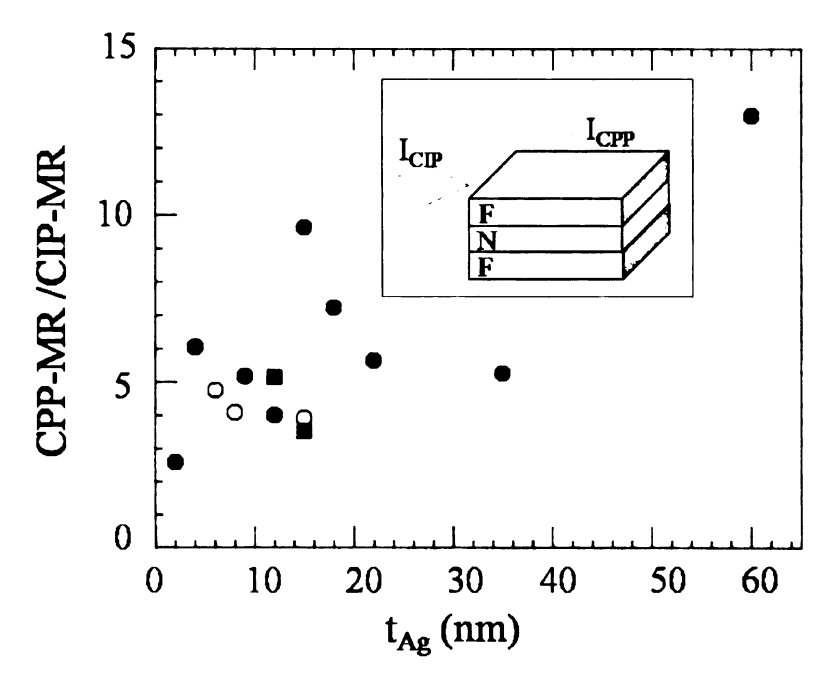


Figure 1.3: CPP-MR/CIP-MR ratio for Co/Ag multilayers showing CPP-MR is much greater than CIP-MR (after figure 3, ref [30]). The inset shows the CPP and CIP current directions in a metallic multilayer.

50% - - hence termed 'Giant'- - in multilayer samples at saturation fields ~ 2 T [5]. Figure 1.2 shows the GMR data for Fe/Cr multilayers measured at 4.2 K. The large value of GMR, as compared to the MR of single magnetic films, was soon utilized by industry in read heads enabling higher capacity hard disks [29].

1.2.2.1 Current geometries and effect on MR

The current in a thin film sample can be made to flow in-plane (CIP) or perpendicular to the plane (CPP) of the sample (see inset in figure 1.3). For a short and wide sample, with length (l) = width (w) = 1 mm (area = 1 mm²), thickness (t) $\sim 0.1 \,\mu\text{m}$ and ρ = 100 n Ω m, we get, R_{CIP} (= ρ l/wt) $\sim 1\Omega$ and R_{CPP} (= ρ t/wl) ~ 10 n Ω . The CIP resistance is easy to measure, and thus the initial studies of GMR had the electric

current flowing in the plane of the layers (CIP). The ultra low sample resistances for the CPP geometry require a special measurement technique [30], which we describe in chapter 2. Consistent with the predictions of Zhang and Levy [31], Pratt et al [30], first showed that currents flowing perpendicular to the plane (CPP) could yield a much larger MR than CIP-MR [31] as shown in figure 1.3.

In addition to often giving a larger MR, the CPP geometry also has other advantages. The CPP-MR is usually less sensitive to sample inhomogeneities than the CIP-MR [32]. A comparison of interface parameters for multilayers prepared by different techniques suggests that the CPP-MR is also not as sensitive to changes in interfacial properties as the CIP-MR [32]. In the absence of any spin flipping, the CPP-MR can be analyzed by a simple two current series resistor model (2CSR) [31, 33, 34, 32]. Reviews of CIP and CPP magneto-transport with more detailed information on theory and experiment are given in refs. [35, 36, 37, 32, 38].

The CPP geometry is thus often more suited to test GMR models and to determine the physics underlying spin dependent transport. Nano-pillar sized samples allow CPP resistance to become large enough for devices. For such samples, the CPP geometry has been shown to offer advantages in terms of read head performance and is being projected as a future technology for read heads with recording densities > 300 Gb/in² [39].

1.2.2.2 Simple 2 current model of GMR

Figure 1.4, shows a schematic of the Fert model of GMR. Electrons with moments up and down traverse independently through the layers. Following the notation in

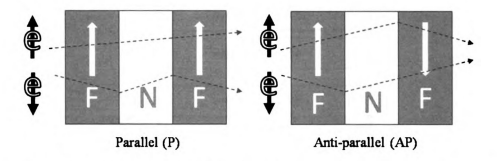


Figure 1.4: Two F layers in the parallel and antiparallel orientations. The dashed lines show how electrons with moments along or opposite to the local magnetization are scattered as they traverse the layers.

section 1.2.1, we assume that \(\) electrons (electrons with moment opposite to the local F moment) scatter more strongly than \(\) electrons (electrons with moment along the local F moment). Figure 1.4 (left) shows that when the moments of both F's are parallel, parallel (P) state, the up moment electrons scatter weakly in both F layers, and thus short the sample, yielding a low resistance. Figure 1.4 (right) shows that when the moments of both F's are anti-parallel, anti-parallel (AP) state, both the up and down moment electrons scatter strongly in one of the F layers, thus giving a higher resistance than the P state. The resulting difference in resistance between P and AP states is the source of GMR.

1.2.3 Control of magnetic order

Control of GMR requires control of the magnetic order of the F layers. The magnetic order of the F layers can be controlled by the following methods.

Antiferromagnetically coupled F/N multilayers: In 1986, Grünberg
et al showed experimentally the existence of antiferromagnetic coupling (antiparallel (AP) state) in Fe layers separated by thin Cr layers (~ 1nm) [27, 28].

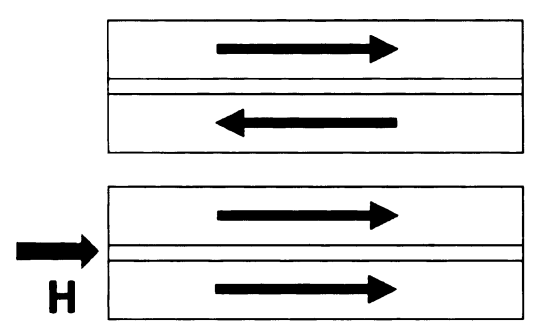


Figure 1.5: The layers with arrows denote ferromagnets with moments pointing in the direction of the arrows. The thin layer in between is the N layer. The top figure represents an anti-parallel configuration and the bottom figure shows the parallel configuration after a high magnetic field is applied.

A large magnetic field was needed to align all the Fe moments parallel to each other, leading to a parallel (P) state. Figure 1.5 shows an example of the antiparallel (AP) and parallel (P) states.

2. Uncoupled $[F/N]_n$ multilayers: We consider next $[F/N]_n$ multilayers with identical F layers and identical N layers. Parkin et al showed experimentally that the coupling between F layers separated by a N layer oscillates between antiferromagnetic and ferromagnetic as the N layer is made thicker [40, 41]. The F layers finally became uncoupled for thick $N \gtrsim 5$ nm.

In CPP-MR, the parameter of interest is the specific resistance - - area (A) through which the current flows times resistance (R). Figure 1.6 shows an example of the AR versus H curve for such an uncoupled multilayer. The AR curve shows three different states. The low resistance state at large saturation fields corresponds to the parallel (P) state, and is well defined. The as-grown state gives the maximum resistance(AR°). Sweeping the field back from saturation gives an intermediate maximum of resistance (AR(peak)). This state of

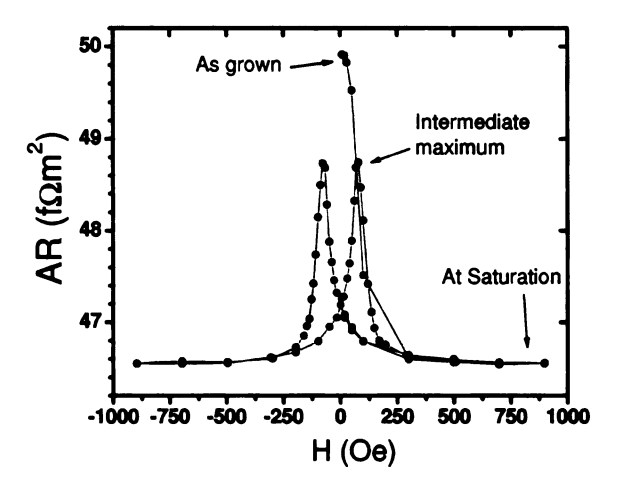


Figure 1.6: AR vs. H plot for a typical F/N multilayer sample. The low resistance at saturating fields corresponds to the parallel (P) state. The maximum resistance is for the as-grown state, which has been argued to most closely approximate the anti-parallel (AP) state. Sweeping fields back from saturation gives intermediate maximum of resistance.

intermediate maximum has been shown to correspond to a net moment (M) = 0 [30, 42]. Since the AP state should give maximum resistance, the as-grown state looks to be the best approximation to the AP state. But formally, it is only a lower bound to the true AP resistance. For Co/Ag and Co/Cu, the as-grown state has been shown to be a good approximation to the AP state [30, 42]. However, for Py/Cu ($Py = Ni_{84}Fe_{16}$), the as-grown state is not close to the AP state [43].

3. Spin valves: To achieve a clear anti-parallel state in F/N/F trilayers, one uses a spin valve, in which the switching fields of the two F layers are made different. The N layer is kept sufficiently thick to eliminate any exchange coupling between the two F layers. Initially a large field is applied to orient the moments of the

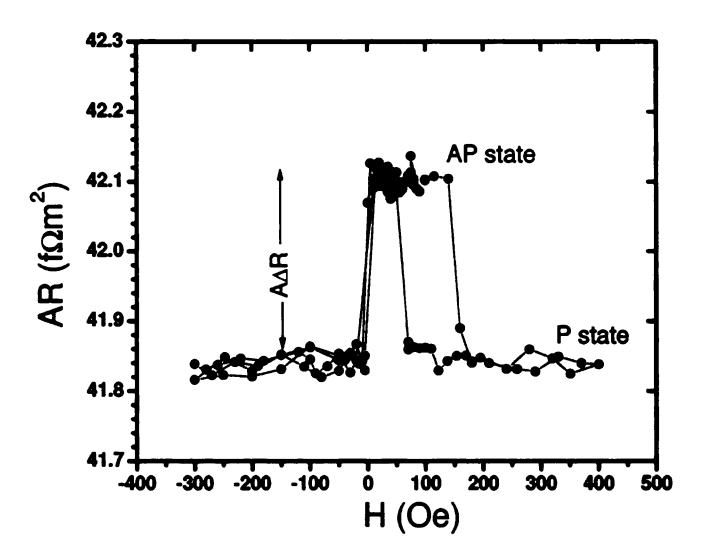


Figure 1.7: AR vs. H plot for a typical EBSV sample, showing clear parallel and anti-parallel states. $A\Delta R$ is also shown.

F layers in the same direction (parallel configuration). Sweeping the field in the opposite direction, the F layer with the lower switching field switches first to give an anti-parallel configuration. Sweeping the field further, the second F layer then switches at a larger field giving the parallel configuration. Usually, only the F layer with the smaller switching field is toggled to achieve P and AP states. The difference between the switching field of the two F layers can be achieved by:

- (a) using two F metals with very different coercive fields - either different F metals or the same F metals but with very different thicknesses. These samples are called hybrid spin valves.
- (b) pinning one of the F layers by exchange bias, as proposed by Dieny et al [44]. The pinning is achieved by growing an anti-ferromagnetic (AFM)

layer next to the F layer and then heating the sample above the blocking temperature of the AFM and cooling in a field. The pinned F layer is then hard to switch, whereas the unpinned F layer can be switched easily. These samples are called exchange biased spin valves (EBSV). Figure 1.7 shows a typical CPP measurement for an EBSV. Note clear P and AP states. $A\Delta R = AR(AP) - AR(P)$ is also shown for reference.

1.3 Current perpendicular to the plane magnetoresistance: Parameters and their prior values

Since CPP-MR is the basis for the first part of this thesis, we define the parameters to be used.

In the analysis used in this thesis, the fundamental length in CPP-MR is taken to be the spin diffusion length (l_{sf}) - - the mean distance that electrons diffuse between spin-flipping collisions [33] (see figure 1.8). l_{sf} is related to the spin flip length, λ_{sf} , and the mean free path, λ_{t} , via the relations:

$$l_{sf}^{F} = \sqrt{\frac{\lambda^{F*}\lambda_{sf}^{F}}{6}} = \sqrt{\frac{(1-\beta^{2})\lambda_{t}^{F}\lambda_{sf}^{F}}{6}}$$
 (1.2)

$$l_{sf}^{N} = \sqrt{\frac{\lambda_{t}^{N} \lambda_{sf}^{F}}{6}} \tag{1.3}$$

For most of the metals and alloys used in this thesis, the values of l_{sf} have already been measured. We list the values of l_{sf} from those studies in Table 1.1. β will be defined just below.

The physics of CPP-MR involves asymmetric scattering in both the F layers and at the F/N interfaces, often dominated by the latter as the layers become very thin.

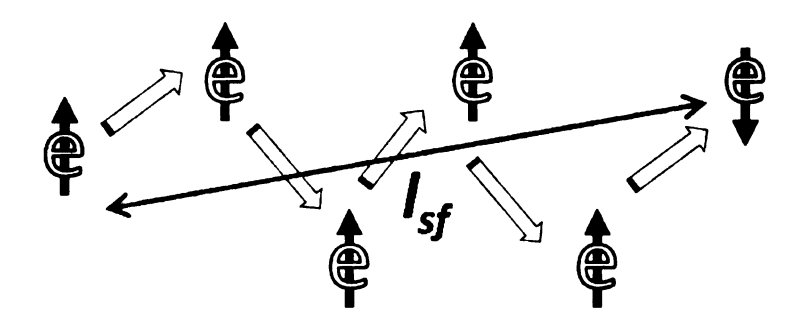


Figure 1.8: A cartoon showing a 'qualitative' model of spin diffusion length(l_{sf}) - - the mean distance electrons diffuse between spin-flipping collisions. The exact representation of l_{sf} is as given in equations 1.2 and 1.3. The hollow arrows represent 'mean free paths' - - the mean distance electrons travel between scattering events. The sum of all the hollow arrows represents the mean distance an electron travels before flipping its spin - - spin flip length (λ_{sf}) .

Knowledge of both the bulk and interface CPP-MR parameters is thus essential for understanding the underlying physics and for analysis. In the bulk, the asymmetric scattering is represented by ρ_F^{\downarrow} and ρ_F^{\uparrow} . At the interfaces it is represented by spin dependent interface specific resistances - - $AR_{F/N}^{\uparrow}$ and $AR_{F/N}^{\downarrow}$. However, the equations to analyze CPP-MR data are greatly simplified by using alternative bulk and interface parameters [34, 33]:

$$\rho_F^* = \frac{\rho_F^{\downarrow} + \rho_F^{\uparrow}}{4} = \frac{\rho_F}{1 - \beta^2} \tag{1.4}$$

where

$$\beta = \frac{\rho_F^{\downarrow} - \rho_F^{\uparrow}}{\rho_F^{\downarrow} + \rho_F^{\uparrow}} \tag{1.5}$$

and

$$AR_{F/N}^{*} = \frac{AR_{F/N}^{\downarrow} + AR_{F/N}^{\uparrow}}{4} = \frac{AR_{F/N}}{1 - \gamma^{2}}$$

$$\tag{1.6}$$

	$ ho_{old}$	β	l_{sf}
Element	$\mathbf{n}\Omega\mathbf{m}$		nm
Cu	$5\pm 1 \ [45]$		~ 1000 [45]
Al	5±1 [45]		$\geq 500 \ [45]$
Ag	7±2 [45]		$\geq 500 \ [45]$
Nb	$78 \pm 15 [46, 45]$		$48 \pm 3 [46, 47, 45]$
V	$105 \pm 20 [46, 45]$		$46 \pm 5 [46, 45]$
Pd	$40 \pm 3 [48, 45]$		25^{10}_{-5} [48, 45]
Pt	26±1 [48]		23± 10 [48]
$Py (= Ni_{84}Fe_{16})$	120±40 [49, 50]	0.76 [32, 50]	5.5 ± 1 [45, 50]
Co	60±9 [49]	0.46 [32]	$\sim 60 \ [45, 51]$
$\text{Co}_{91}\text{Fe}_{9}$	$70 \pm 10 \ [45, 52]$	0.65 [52]	$12\pm 1 \ [45, 52]$
Fe	40±10 [53]	0.78 [54]	8.5 ± 1.5 [54]

Table 1.1: Reference values from old estimates of resistivity (ρ_{old}) , spin diffusion length (l_{sf}) , and bulk asymmetry parameter (β) , for metals used in the present study. Except for the resistivities of Nb and V, all the other values were determined at 4.2 K. Since Nb and V are superconductors at 4.2 K, their resistivities were measured at 12 K.

where

$$\gamma = \frac{(AR_{F/N}^{\downarrow} - AR_{F/N}^{\uparrow})}{(AR_{F/N}^{\downarrow} + AR_{F/N}^{\uparrow})}$$
(1.7)

.

We will analyze our data in terms of these alternative bulk and interface parameters.

For the bulk parameters, ρ_F is the separately measured resistivity of the F metal, and β is the bulk asymmetry parameter. In our case, we measure ρ on thin films using the Van der Pauw technique [55] as discussed in appendix A.1.

Most of the metals used in this thesis are nominally 'pure' metals, for which the resistivity at our measuring temperature of 4.2 K, is due to an unknown combination of unknown impurities with stacking faults and grain boundaries. In principle, the resistivities of such metals might vary from run to run, or with the method of sample

fabrication, or upon changing the sputtering targets. For F metals, β might also vary from run to run. We thus need to determine the resistivities of each metal for each batch of samples, to see that the values are stable over time and stable for different targets of the same metal.

For dilute F-alloys, in contrast, with a known impurity that dominates the scattering, β should be uniquely determined. β for a number of commonly used dilute F-alloys was first determined by studies based on deviations from Matthiessen's rule (DMR) [2], and more recently determined from studies of CPP-MR [50, 52, 56, 57, 32]. In most cases the estimates of β by both methods were found to be consistent [58] within mutual uncertainties.

For the F metals used in this thesis, estimates of β exist from earlier studies in our laboratory [50, 52, 56, 57]. Table 1.1 lists these earlier values of resistivities and β for the metals used in this thesis. To use those estimates, we must show that the resistivities of our newly sputtered samples agree with the previously measured resistivities of the given F metals. For each of the studies in this thesis, we have thus independently measured the resistivity of each sputtered metal. With only two exceptions, Fe and Ag, our resistivities are consistent, within mutual uncertainties, with the prior values. For Fe, probably due to a new sputtering target, our measured resistivity was much larger than prior measurements. We have thus separately determined β for this target. Except for Fe, we will use the values of β from the earlier studies [50, 52, 56, 57, 32]. For Ag, even though we get a higher resistivity, it does not affect our studies because the resistivity is still small.

The interface parameters, $2AR^*$ and γ , are the focus of this thesis. To give

Metal pair	2AR (exp)	2AR (Perfect)	2AR (2 monolayer disorder)
	f Ωm^2	${ m f}\Omega m^2$	${ m f}\Omega m^2$
Ag/Au	0.1	0.09	0.12
Fe/Cr	1.6	1.5, 1.9	1.6
Pd/Pt	0.28	0.30	0.33
Au/Cu	0.3	0.45	0.7
Ag/Cu	0.1	0.45	0.6
Pd/Cu	0.9	1.5	1.6
Pd/Ag	0.7	1.6	2.0
Pd/Au	0.5	1.7	1.9
Co/Cu	1.0	0.9	1.1

Table 1.2: 2AR(exp) versus rounded no-adjustable-parameter calculations for close packed interfacial layers. 2AR (Perfect) represents a perfect interface and 2AR(2 monolayer disorder) represents an interface with two monolayers randomly mixed 50-50. For Co/Cu and Fe/Cr, the experimental values represent 2AR*. The values listed above (below) the double line are for lattice matched metal pairs with $\Delta a/a < (>)1\%$. Except for Pd/Pt, the values are taken from ref [59]. The values of Pd/Pt are taken from ref [48].

Metal pair	Orientation	2AR (Perfect)	2AR (2 monolayer disorder)
		${ m f}\Omega m^2$	${ m f}\Omega m^2$
Al/Ag	(111)	0.64	0.92
$\mathbf{a}_{fcc} = 4.05 \text{ Å}$	(110)	1.60	1.39
, ,	(001)	2.82	2.37

Table 1.3: Calculated specific interface resistance of Al/Ag. The third column lists the values for perfect interfaces and the fourth column lists the values with interface disorder modeled as two layers of a 50-50 alloy in 10×10 lateral supercells. The table is after Ref. [60].

the reader a feeling for magnitudes, Table 1.2 lists previously determined values of $2AR_{F/N}^*$ for two standard metal pairs, Co/Cu and Fe/Cr. Table 1.2 also lists earlier values of specific interface resistance $2AR_{N1/N2}$ of several N1/N2 metal pairs

The initial CPP-MR models [31, 61, 62, 33] treated 2AR* and γ as fitting parameters for experimental data. More recently it has become possible to calculate 2AR* and γ without any adjustable parameters [63, 64, 65, 66]. The models work well for lattice matched pairs - $\Delta a/a < 1\%$, where a is the lattice constant. For $\Delta a/a > 1\%$

1%, unknown lattice restructuring at the interface complicates the calculations, and the models do not work so well. Table 1.2 lists calculations of 2AR (and 2AR*) for perfect interfaces and for interfaces with 2 monolayers of disorder. The experimental values are also listed for comparison. The calculations agree with experiment for metal pairs with $\Delta a/a < 1\%$ but not for metal pairs with $\Delta a/a > 1\%$. Recently, Xu et at [60] calculated the effect of 'orientation' and 'interface disorder' on the interface parameters of commonly used metal pairs. They found that, for most of the metal pairs chosen, the interface parameters were not sensitive to orientation or alloying. But for Al/Ag, the interface resistance was found to be strongly dependent on the orientation as well as on interfacial alloying. Table 1.3 lists the results of the calculations of Xu et al [60] for Al/Ag. Note that both the (110) and (001) calculations give a smaller 2AR for the disordered interface.

To use CPP-MR in devices, one wants both relatively large R and large MR. As the devices are made smaller, the layers get thinner and the interfaces dominate. The interface parameters, $2AR^*$ and γ , are thus more crucial for such potential devices. A large value of $2AR^*$ corresponds to a large R, and a large value of the product $2AR^*\gamma$ corresponds to large MR. Thus to use CPP-MR in devices, one requires large values of both $2AR^*$ and γ . The product $2AR^*\gamma$ gives a rough measure of when both interface parameters are large.

1.4 Spin transfer torque (STT)

As described above, in GMR the magnetic configuration influences the transport properties. Spin transfer torque (STT) is the complimentary phenomenon, where the transport currents influence the magnetic configuration. STT has been an area of active theoretical and experimental research since its prediction by Slonczewski [8] and Berger [9] in 1996, and its first observation in 1998 [10]. The basic concept of spin transfer torque is that an unpolarized dc current, upon passing through a ferromagnet with moment fixed in direction (fixed layer), becomes 'partially' polarized along the direction of moment of the ferromagnet. This spin polarized current then exerts a torque on a second ferromagnet (free layer), so long as its magnetic moment is not collinear with the direction of polarization of the current. This torque competes with damping, so that sufficiently large current density ($\sim 10^8 \, \text{A/cm}^2$) causes 'precession' (see figure 1.9) or 'switching' of the free layer moment, depending upon the intensity of the applied magnetic field . Switching of the free layer leads to parallel or antiparallel configurations of the two ferromagnets, which then shows up as a change in resistance of the sample due to the GMR effect. The precession of the free layer causes generation of high frequency (microwave) excitations, which are detected through the GMR effect.

To observe spin transfer effects requires ultra small cross section (~ few 100 nm in diameter) samples for: (a) achieving high current densities, and (b) the spin transfer effects to dominate over self Oersted field effects due to the propagating current. These small cross-sections have been usually obtained with point contacts - - mechanical or lithographic, or lithographically patterned nanopillars. As noted above, the first experimental evidence of spin transfer torque driven excitations was obtained by Tsoi et al in 1998 [10, 67], as current and field dependent steps in the resistance of Co/Cu multilayer samples measured at 4.2 K using Ag mechanical point contacts.

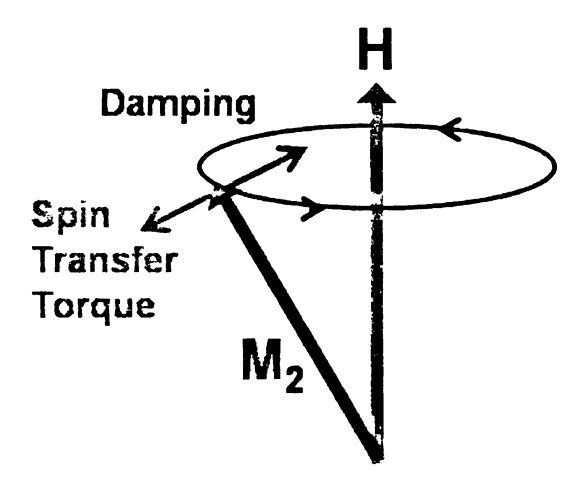


Figure 1.9: A cartoon showing the spin transfer torque and damping for a ferromagnet (free layer) with moment M_2 . The direction of the spin transfer torque depends on the direction of the current. H sets the direction of the moment of the polarizing 'fixed' ferromagnet.

The first observation of spin-current induced switching of the magnetic state was by Sun [68] in 1999 in granular manganite trilayer junctions. Shortly thereafter, spin transfer torque driven switching was observed in lithographic point contacts by Myers et al [11] in 1999 and in lithographically patterned nano-pillars by Katine et al [12] in 2000.

The first direct evidence of spin torque induced magnetic precession was observed by Tsoi et al [69] in 2000. They observed additional dc responses due to non-linear mixing, at or near resonance, by applying microwave radiation to Ag mechanical point contacts to metallic multilayers. The spin torque induced steady state magnetic precession was soon directly measured as voltage oscillations. [70, 71, 72]

The above mentioned studies were done on sample structures with a polarizing F layer and a free F layer. It was soon predicted [73, 74, 75, 76, 77], and experimentally observed [78, 79], that spin transfer effects could be seen with only one ferromagnet.

These effects are weak, require high fields, and are less controlled, making them unsuitable for device applications. We will not cover spin transfer effects with only one ferromagnetic layer in this thesis.

The possibility of switching the magnetic state of a ferromagnet, and generation of microwave signals by dc current, makes these effects potential candidates for devices. Spin transfer induced switching has been projected to be a technology for new magnetic random access memories (MRAM) [80].

1.5 Antiferromagnetic Spintronics

The spintronics effects - - GMR and STT, described above, were predicted and observed in ferromagnetic systems. It was thus intriguing when MacDonald and coworkers predicted the possibility of corresponding effects in multilayers where the ferromagnets are replaced by antiferromagnets (AFM) [13, 14, 15, 16]. They predicted that, like in ferromagnetic GMR, the resistance of an AFM/N/AFM trilayer could depend upon the relative orientations of the magnetic moments in the two AFM layers. They called such a phenomenon antiferromagnetic GMR (AGMR). They also predicted that a large enough current density injected in an AFM could affect its magnetic state due to spin transfer torque. They estimated smaller critical currents needed to alter the magnetic order in AFMs than in Fs, due to the absence of shape anisotropy and as spin torques act on the entire volume of an AFM. These new AFM predictions are very exciting and could potentially lead to a new field of all-AFM spintronics where AFMs are used in place of Fs.

The predictions, however, are based on calculations assuming perfect samples. The

calculations thus depend upon quantum coherence, and any disorder should reduce the predicted effects. Experiments are thus crucial to see if any such effects can be observed in real 'imperfect' samples.

1.6 This Thesis

In this thesis I have done studies intended to generate new information about GMR and STT with ferromagnets, and to search for spintronics effects with antiferromagnets. Much of the experimental work has been done in collaboration and I will highlight the contributions in the individual projects.

This thesis is organized as follows.

1.6.1 CPP-MR studies

In Chapter 2, I present new experiments to study CPP-MR interface parameters. The genesis of these studies was a discovery by the Cornell group of unexpected transport in Py/Al/Py nanopillars. They found [81] that such nano-pillars had: (a) larger resistance, (b) smaller MR, but (c) similar switching currents to Py/Cu/Py nanopillars. They concluded that the spin-dependent scattering properties of Py/Al interfaces must be significantly different from those of Py/Cu. However, it was hard to quantify $2AR_{Py/Al}^*$ and $\gamma_{Py/Al}$, since their lead resistance was not fully controlled.

Their results stimulated us to use our well-controlled CPP-MR technique to obtain quantitative values of Py/Al interface parameters. The resulting Py/Al experiments gave unusually large $2AR_{Py/Al}^* \sim 8.5~\mathrm{f}\Omega m^2$, but small $\gamma \sim 0.025$. This large value of $2AR_{Py/Al}^*$ stimulated us to extend our studies with Al to other F metals (F: Co, Fe

& Cog₁Fe₉) in the hopes of finding large values of both $2AR_{F/Al}^*$ and γ that would be more competitive for devices. As we will describe, these experiments again gave large values of $2AR_{F/Al}^* \sim 8$ -11 f Ωm^2 , but still small $\gamma \leq 0.18$.

To try another path to large $2AR^*$ and large γ , we extended our studies to other N metals - - Pd, V, Nb and Pt, chosen to have at least modestly large l_{sf} . For each N metal, we chose an F metal with the same crystal structure. We settled upon F/N = Py/Pd, Fe/V, Fe/Nb and Co/Pt metal pairs. The results will be presented in section 2.4.2.

In extending their Py/Al/Py nanopillar studies [81], the Cornell group found that bracketing thick Al (\sim 10nm) with thin Cu (\sim 0.6 nm) in Py/Cu/Al/Cu/Py multilayers gave an MR closer to the smaller one for Al than to the larger one for Cu [82]. Our initial interpretation of this observation was that such thin Cu would be incorporated into the finite thickness F/Al interfaces, and thus play a minor role. If so, then making the Cu thick might give an MR similar to that for Cu. To check this interpretation, the CPP-MR experiments were extended to study the effect of Cu(t_{Cu})/ Al(t_{Al})/ Cu(t_{Cu}) sandwiches on the A Δ R of Py exchange biased spin valves (EBSV). The results will be presented in section 2.4.3.

To properly interpret the Py/Cu /Al/ Cu/Py study, we needed to determine $2AR_{Al/Cu}$. The results are described in section 2.3.2. In 2006, Xu et al [60] predicted that $2AR_{Al/Ag}$ varies strongly with: (a) orientation, and (b) disorder. This led us to determine $2AR_{Al/Ag}$ (111). In this project, we recognized that disorder, caused by interdiffusion was likely to complicate analysis. The results will be presented in section 2.3.1.

I will indicate the collaborators at the start of the discussion of each project.

Organization of Chapter 2

Chapter 2 starts with an overview of the theory of CPP-MR. It then explains our experimental procedures, including sample fabrication and measurement techniques, and the different types of samples used in the experiments. The experiments to be described are covered in the following order.

- Experiments involving Non-magnetic metal (N1) / Non-magnetic metal (N2) interfaces:
 - 1. Estimate the specific resistance of an Al/Ag interface.
 - 2. Estimate the specific resistance of an Al/Cu interface.
- Experiments involving Ferromagnetic (F) / Non-magnetic metal (N) interfaces :
 - 1. Determine 2AR* and γ of F/Al (F:Py, Co, Fe & Coq1Feq) interfaces.
 - 2. Determine 2AR* and γ of F/N - Py/Pd, Fe/V, Fe/Nb and Co/Pt interfaces.
 - 3. Effect of Cu/Al/Cu sandwiches on the A Δ R of Py exchange biased spin valves.

1.6.2 Spin transfer torque studies

In chapter 3, to help understand the underlying physics of spin transfer torque, I will describe experiments to study the effects of changing only the transport in the non-magnetic metal spacer. I first give an overview of spin transfer torque and the various

models used to explain the phenomenon. Then I briefly discuss the sample details, sample fabrication, and measurement techniques. This project was done jointly with Dr. N. Theodoropoulou. I will present separately the data for both the samples fabricated and measured by me and the totality of samples made by both of us. I will compare the latter with theoretical predictions.

1.6.3 Antiferromagnetic spintronics studies

In chapter 4, I present experiments to search for spintronics effects with antiferromagnets based on predictions by Macdonald and coworkers [13, 14, 15, 16]. As the predictions assume perfect samples, such experiments are needed to see if any such effects can be seen in real 'imperfect' samples. I first give an overview of the predictions of the spintronics effects with antiferromagnets. I then briefly describe the samples and the point contact measurement technique. Finally I describe two separate projects:

- 1. Effects of current on exchange bias in exchange biased spin valves.
- 2. Search for antiferromagnetic giant magnetoresistance effects.

In these projects, I prepared the multilayer samples, which were measured by our collaborators at the University of Texas, Austin.

1.6.4 Conclusions

In chapter 5, I present the conclusions of our studies.

Chapter 2

Current perpendicular to the plane magneto-transport studies in metallic multilayers

In this chapter we present our CPP magneto-transport experiments in metallic multilayers to determine the interface parameters - - $2AR^*$ and γ for new metal pairs. We determined these interface parameters either to compare with theoretical calculations or to search for metal pairs better suited for devices.

The chapter is organized as follows. In section 2.1, we present the sample fabrication, processing, and measurement techniques, and the types of samples we use to determine the parameters of interest. In section 2.2, we describe the models and equations of CPP-MR that we use in our analysis. In section 2.3 we present the experiments to estimate the specific interface resistance of Al/Ag and Al/Cu. In section 2.4 we present the experiments to determine $2AR^*$ and γ for F/Al (F:Py (= Ni₈₄Fe₁₆), Co, Fe & Co₉₁Fe₉) and F/N: Py/Pd, Fe/V, Fe/Nb, and Co/Pt interfaces. Lastly, we present experiments to study the effect of Cu/Al/Cu sandwiches on A Δ R.

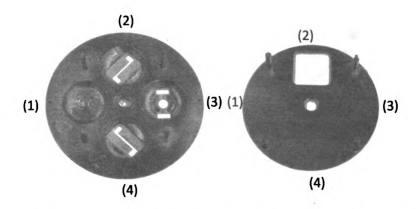


Figure 2.1: The left figure is a mask used to deposit CPP samples. The CPP substrate holder can accommodate 1 substrate and the mask is changed from position (1) - - the closed position, where the substrate is not exposed, to positions (2)-(4) to deposit the superconducting crossed strips and the multilayers. The figure on the right shows a CIP mask. The CIP substrate holder can accommodate 2 substrates. The mask is rotated to bring the open position (shown as position (2)), over position (1) to expose one substrate. After the deposition, the open position is brought over position (4) to close the substrates. To deposit the second substrate, the open position is moved over position (3). After the deposition, the open position is brought back over position (2) to close the substrates.

2.1 CPP-MR Samples

2.1.1 Fabrication, Processing & Measurement

The multilayers in our experiments were deposited onto half inch square Si(100) substrates in an ultra high vacuum compatible, computer controlled, sputtering system. The chamber can accommodate up to six sputtering targets (four 2.25" and two 1" targets). The substrate plate can hold up to eight CPP or sixteen CIP samples. Our chamber has a unique in-situ mask changing capability. The chamber is pumped for up to two days to get vacuum $\sim 2\text{-}3\times 10^{-8}$ torr. The partial pressure of the residual gases is checked by residual gas analyzer (RGA). The chamber has a Meissner trap, operating at 77 K, to freeze most of water vapor and achieve a vacuum $\sim 1\text{-}2\times 10^{-8}$ torr. The substrate temperature is maintained between -30° C to 30° C during the

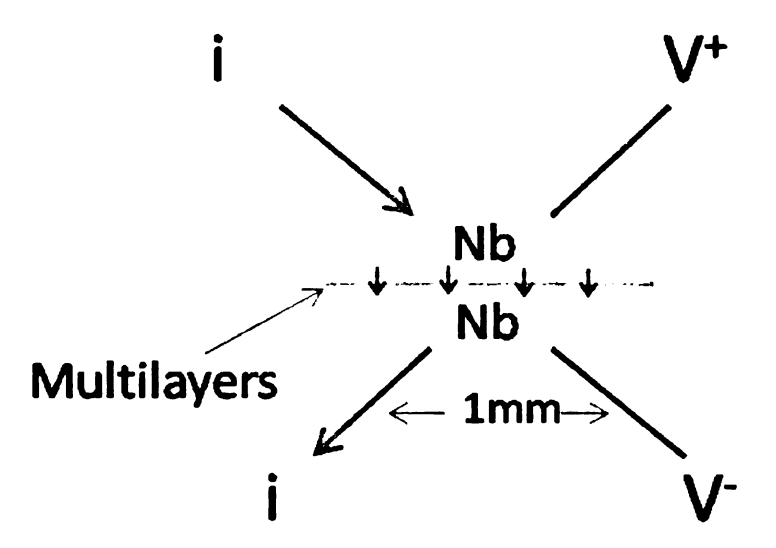


Figure 2.2: A cartoon showing uniform current density in our samples - - where the thickness of the multilayer is much smaller than the widths of the Nb strips.

run.

Ar is slowly introduced in the chamber at a rate to maintain the pressure ~ 2.5 $\times 10^{-3}$ torr. The targets are then turned on and stabilized for ~ 20 -30 mins. The sputtering rate for each target is measured by two computer controlled Sycon film thickness monitors before depositing each sample. The mask of the sample is rotated to the desired open position, see below, by an in-situ mask changing mechanism. The chamber has a shutter plate on top of the targets, which is set to an open position before sputtering. The samples are then deposited by moving sequentially over the desired targets. The movement of the shutter and the substrate plate are both computer controlled. After depositing a sample, the shutter plate is set to close position and then the mask of the sample is rotated to the close position. The samples use two types of masks - - one each for CPP and CIP samples. As shown in the left in figure 2.1, the mask on the CPP substrate holder has four positions to: (1) close, (2) deposit a bottom superconducting strip, (3) deposit the actual multilayer, (4)

deposit a top crossed superconducting strip, and (1) close again. The mask on the CIP substrate holder has two positions: (a) to deposit the layers, and (b) to close. Further details of our chamber can be found in refs [83, 84, 85, 86, 87, 88].

For CPP transport we need a uniform current flowing through the multilayers. We also need to control the contact resistance to reliably measure the resistance of the multilayer. To address these issues, we use \sim 1mm wide, 150 nm thick crossed superconducting (= Niobium (Nb) in our samples) strips sandwiching the multilayers of interest (see figures 2.2 and 2.3). These strips remain superconducting at our measuring temperature (\sim 4.2 K) and magnetic fields well above 1 kG. The fringing currents for our sample geometry are small (see appendix in ref [85]). The superconducting strips limit the lead and the contact resistance to the field independent superconductor/metal interface resistance, which for typical Fs - - Py, Co, Cog₁Fe₉ and Fe - - is AR $_{Nb/F} \sim 3 \pm 0.5$ f Ωm^2 [89, 85, 90, 49, 52, 50, 53, 54].

In CPP transport, the parameter of interest is the specific resistance - - area (A) times resistance (R). The area (A) through which the CPP current flows is determined by taking the product of the widths (measured using a Dektak surface profiler) of the two crossed Nb strips sandwiching the 'active' multilayer (see figure 2.3). The typical uncertainty in the area is $\sim \pm 5$ %. Our resistance measurements are done at 4.2 K. We mount our sample on a quick dipper - - a stick with sample holder, superconducting magnet, and some measurement electronics including a superconducting quantum interference device (SQUID) null detector. The quick dipper is dipped slowly into a standard 60 lt. helium dewar to reach the measuring temperature. As the CPP resistance is ultra low (\sim few n Ω), we use an ultra sensitive SQUID based poten-

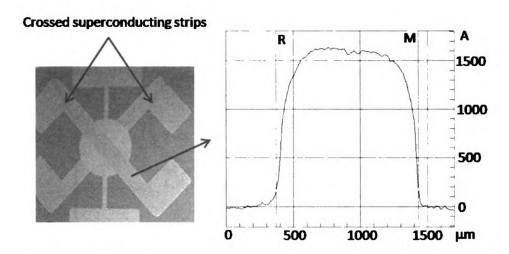


Figure 2.3: The left figure is an optical image of the sample used for CPP measurements. The right figure shows the profile of typical superconducting crossed strip, measured by a Dektak profilometer, that is used to compute the area through which the CPP current flows.

tiometer bridge circuit (see figure 2.4) to measure the sample resistance [91]. We pass a known current $I_{Cpp}=100$ mA through the sample, and the current through the reference resistor is varied to balance the potentiometer setup. R_{Cpp} can then be determined using the relation $R_{Cpp}=(\mathrm{R}_{Ref}\mathrm{xI}\mathrm{R}_{ef})/(I_{CPP})$. Further details of the measurement setup are explained in earlier theses of our group (see [84, 86, 87, 88]).

2.1.2 Types of samples

For our CPP-MR studies we use the following four types of samples to determine the parameters of interest.

- · We use two types of multilayers, which we define next.
 - 1. F/N multilayers : These samples have the structure, SC/ $[F(t_F)/N(t_N)]_n/F(t_F)/SC$, where SC (= Nb) is 150 nm thick superconductor, $t_F=6$ nm is the fixed thickness of the ferromagnet, t_N is the variable

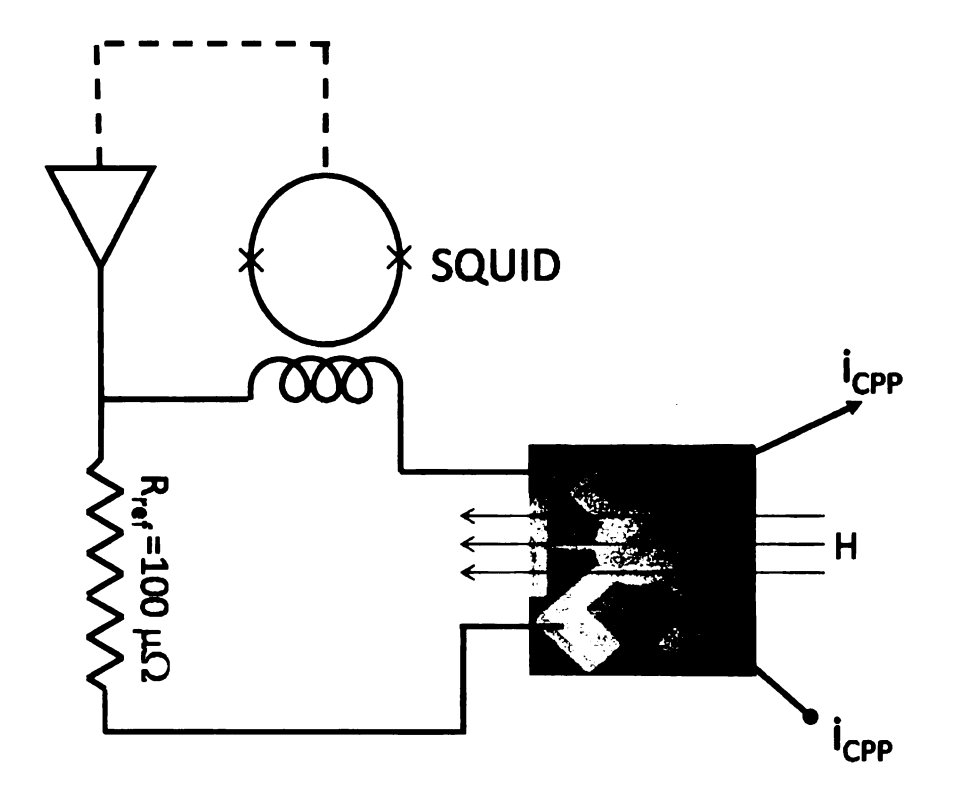


Figure 2.4: A schematic drawing of the ultra sensitive superconducting quantum interference device (SQUID) based potentiometer bridge circuit that we use to measure the resistance of our CPP samples.

thickness of the non-magnetic metal, and n is the number of bilayers. These samples have a fixed total thickness i.e. $n(t_F+t_N)+t_F=$ constant (= 366 nm for our experiments). With the total thickness fixed, an increase in the number of bilayers corresponds to an increase in the number of interfaces and a decrease in t_N . The ferromagnets next to the superconductors are deposited to eliminate any proximity effects. For some samples with Py, for better switching we use a buffer Cu layer (\sim 5nm), between the superconductors and the adjacent Py layers. This buffer Cu layer becomes superconducting due to the proximity effect. These F/N

multilayer samples are used to determine $2AR_{F/N}^*$. Figure 1.6 shows a typical CPP measurement for such an F/N multilayer. As mentioned in section 1.2.3, the maximum resistance - - (AR $^{\circ}$) for the as-grown state often corresponds closely to an anti-parallel (AP) state. The minimum resistance (AR(P)) at saturating field corresponds to the parallel (P) state. Sweeping the field back from saturation leads to an intermediate maximum of resistance AR(peak).

- 2. N1/N2 multilayers: These samples are similar to F/N multilayers but with bilayers of F and N replaced by bilayers of N1 and N2. The structure for such samples is SC/F(10nm)[N1(t_{N1})/N2(t_{N2})]_n/F(10nm)/SC where t_{N1} and t_{N2} are the thicknesses of the non-magnetic metals. We keep t_{N1} = t_{N2}. The total thickness of the bilayer structure, n(t_{N1} + t_{N2}) is kept constant (= 360 nm for our experiments). These samples are used to determine the specific interface between two non-magnetic metals N1 and N2 (2AR_{N1/N2}). Because of the large separation of the F layers, MR is negligible for these N1/N2 multilayer samples. Figure 2.5 shows typical AR data for such an N1/N2 multilayer.
- The third kind of samples are exchange biased spin valves (EBSVs). These samples are used to get a clean AP state to let us reliably determine $A\Delta R$, and hence γ . In principle, the EBSVs could be used to extract $AR_{F/N}^*$ too. But the sample to sample fluctuations in the overall sample resistance are of the order of $AR_{F/N}^*$ for a single layer, making it hard to reliably extract $AR_{F/N}^*$

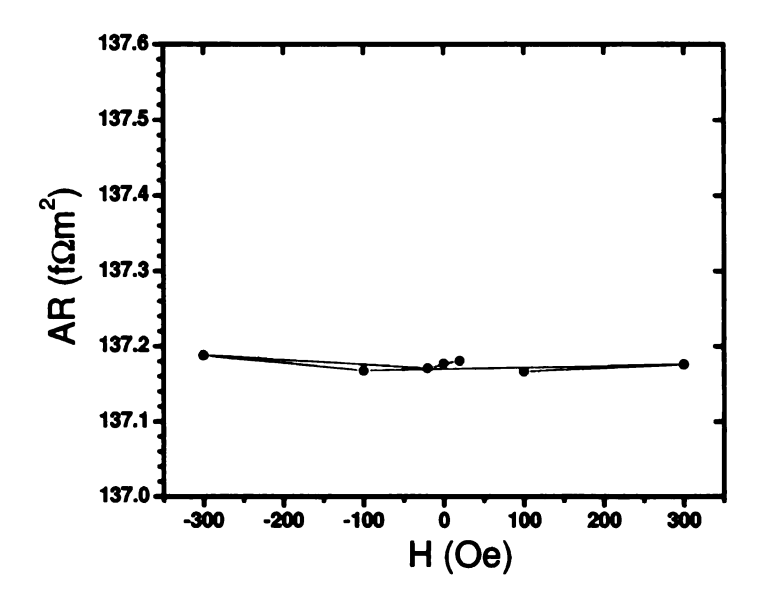


Figure 2.5: AR vs. H plot for a typical N1/N2 multilayer sample.

from the EBSVs. We will thus use the multilayers to determine $AR_{F/N}^*$, and the EBSVs to determine γ , and then check both for internal consistency. The EBSVs have the structure SC/AFM(t_{AFM})/ $F(t_F)/N(t_N)$ / $F(t_F)/SC$, where AFM denotes the antiferromagnet (= FeMn for our samples) and t_{AFM} is the fixed AFM thickness = 8nm. As discussed in section 1.2.3, the AFM is used to pin the adjacent F layer by exchange bias. For better growth of the AFM, we grow a buffer Cu layer (\sim 5nm), which becomes superconducting due to the proximity effect, between the superconductors and the adjacent antiferromagnet or ferromagnet. The exchange bias between the AFM and the adjacent F is induced by heating the sample above the blocking temperature of the AFM (\sim 453K for FeMn), applying a small magnetic field (\sim 200 Oe) for \sim 2 min, and then cooling quickly in the presence of the field.

• The fourth kind of samples are multilayers within EBSVs [46]. They have the form SC/AFM(8nm)/ $F(t_F)$ / Cu(10nm)/[$N1(t_{N1})/N2(t_{N2})$] $_n$ / Cu(10nm)/ $F(t_F)$ / SC. These samples are pinned similar to EBSVs. These samples are used to extract the interface resistance of the non-magnetic metals N1 and N2, but with the advantage of control of the magnetic states. Thus, these samples can also be used to determine the spin flip parameter ($\delta_{N1/N2}$) - - a parameter representing the amount of spin flipping at the N1/N2 interface.

For both the EBSV, and the multilayer within EBSV samples, the data look similar. Figure 1.7 shows a typical example of EBSV data.

In addition to the CPP samples, we also made some CIP samples. These were usually used for resistivity measurements of metals and alloys, using the Van der Pauw technique presented in appendix A.1. However, some CIP samples were also used for magnetization measurements, X-ray diffraction studies, and for structural studies using high resolution transmission electron microscopy (HRTEM) and electron energy loss spectroscopy (EELS).

2.2 CPP-MR: Models and equations

At cryo temperatures, the physics of CPP-MR involves asymmetric scattering of electrons, with moments along or opposite to the direction of F moment, within the F layers and at F/N interfaces, relaxation of the spins as electrons traverse the layers [33, 92, 45], and spin flip scattering at the interfaces. Unless specifically mentioned, we neglect any spin flipping at the interfaces. In two cases, our analysis had to include spin flipping at the F/N interfaces to achieve internal consistency.

At higher temperatures CPP-MR can be affected by another process called spinmixing, where momentum is transferred between the two channels, for example by electron magnon scattering [92]. The effects of spin mixing are taken into account by incorporating a corresponding resistivity term, $\rho_{\uparrow\downarrow}$ [92]. Such spin-mixing can be neglected at our cryogenic measuring temperature ~ 4.2 K.

As mentioned in section 1.3, the set of parameters for bulk and interfaces which we will focus upon are ρ_F^* and β for the bulk F-metals and $\operatorname{AR}_{F/N}^*$ and γ for the F/N interfaces. As also discussed in section 1.3, the bulk parameters for the commonly used F metals and alloys sputtered in our system were determined earlier by previous researchers of our group [50, 52, 56, 57]. In all cases but one, our measured resistivities agree with prior measurements. So we use the values of β from those earlier studies [50, 52, 56, 57]. The one exception, Fe, will be discussed in section 2.4.1.

The models that we employ for analysis of CPP-MR data depend upon the relative thicknesses and spin diffusion lengths, l_{sf} , of the individual layers. (Note: We will highlight the equations that we later use for analysis.)

2.2.1 Two current series resistor model (2CSR) - - No Spin relaxation in the layers and no spin flipping at the interfaces

For infinite spin diffusion lengths, we use a two current series resistor (2CSR) model [31, 34, 33]. In this model, the two spin channels traverse the sample independently, and add in parallel. Using equations 1.4 and 1.5, we have $\rho_F^{\uparrow} = 2\rho_F/(1+\beta)$ and $\rho_F^{\downarrow} = 2\rho_F/(1-\beta)$. Similarly using equations 1.6 and 1.7 we have $\mathrm{AR}_{F/N}^{\uparrow} = 2\mathrm{AR}_{F/N}/(1+\gamma)$ and $\mathrm{AR}_{F/N}^{\downarrow} = 2\mathrm{AR}_{F/N}/(1-\gamma)$. For the two spin channels acting in parallel,

we have

$$\frac{1}{AR_{AP}} = \frac{1}{AR_{AP}^{\downarrow}} + \frac{1}{AR_{AP}^{\uparrow}} \tag{2.1}$$

and

$$\frac{1}{AR_P} = \frac{1}{AR_P^{\downarrow}} + \frac{1}{AR_P^{\uparrow}} \tag{2.2}$$

For two F layers in the AP configuration, separated by a N layer, as shown in figure 1.4, we have

$$AR_{AP}^{\uparrow} = \rho_F^{\uparrow} t_F + AR_{F/N}^{\uparrow} + \rho_N^{\uparrow} t_N + AR_{F/N}^{\downarrow} + \rho_F^{\downarrow} t_F$$
 (2.3)

and

$$AR_{AP}^{\downarrow} = \rho_F^{\downarrow} t_F + AR_{F/N}^{\downarrow} + \rho_N^{\downarrow} t_N + AR_{F/N}^{\uparrow} + \rho_F^{\uparrow} t_F$$
 (2.4)

Note that equations 2.3 and 2.4 are identical - - $AR_{AP}^{\downarrow} = AR_{AP}^{\uparrow}$.

As $\rho_N^{\uparrow} = \rho_N^{\downarrow} = 2\rho_N$, using equations 2.3 and 2.4 in equation 2.1, we have

$$AR_{AP} = \frac{\rho_F^{\downarrow} t_F + AR_{F/N}^{\downarrow} + 2\rho_N t_N + AR_{F/N}^{\uparrow} + \rho_F^{\uparrow} t_F}{2} \tag{2.5}$$

Using expressions for $AR_{F/N}^*$ and ρ_F^* (equations 1.4 and 1.6) and adding the superconductor / ferromagnet interface resistance, we have

$$AR_{AP}^{Total} = 2AR_{S/F} + 2\rho_F^* t_F + 2AR_{F/N}^* + \rho_N t_N$$
 (2.6)

Note that the use of 2AR*, γ , ρ_F^* and β simplifies the equation. For a multilayer with n bilayers, we similarly have (neglecting the difference between n and $n\pm 1$),

$$AR_{AP}^{Total} = 2AR_{S/F} + n[\rho_F^* t_F + \rho_N t_N + 2AR_{F/N}^*]$$
(2.7)

The analysis for the parallel configuration is more complicated, but can be expressed in a simple form in terms of AR_{AP} . For n bilayers we have [34]

$$A\Delta R = AR_{AP}^{Total} - AR_{P}^{Total} = \frac{n^{2} [\beta \rho_{F}^{*} t_{F} + 2\gamma_{F}/N^{AR}_{F}^{*}/N]^{2}}{AR_{AP}^{Total}}$$
(2.8)

. To determine the interface resistance between two non-magnetic metals N1, N2, we use multilayers of the form N1/N2 (see section 2.1). For these N1/N2 multilayers, the two F layers are separated by ~ 360 nm of N1/N2 layers, such that the spin information is not carried from one F to the other. The total specific resistance of the sample, can thus be determined by simply adding the contributions from the bulk of the layers and interfaces. We thus have (neglecting the difference between n and $n\pm 1$)

$$\begin{array}{rcl} {\rm AR}_{N1/N2}^{T} & = & 2{\rm AR}_{S/F} + {\rm AR}_{F/N1} + {\rm AR}_{F/N2} + 2\rho_{F}{\rm t}_{F} + \\ & & & & & & & & \\ & & & & & & & \\ & & & & & & & \\ & & & & & & \\ & & & & & & \\ & & & & & & \\ & & & & & \\ & & & & & \\ & & & & & \\ & & & & & \\ & & & & & \\ & & & & & \\ & & & & \\ & & & & \\ & & & & \\ & & & & \\ & & & \\ & & & & \\ & & & \\ & & & \\ & & & \\ & & & \\ & & & \\ & & & \\ & & & \\ & &$$

where $t_T = 360$ nm is the total fixed thickness of the N1/N2 multilayer region.

For an EBSV, in a quasi 2CSR model, we have

$$AR_{AP}^{EBSV} = AR_{S/AFM} + \rho_{AFM} t_{AFM} + AR_{AFM/F} + 2\rho_F^* t_F + 2AR_{F/N}^* + \rho_N t_N + AR_{F/S}$$
 (2.10)

and

$$A\Delta R = \frac{4[\beta \rho_F^* t_F + \gamma A R_{F/N}^*]^2}{A R_{AP}^{EBSV*}}$$
 (2.11)

where $A\Delta R = AR_{AP} - AR_{P}$ and AR_{AP}^{EBSV*} is AR_{AP}^{EBSV} (equation 2.10) without the $AR_{S/AFM}$ and $\rho_{AFM}t_{AFM}$ terms, which would be included in the full 2CSR model, but are removed due to strong spin flipping at the AFM/F interface.

2.2.2 Valet-Fert (VF) model - - Including spin relaxation in the layers, and sometimes spin flipping at the interfaces.

Including spin relaxation in the layers complicates the analysis. The general way to analyze the CPP-MR data is to use the Valet-Fert formalism [33] which is based on a Boltzmann equation approach. We limit the model to zero temperature to eliminate spin mixing (electron-magnon spin flip scattering). The model assumes a single parabolic conduction band for both the F and N layers. The analysis yields that the 'Boltzmann correction' to the transport equations is proportional to λ_t/l_{sf} (equation 9 in ref [33]). For $\lambda_t/l_{sf} \ll 1$, the transport equations reduce to the macroscopic equations (equations 10, 11 of ref [33])

$$\frac{e}{\sigma_s} \frac{\partial J_s}{\partial z} = \frac{\overline{\mu}_s - \overline{\mu}_{-s}}{l_{sf}^2} \tag{2.12}$$

$$J_S = \frac{\sigma_S}{e} \frac{\partial \overline{\mu}_S}{\partial z} \tag{2.13}$$

where -e is the charge of the electron, z is the direction of propagation of current (perpendicular to layer planes), s is the spin direction and J_s , μ_s , σ_s and l_{sf} are respectively the current density, electrochemical potential, conductivity and spin diffusion length for spin s. $\Delta \mu = \overline{\mu}_s - \overline{\mu}_{-s}$, is the spin accumulation, representing the difference between the *spin up* and *spin down* Fermi energies. Equation 2.12 implies that spin-flip processes balance the spin accumulation related to spin divergences. Equation 2.13 is just Ohm's law.

These two equations form the basis of the analysis. However, the actual equations which are used for numerical fits to analyze the data are based on equations C1-C6

given in appendix C of ref [33]. Those equations yield the spin dependent electrochemical potentials, spin dependent current densities, and the electric field. These quantities are then matched at the layer boundaries using boundary conditions, to determine the resistance of the multilayer. Due to complexity of the equations, we do not reproduce them here. The Valet-Fert equations reduce to equations from the 2CSR model in the limit $l_{sf} \gg t_F, t_N$.

For the limit $t_F \gg l_{sf}^F$ & $t_N \ll l_{sf}^N$, for an EBSV of the form AF/F/N/F, the inclusion of spin relaxation effects does not always require one to numerically solve the Valet-Fert equations. Under these conditions, Fert et al (see equation A1 in ref [93]) showed that $A\Delta R$ can be expressed as

$$A\Delta R = \frac{4[\beta \rho_{F}^{*} l_{sf}^{F} + \gamma A R_{F/N}^{*}]^{2}}{2\rho_{F}^{*} l_{sf}^{F} + 2A R_{F/N}^{*} + \rho_{N} t_{N}}$$
(2.14)

Equation 2.14 shows that for the limit, $t_F\gg l_{sf}^F$, only the central region composed of N plus l_{sf}^F thicknesses of the adjacent F layers is 'active' and contributes to A Δ R. Note the similarity of equation 2.14 with the 2CSR equation 2.11, but with only the contribution from active region in the denominator and t_F also replaced by l_{sf}^F in the numerator.

Using the approach in equation 2.14, the total resistance of an N1/N2 multilayer in an EBSV with $\mathbf{t}_F \gg \mathbf{l}_{sf}$, to a first approximation, can be modeled by a 2CSR model where only the l_{sf}^F thickness of the F layer is 'treated' as active. For multilayer in EBSV samples, we find, (neglecting the difference between n and $n\pm 1$)

$$AR_{AP}^{T} = AR_{S/AFM} + \rho_{AFM}t_{AFM} + AR_{AFM/F} + 2\rho_{F}^{*}l_{sf}^{F} + 2\rho_{F}(t_{F} - l_{sf}^{F}) + 2AR_{F/Cu}^{*} + 2\rho_{Cu}t_{Cu} + AR_{Cu/N1} + AR_{N2/Cu} + n(\rho_{N1}t_{N1} + \rho_{N2}t_{N2}) + 2nAR_{N1/N2} + AR_{F/S}$$
(2.15)

To incorporate spin-flipping at the interfaces, the interfaces are modeled as a layer with a thickness \sim few monolayers with appropriate resistivity and spin diffusion length. The spin flipping at the interfaces is then evaluated from numerical solutions, usually expressed in terms of a parameter δ which relates to the spin flip probability P as P = 1 - $e^{-\delta}$ [46, 45].

2.3 Experiments involving Non-magnetic metal (N1) / Non-magnetic metal (N2) interfaces

We estimate the specific interface resistance (AR) of two new N1/N2 metal pairs -Al/Ag and Al/Cu. We use N1/N2 multilayer samples in both studies. To have an
independent estimate for Al/Cu, we have also done additional studies using multilayer
in EBSV samples. In both of these projects, I was helped by Dr. N. Theodoropoulou.
I expect to be the first author in the eventual publication of these projects.

2.3.1 Specific interface resistance of sputtered Al/Ag interfaces

2.3.1.1 Introduction

Xu et al [60] recently predicted that the specific interface resistance of Al/Ag should show strong effects of orientation and alloying. We undertook this project to estimate $2AR_{Al/Ag}$ (111) and compare it with the calculations. A complication recognized in advance was the likelihood of significant interdiffusion. We did X-ray diffraction (XRD) to know the orientations of the sputtered Al (FCC) and Ag (FCC) layers in our multilayer. We expected the sputtering growth to be in the close packed (111) planes. To estimate diffusion of Ag in Al, and vice versa, we have done diffusion calculations, which are described in Appendix A.2. The calculations predict interdiffusion of a few monolayers in a week - - typical time between sputtering and measurement.

2.3.1.2 Experiment

A. Structure Determination

To check both the layering of our multilayers, and the crystallographic orientation

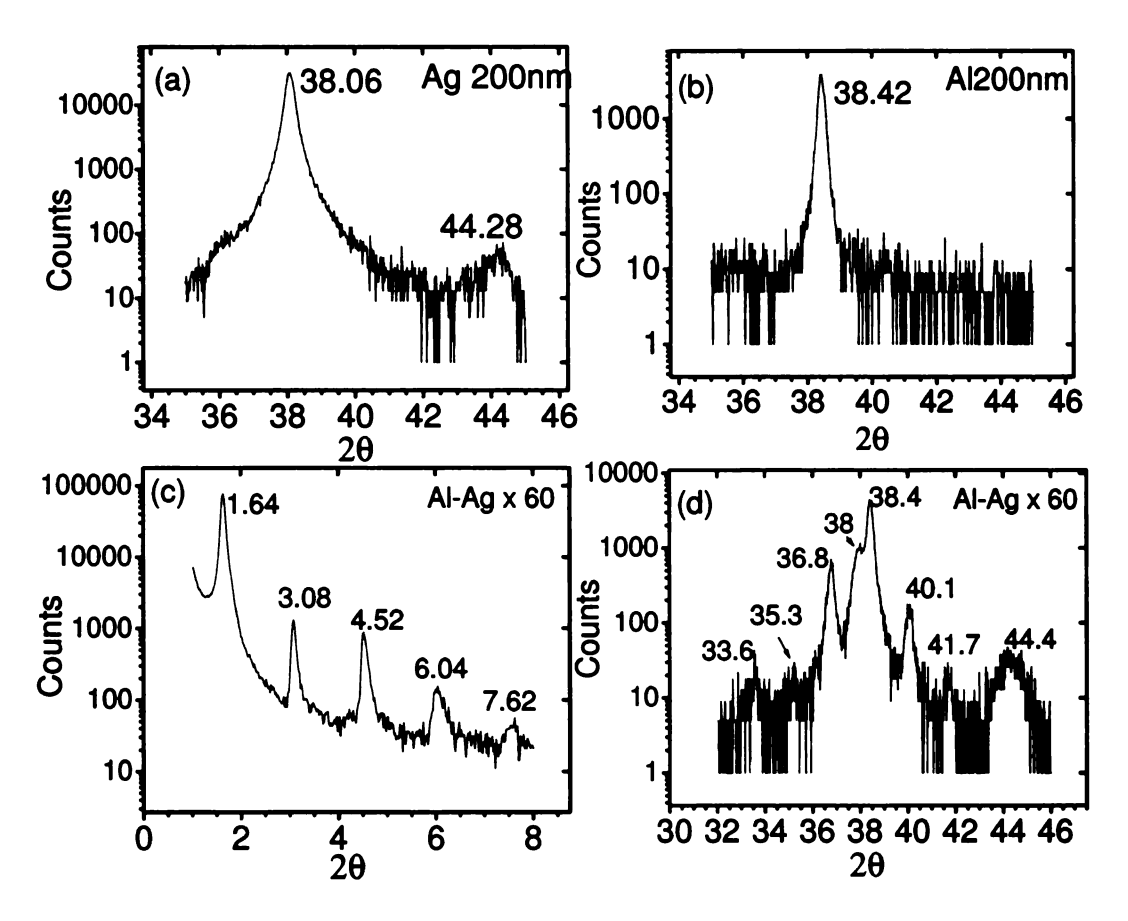


Figure 2.6: X-ray diffraction patterns for: (a) Ag, (b) Al, (c) and (d) Al/Ag bilayers (n = 60).

of the sputtered layers, we have done X-ray diffraction (XRD) on the multilayer samples and on separately grown 200nm thick films. For sputtering, generally the metals grow in the closed packed planes - - (111) for FCC and (011) for BCC. We show the diffraction peaks for 200nm thick films of Ag and Al in figure 2.6 (a) and (b). In figure 2.6 (c) and (d) we show the low angle (for layering information) and high angle diffraction patterns for a real Al/Ag multilayer sample with n = 60.

For Ag (FCC) and Al (FCC) the lattice constants (a $_{Ag}$ and a $_{Al}$) are 4.09 Å and

4.05 Å respectively [24]. Using Bragg's law

$$2d_{hkl}sin(\theta) = m\lambda \tag{2.16}$$

where θ is the angle between the incident ray and the scattering planes, m is an integer determined by the order, λ is the wavelength of the x-rays (=1.54 Å for the Cu k α line used in our XRD setup), d_{hkl} is the spacing between the planes in the atomic lattice, and hkl are the miller indices. For cubic crystals we have

$$d_{hkl}(cubic) = \frac{a}{\sqrt{h^2 + k^2 + l^2}}$$
 (2.17)

Using equation 2.17 and the lattice constants of bulk Ag and Al, we have d_{111}^{Ag} (calc) = 2.34 Å and d_{111}^{Al} (calc) = 2.36 Å.

Using θ from figures 2.6 (a) and (b), in equation 2.16, we get $d_{Ag} = 2.36 \pm 0.06$ Å and $d_{Al} = 2.34 \pm 0.06$ Å. The agreements of the calculated values with the bulk values show that our samples grow in the expected (111) direction.

The low angle XRD data for a multilayer sample with n=60 are shown in figure 2.6 (c). The low angle XRD data give a bilayer thickness $d_{bilayer}=5.9\pm0.3$ nm, in good agreement with the sputtered bilayer thickness = 6 nm. The high angle XRD pattern of the same sample shows a main peak at $\sim 38^{\circ}$ corresponding closely to the angles expected for Al (111) and Ag (111). The satellites peaks in figure 2.6 (d) are due to the modulation by the bilayer structure, shown also in figure 2.6 (c).

B. Transport data

To estimate $2AR_{Al/Ag}$ we use N1/N2 multilayer samples with the structure Nb (150) / Co(10) / [Al (t_{Al}) / Ag (t_{Ag})]_n / Co(10) / Nb(150) where n is the number of bilayers (all layer thicknesses are in nm). We keep $t_{Al} = t_{Ag}$ and the total 'effective'

thickness $\mathbf{t}_{Total} (= n(t_{Al} + t_{Ag}))$ fixed (= 360 nm). For \mathbf{t}_{Total} fixed and $\mathbf{t}_{Al} = \mathbf{t}_{Ag}$, we have $\mathbf{t}_{Al}^{Total} = \mathbf{t}_{Ag}^{Total} = \mathbf{t}_{Total}/2$, implying that the bulk contributions from the Al and Ag layers do not change with n. Barring unexpected complications, or time dependent interdiffusion, an increase in n corresponds solely to addition of more interfaces.

We measure the resistivities of our sputtered Al and Ag using the Van Der Pauw [55] technique, discussed in appendix A.1. For Al, we get $\rho_{Al}=4.1\pm1.6$ n Ω m which is comparable to the earlier estimates of ρ_{Al} (old) = 5 n Ω m [45]. For Ag, we get $\rho_{Ag}=15.6\pm4.3$ n Ω m which, probably due to a new target, is larger than the earlier estimate of ρ_{Ag} (old) = 7 ± 2 n Ω m [46, 45].

We use equation 2.9 to estimate $2AR_{Al/Aq}$,

$$AR_{Al/Ag}^{T} = [2AR_{Nb/Co} + AR_{Co/Al} + AR_{Co/Ag} + 2\rho_{Co}t_{Co} + \rho_{Al}\frac{t_{T}}{2} + \rho_{Ag}\frac{t_{T}}{2}] + [2nAR_{Al/Ag}]$$
(2.18)

where from independent earlier measurements, we have $2AR_{Nb/Co} = 6\pm 1$ f Ω m² [89, 34, 85], $AR_{Co/Ag} = 0.18\pm 0.02$ f Ω m² [85], $AR_{Co/Al} \sim 5.5\pm 0.1$ f Ω m² [94] (also see section 2.4.1), and $\rho_{Co} = 61.5 \pm 8.5$ n Ω m (see table 2.2).

Figure 2.7, shows the measured $AR_{Al/Ag}^T$ as a function of n (solid symbols). The $AR_{Al/Ag}^T$ data initially rise linearly with n and then saturate after a certain value of n. The saturation is expected for finite interface widths. Even without interdiffusion, in other sputtered multilayer samples the interfaces have typical width ≤ 1 nm. For large n, the individual layer thicknesses become comparable to the width of the interface, and the bilayer structure is lost. In the overlap limit, the multilayers

can be approximated with a 50-50 uniform alloy. For the data, shown in figure 2.7, $AR_{Al/Ag}^T$ saturates at large n. We roughly estimate the resistivity of Ag(50)-Al(50) alloy using Nordhiem's rule [95], $\Delta \rho(c) = (\Delta \rho_c/\Delta(c))_{avg}(c/100\%)(100\%$ -c), where c is the concentration and $(\Delta \rho_c/\Delta(c))_{avg}$ is the average resistivity of Ag in Al and Al in Ag per % concentration. $(\Delta \rho_c/\Delta(c))_{avg}$ can be calculated from the values listed in ref [95]. Using those values, we get $\rho_{Ag(50)Al(50)} \sim 360 \pm 30 \text{ n}\Omega\text{m}$. For $t_{Total} = 360\text{nm}$, this value gives a specific resistance $(\rho t) \sim 130 \text{ f}\Omega\text{m}^2$. Adding to it the contributions from the rest of the layers, we get the specific resistance of the total sample, with Ag(50)-Al(50) alloy $\sim 140 \text{ f}\Omega\text{m}^2$ which is comparable to the observed $AR_{Al/Ag}^T$ at saturation in figure 2.7.

We fit a straight line to the linear regime of our data as shown in figure 2.7. The intercept from the fit is compared to the estimate calculated from independently determined terms in the first square bracket in equation 2.18 for consistency. The terms in the first square bracket in equation 2.18 give an intercept $\sim 16.3 \pm 1.3$ $f\Omega m^2$. The intercept from the fit is 19.4 ± 3.7 $f\Omega m^2$. Both estimates agree within mutual uncertainties. The slope of the fit gives $2AR_{Al/Ag}(\exp) = 1.4 \pm 0.2$ $f\Omega m^2$.

Our calculations of diffusion distances for Ag in Al show a few Å diffusion in a week at 300 K. To look for the effect of interdiffusion on the resistances of our samples, we remeasured two samples after a long time (~ 2 yrs). We show AR for these samples as open symbols in figure 2.7. The resistances of the samples show a significant increase. Although these increases in resistance are likely due to significant alloying, x-ray diffraction studies on these samples still showed clear bilayer structure. Thus the open symbol samples are not simply random alloys.

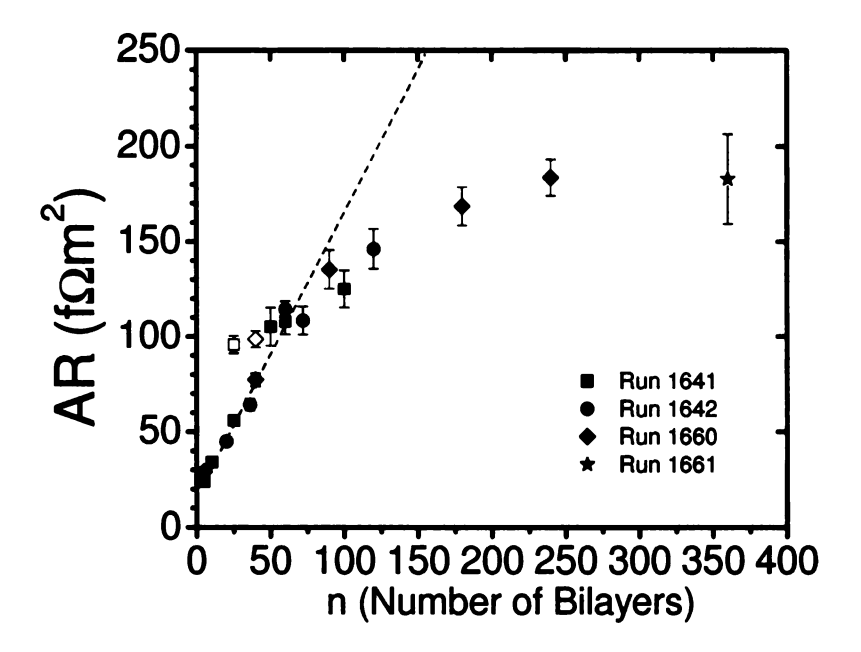


Figure 2.7: AR^T vs. n for Al/Ag Multilayers. The different symbols denote different sputtering runs. The filled symbols are initial measurements and the open symbols are measurements after significant time (~ 2 years).

2.3.1.3 Results

We first compare our experimentally determined estimate of $2AR_{Al/Ag}$ (111) = 1.4 ± 0.2 $f\Omega m^2$ with the calculated value for perfect interfaces $2AR_{Al/Ag}$ (calc (111))=0.64 $f\Omega m^2$ [60]. The calculated value for perfect interfaces is much less than our experimental estimate. Since our diffusion distance calculations indicate likely interdiffusion, around 1nm in a week for Ag in Al, we also compare our estimate of $2AR_{Al/Ag}$ with calculations for 2 and 4 layers of a disordered 50-50 alloy. For 2 layers of disorder, the calculated $2AR_{Al/Ag} = 0.92 \ f\Omega m^2$ [60], is still less than our experimental estimate. However, the calculation for 4 layers of disorder, $2AR_{Al/Ag} = 1.315 \ f\Omega m^2$ [96], is close to our estimate. The good agreements between prior measurements and

calculations for metal pairs with $\Delta a/a < 1\%$, shown in the top part of table 1.2 suggest that calculations for such pairs are likely to be reliable. If so, we infer that the specific interface resistance of our sputtered Al/Ag multilayers is probably affected by interdiffusion.

2.3.1.4 Conclusions

Based on the calculations of $2AR_{Al/Ag}$ by Xu et al [60], showing sensitivity to orientation and disorder, we undertook to experimentally estimate the specific interface resistance of (111) oriented Al/Ag interfaces. We estimate $2AR_{Al/Ag}$ (111) = 1.4 \pm 0.2 $f\Omega m^2$. Our estimate is larger than the calculated value for perfect interfaces or for interfaces with 2 monolayer of interfacial disorder. However, our estimate is close to calculations with 4 monolayer of disorder, $2AR_{Al/Ag}(4)$ layer disorder (111)) = 1.31 $f\Omega m^2$ [96]. This latter agreement suggests that the specific interface resistance for our sputtered Al/Ag multilayers has significant contributions from interface disorder. Consistent with such a conclusion, the sample resistances also increased with time, showing some additional intermixing.

2.3.2 Specific interface resistance of sputtered Al/Cu interfaces

2.3.2.1 Introduction

In this section, we estimate the specific interface resistance of sputtered Al/Cu interfaces to: (a) help us understand our Cu/Al/Cu experiments (presented in section 2.4.3), and (b) compare with $2AR_{Al/Ag}$.

2.3.2.2 Experiment

A. Structural Studies

To check the orientation of the layers of our samples we did X-ray diffraction on a real multilayer sample with n = 60. The lattice constant of bulk Al is $a_{Al} = 4.05$ Å [24] which corresponds to $d_{111}^{Al}(\text{calc}) = 2.36$ Å or $2\theta \sim 38.5$ °. Similarly, for Cu we have $a_{Cu} = 3.61$ Å [24] which corresponds to $d_{111}^{Cu}(\text{calc}) = 2.084$ Å or $2\theta \sim 43.37$ °. The X-ray diffraction data in figure 2.8 shows peaks around 38° and 43.3°, indicating that our multilayers grow in the expected (111) orientation.

The diffusion distances, listed in table A.1, show that Cu in Al diffuses a fraction of an Å in a week at 295 K but around a few nm in minutes at 450 K, the temperature at which our multilayer in EBSV samples are processed. To look for such interdiffusion, we collaborated at Michigan State University and Arizona State University, for structural analysis of our samples using high resolution transmission electron microscopy (HRTEM) and electron energy loss spectroscopy (EELS). As these studies were not done by me, I will just summarize the results instead of presenting the details. To look for effects due to changes in structure with the relative thickness of Al, the

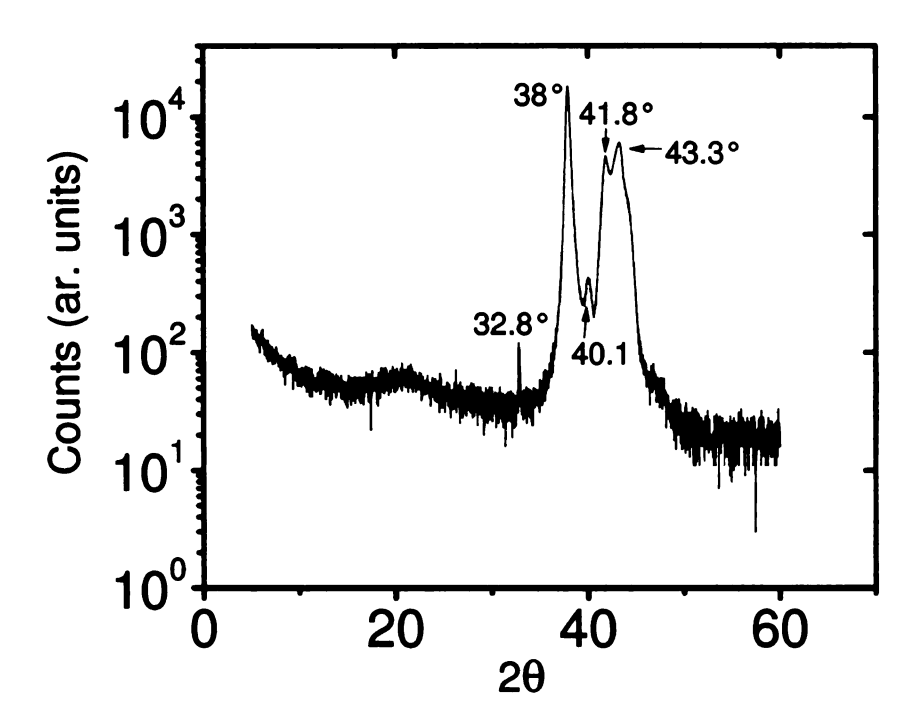


Figure 2.8: X-ray diffraction pattern for an Al/Cu multilayer sample with n=60. structural studies were done on two types of multilayers (a) $Nb(150)/[Cu(8)Al(10)]_{20}$ /Nb(2) (structure with thick Al) and (b) $Nb(150)/[Cu(5)Al(3)]_{45}$ /Nb(2) (structure with thin Al), where all layer thicknesses are in nm. To look at the thermal stability effects, some of the type (a) samples were studied after annealing. The studies show

- For thick Al (Cu(8nm) Al(10nm) multilayers) significant interdiffusion was observed. The data suggests inclusions of ordered intermetallic phases. The Al rich layers were identified to include Al₂Cu, and the Cu rich regions were identified to include AlCu₃. Annealing to 450 K caused more interdiffusion.
- For thin Al (Cu(5nm)Al(3nm) multilayers) the data suggests less intermixing and less intermediate phase formation. The Al rich layers were identified to

Sample	Resistivity at 4.2 K	Remarks
	$(\mathrm{n}\Omega\mathrm{m})$	
Al ₂ Cu (Thin)	360 ± 60	Unannealed
Al ₂ Cu (Thin)	48 ± 15	Annealed at 450 K for 1 min
Al ₂ Cu (Thin)	46.5	Annealed at 450 K for 10 min
Al ₂ Cu (Thick)	89.1	Unannealed
Al ₂ Cu (Thick)	74.5	Annealed at 450 K for 1 min
Al ₂ Cu (Thick)	45.4	Annealed at 510 K for 15 min
AlCu ₃ (Thin)	276 ± 6	Unannealed
AlCu ₃ (Thin)	253 ± 7	Annealed at 450 K for 1 min
AlCu ₃ (Thin)	241	Annealed at 450 K for 10 min
AlCu ₃ (Thin)	222	Annealed at 480 K for 15 min
AlCu ₃ (Thin)	201	Annealed at 510 K for 15 min
AlCu ₃ (Thick)	262	Unannealed
AlCu ₃ (Thick)	74.5	Annealed at 450 K for 1 min
AlCu ₃ (Thick)	45.4	Annealed at 510 K for 15 min

Table 2.1: Van der Pauw resistivities of sputtered Al and Cu multilayers with atomic % similar to Al₂Cu and AlCu₃. In some cases, only a single sample has been processed at different temperature and time. In others, multiple samples have been processed similarly. In the latter case, the specified uncertainties are the standard deviation of measurements.

include some ordered intermetallics, probably mostly Al₂Cu, and the Cu rich regions were identified to be FCC Cu.

We thus find that Al and Cu do intermix significantly and probably form some intermetallic phases.

Since the most likely Al/Cu intermetallic phases are Al₂Cu and AlCu₃, a knowledge of the resistivities of Al₂Cu and AlCu₃ could be useful to understand our data. We sputtered CIP multilayer films with very thin layers of Al and Cu to promote uniform alloy formation. We kept the Al and Cu layer thicknesses such as to keep the atomic % corresponding to Al₂Cu and AlCu₃. For Al₂Cu, we sputtered, [Al(1.76)Cu(0.63)]₈₅ (thin layers) and [Al(3.52)Cu(1.26)]₄₅ (thick layers) and for AlCu₃ we sputtered Al(0.6)Cu(1.28)]₁₁₀ (thin layers) and [Al(1.2)Cu(2.56)]₅₅

(thick layers). All layer thicknesses in nm. We then did Van Der Pauw resistivity measurements [55], using the technique discussed in appendix A.1. Further, we annealed some samples for different times and at different temperatures to look for the effects of thermal stability on the resistivity. We present our resistivity data in table 2.1. The Al₂Cu (thin) unannealed samples show a higher resistivity than that of Al₂Cu (thick) unannealed samples. The resistivity of both Al₂Cu (thin) and Al₂Cu (thick) samples drop to $\sim 46 \text{ n}\Omega\text{m}$ upon annealing which we tentatively associate with ordered Al₂Cu intermetallic. The AlCu₃ (thin) unannealed samples have comparable resistivity to AlCu₃ (thick) unannealed samples. Annealing causes a significant drop in the resistivity of AlCu₃ (thick) but only a mild drop in the resistivity of AlCu₃ (thin). Apparently the AlCu₃ (thin) samples do not form good ordered intermetallics.

Apart from measuring the resistivity, we also did X-ray diffraction (XRD) on these samples to check the structures. The structure of Al_2Cu is tetragonal with lattice parameters a=b=6.04 Å, c=4.86 Å and the close packed plane is 110 (from the TEM studies). The structure of $AlCu_3$ is BCC with a=2.95 Å, which corresponds to $2\theta=43.3$ °.

For a tetragonal structure, the spacing between the planes in the atomic lattice (\mathbf{d}_{hkl}) is given as

$$d_{hkl}(Tetragonal) = \sqrt{\left\{\frac{h^2 + k^2}{a^2} + \frac{l^2}{c^2}\right\}^{-1}}$$
 (2.19)

For Al₂Cu, d₁₁₀ = 4.27 Å corresponding to $2\theta = 20.77^{\circ}$, using Bragg's law. We show the x-ray diffraction data for one of the Al₂Cu (thin) samples (both unannealed and annealed for 1 min at 180 °C) in figure 2.9. The solid line represents the unannealed

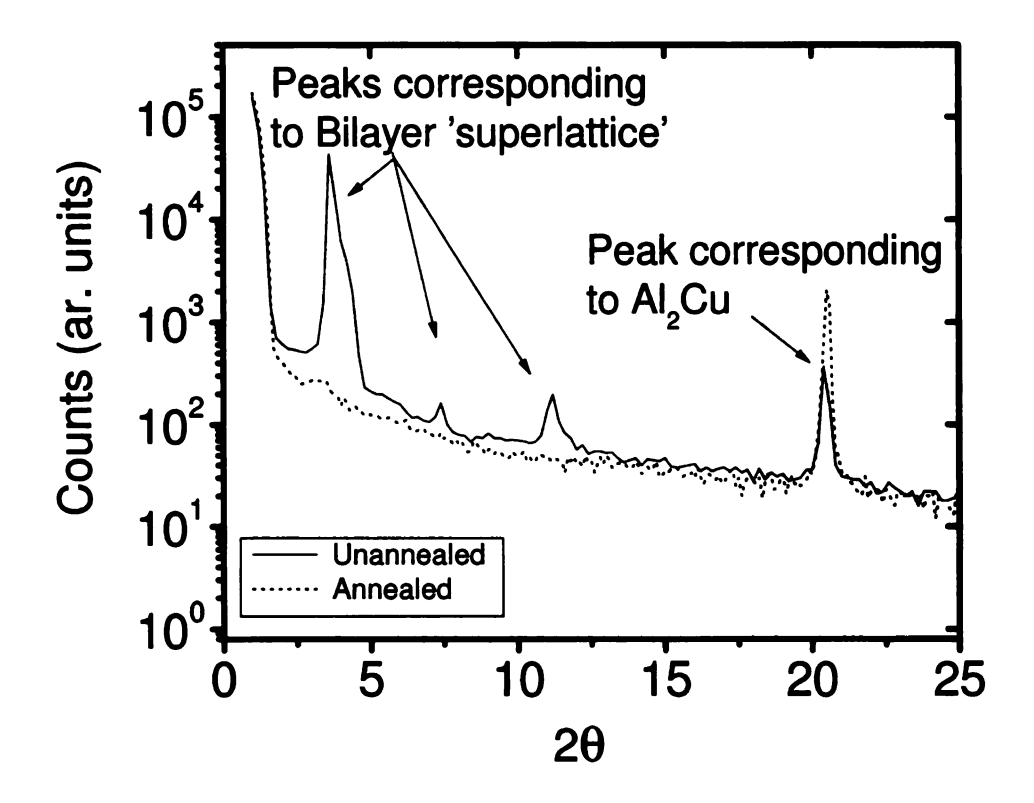


Figure 2.9: X-ray diffraction of a multilayer with very thin Al and Cu layer in an attempt to make an Al_2Cu (thin) sample. The dashed curve is the diffraction pattern after annealing at 450 K for 1 min.

sample and the dashed line is for the annealed sample. For the unannealed sample, the XRD pattern shows a peak $\sim 21^\circ$ which corresponds to Al_2Cu . We also get low angle peaks which correspond to the bilayer superlattice of the multilayers, indicating that the Al and Cu are not completely intermixed. However, upon annealing, as shown by the dashed line in figure 2.9 the low angle peaks are lost and the peak for $Al_2Cu \sim 21^\circ$ becomes more pronounced, suggesting strong intermixing and ordering between Al and Cu layers upon annealing. We see similar behavior for other Al_2Cu thin and thick samples. The x-ray diffraction data for one of the $AlCu_3$ (thin) samples (both unannealed and annealed for 1 min at 180 $^\circ$ C) are shown in figure 2.10. Same

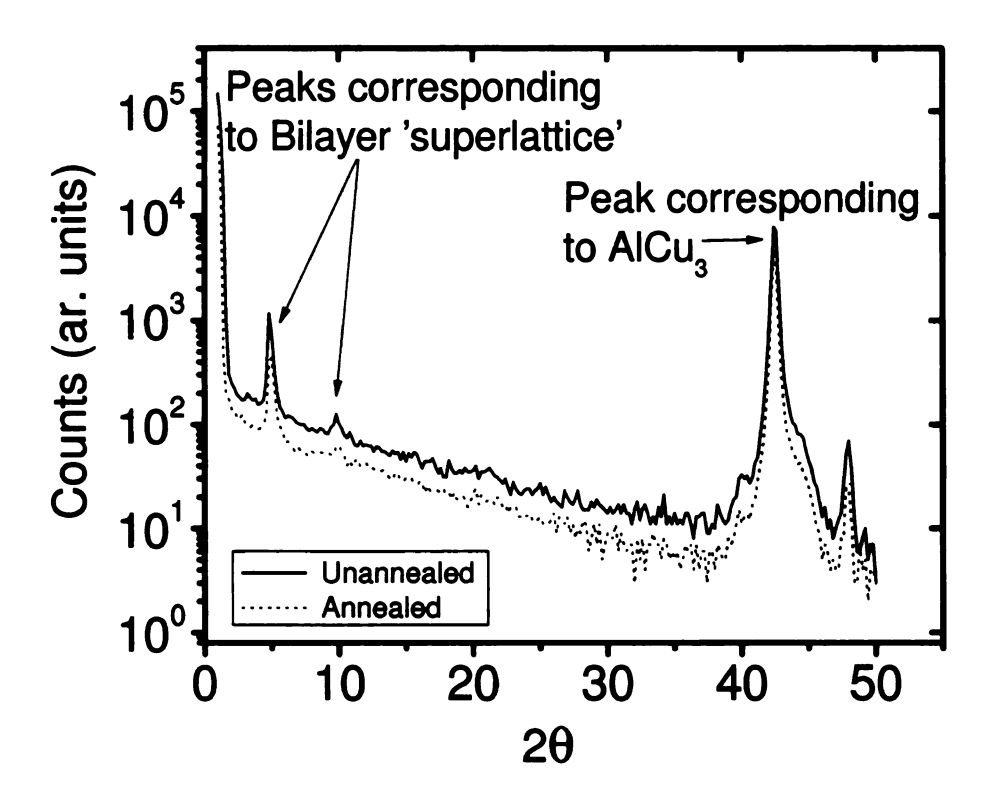


Figure 2.10: X-ray diffraction of a multilayer with very thin Al and Cu layer in an attempt to make an AlCu₃ (thin) sample. The dashed curve is the diffraction pattern after annealing at 450 K for 1 min.

as above, the solid line represents the unannealed sample and the dashed line the annealed sample. The peak at $\sim 43^\circ$ corresponds to AlCu₃. The low angle peaks correspond to the bilayer superlattice of the multilayers. In contrast to Al₂Cu, the low angle peaks do not disappear upon annealing, suggesting that the annealing for 1 min at 180 $^\circ$ C does not cause much more interdiffusion between Al and Cu. Thin and thick AlCu₃ samples give similar XRD patterns.

B. Transport data

To estimate $2AR_{Al/Cu}$ we first used N1/N2 multilayer samples with the structure $\dot{Nb}(150)/$ Py(10)/ [Al(t_{Al})/Cu(t_{Cu})]_n/ Py(10)/ Nb(150) (all thicknesses in nm),

where n is the number of bilayer repeats. For these multilayer samples, we keep \mathbf{t}_{Al} = \mathbf{t}_{Cu} and the total 'effective' thickness $\mathbf{t}_T = n((\mathbf{t}_{Cu} + \mathbf{t}_{Al}))$ as fixed (= 360 nm). We thus have $\mathbf{t}_{Al}^{Total} = \mathbf{t}_{Cu}^{Total} = \mathbf{t}_{T}/2$, so that contribution from the bulk of Al and Cu remains the same irrespective of n. By increasing n we thus add more and more interfaces, letting us estimate $2AR_{Al/Cu}$ from the expected linear growth of the total sample resistance with increasing n. As noted in section 2.3.1, when the number of bilayers becomes so large that the individual layer thicknesses become thinner than the interface thickness, the bilayer structure will be lost and the AR should approach a value approximated by a disordered 50-50 uniform alloy. We thus expect an initial increase in total sample specific resistance with n, but eventual saturation after a certain n. Our Al/Cu multilayer data, however, show a significant drop in AR_T at large values of n, and then saturation at a lower value of AR.

To independently check our estimate of $2AR_{Al/Cu}$, and to look for possible direct effects of annealing at 450 K on $2AR_{Al/Cu}$, we decided to also try a different technique. In this technique, we used multilayers within EBSV samples (samples of the 'fourth kind' as given in section 2.1) with the structure Nb(150)/ Cu/(5)/ FeMn(8)/ Py(24)/Cu(10) [Al(t_{Al})/ Cu(t_{Cu})]_n Cu(10) / Py(24)/ Cu (5)/ Nb(150) where n is the number of bilayers and all layer thicknesses are in nm. Whereas our N1/N2 multilayers have no MR, the multilayer in EBSV samples have the advantage of giving clean anti-parallel states. Such states let us also look for evidence of spin flipping at the Al/Cu interface. These samples are pinned as described in section 2.1 . For these multilayer in EBSV samples, we keep $t_{Al} = t_{Cu}$ fixed (=3nm) and define $t_T = n((t_{Cu} + t_{Al}))$. By increasing n for these samples, we thus add both bulk Al and Cu

as well as more interfaces. However, as the resistivities of Al or Cu are both only ~ 5 \pm 1 n Ω m, the contribution from bulk is both known and small, so that we can correct for it. We can thus determine $2AR_{Al/Cu}$ by measuring the total sample resistance as a function of n.

We use equation 2.9 for the MLs

$$AR_{AP}^{T} = 2AR_{Nb/Py} + AR_{Py/Al} + AR_{Py/Cu} + 2\rho_{Py}.10nm + \rho_{Al}.180nm + \rho_{Cu}.180nm + 2nAR_{Al/Cu}$$
 (2.20)

and modified 2CSR equation 2.15 (t_{Py} \gg l_{sf}^{Py} = 5.5 nm [50]) for the ML in EBSVs

$$AR_{AP}^{T} = AR_{Nb/FeMn} + \rho_{FeMn}.8nm + AR_{FeMn/Py} + 2\rho_{Py}^{*} l_{sf}^{Py} + 2\rho_{Py}^{*} l_{sf}^{Py} + 2\rho_{Py}^{*} (24nm - l_{sf}^{Py}) + 2AR_{Py/Cu}^{*} + 2\rho_{Cu}.10nm + n(\rho_{Al}.3nm + \rho_{Cu}.3nm) + 2nAR_{Al/Cu} + AR_{Py/Nb}$$
 (2.21)

to analyze our data.

For our analysis, we use $2AR_{Nb/Py}=6\pm 1$ f Ωm^2 [50], $l_{sf}^{Py}=5.5\pm 1$ nm [50], $AR_{Nb/FeMn}=1.0\pm 0.6$ [50, 49, 97], $AR_{FeMn/Py}=1.0\pm 0.4$ [50, 49, 97], $2AR_{Py/Cu}^*=1\pm 0.1$ f Ωm^2 [50, 32], $\gamma_{Py/Cu}$ [50, 32] = 0.7 \pm 0.1, $\beta_{Py}\sim 0.76$ [50, 32], $AR_{Py/Al}=4.25\pm 0.5$ [94] (also see section 2.4.1), and $\rho_{FeMn}=875\pm 50$ n Ω m [49, 54] determined from independent earlier measurements.

We can thus estimate $2AR_{Al/Cu}$ by studying total sample resistance as a function of n. This procedure neglects any formation of intermetallics.

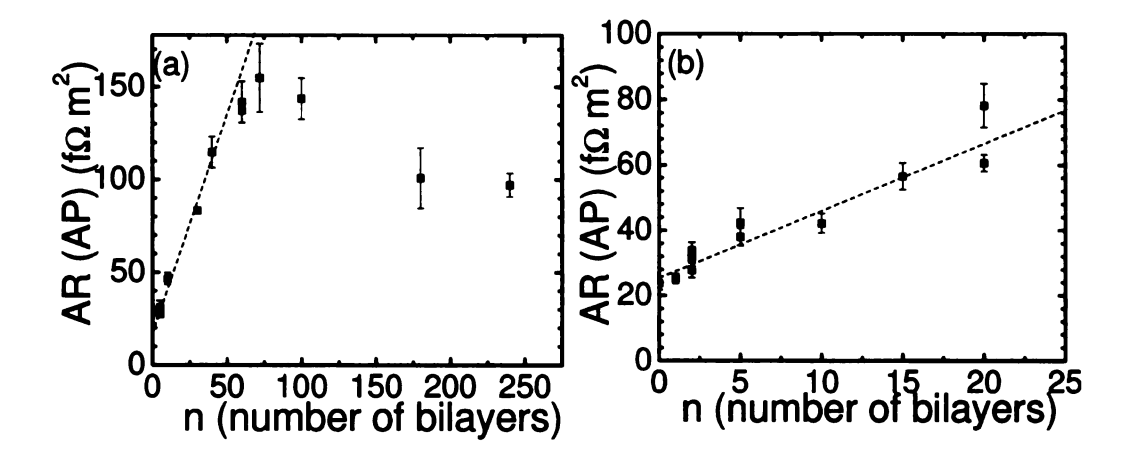


Figure 2.11: Plot of AR against n for: (a) Multilayer samples, and (b) Multilayer in EBSV samples.

2.3.2.3 Results

We show our transport data as AR^{Total} against n in figure 2.11(a) for multilayer samples and figure 2.11(b) for multilayer in EBSV samples. The expected behaviors of our multilayer samples are an initial linear rise of AR with n and then a saturation due to formation of a uniform alloy. We see for our multilayer data in figure 2.11(a), that AR initially grows linearly with n but in contrast to an expected saturation, the AR drops at large values of n. The expected saturation of AR corresponds to the formation of a uniform disordered alloy with $\rho t >$ maximum AR. Usually the resistivity of a disordered alloy is much more than the ordered alloy. For Al and Cu, one possibility is that we get one or more ordered uniform alloys, giving us a drop in AR at saturation. Another possibility might be a disordered alloy, but with a smaller ρt than anticipated with the saturation model. The saturation AR for our Al/Cu multilayers $\sim 100 \text{ } f\Omega m^2$. Assuming uniform alloying between Al/Cu, this

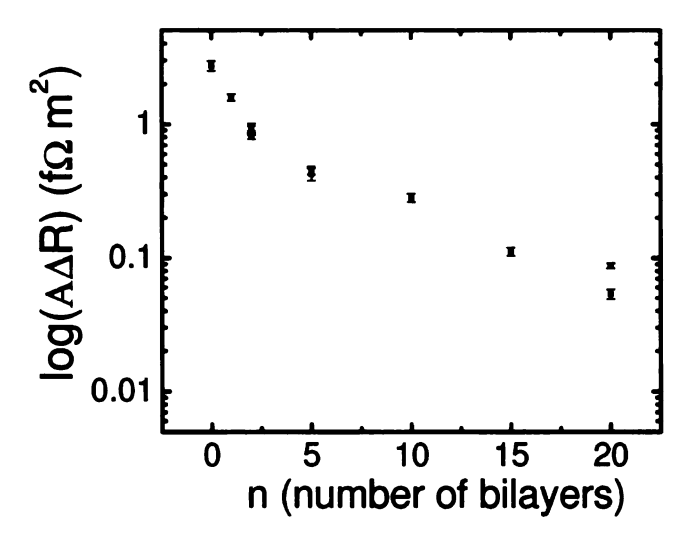


Figure 2.12: Plot of $A\Delta R$ against n for multilayer in EBSV samples.

corresponds to a alloy with resistivity $\sim 300 \text{ n}\Omega\text{m}$ (using the relation $\rho t = AR$). This resistivity is close to the measured resistivities of unannealed Al₂Cu and AlCu₃, listed in table 2.1. However, the unannealed Al₂Cu and AlCu₃ samples show layering and thus the resistivities have contribution from interfaces. A detailed explanation of the drop in AR is not yet clear.

We fit a straight line to the data in the linear regime of figure 2.11 (a). We first compare the intercept from the fit to the calculated value from equation 2.20. The calculations give an intercept = $14.7 \pm 1.4 \text{ f}\Omega\text{m}^2$. The fit gives an intercept = $18 \pm 1 \text{ f}\Omega\text{m}^2$. The value of intercept from the fit almost overlaps with the value from the calculations. From the fit, we get $2AR_{Al/Cu}^{ML} = 2.3 \pm 0.3 \text{ f}\Omega\text{m}^2$.

We fit a straight line to the data in figure 2.11 (b). We first compare the intercept from the fit to calculated value from equation 2.21. The fit gives an intercept \pm 1 f Ω m². Equation 2.21 gives an intercept \pm 1 f Ω m². We again find

that the value of the intercept from the fit almost overlaps with the value from the calculations. From the fit, we get $2AR_{Al/Cu}^{MLinEBSV}=2.1\pm0.2~\mathrm{f}\Omega\mathrm{m}^2$.

We see that the estimates of $2AR_{Al/Cu}$ from both the techniques agree within uncertainties. We can thus combine the two estimates to get an average $2AR_{Al/Cu}$ = $2.2 \pm 0.2 \text{ f}\Omega\text{m}^2$.

Gundrum et al [98], using a technique involving much thicker layers, estimated $2AR_{Al/Cu} = 3.6^{+2.2}_{-0.8} \text{ f}\Omega\text{m}^2$ (scaled to 4.2 K) using thermal conductivity + Lorenz number analysis at room temperature on magnetron sputtered samples. Our estimates are smaller than that of Gundrum et al [98], probably due to the different measurement procedures.

As mentioned in section 2.2, the multilayer in EBSV samples, can be used to estimate spin flipping at the N1/N2 interface. Figure 2.12 shows the plot of log(A Δ R) against n for our multilayer in EBSV samples. Our preliminary analysis gives spin flip parameter, $\delta_{Al/Cu} \sim$ 0.05, but detailed analysis is in progress.

2.3.2.4 Conclusions

To help us understand our Cu/Al/Cu data, presented in section 2.4.3, we have estimated the specific resistance of Al/Cu interfaces $2AR_{Al/Cu}$ using two different techniques involving: (a) multilayer, and (b) multilayer in EBSV samples. The multilayer samples gave $2AR_{Al/Cu}$ (ML) = 2.3 ± 0.3 f Ω m² and the multilayer in EBSV samples gave $2AR_{Al/Cu}$ (ML in EBSV) = 2.1 ± 0.2 f Ω m². Combining the two, we have $2AR_{Al/Cu} = 2.2 \pm 0.2$ f Ω m². Comparing to $2AR_{Al/Ag}$ (= 1.4 ± 0.2 f Ω m²), our estimated $2AR_{Al/Cu}$ is ~ 1.5 larger, but still of the same order. To look for

possibility of spin flipping at Al/Cu interface, we used A Δ R from the multilayer in EBSV samples. Our initial analysis gives spin flip parameter, $\delta_{Al/Cu}\sim 0.05$.

Our diffusion distance calculations (see appendix A.2), predicted strong diffusion of Cu in Al. To look for such interdiffusion, we collaborated for structural studies, which confirmed strong interdiffusion between Al and Cu. Our measured interface resistance thus probably has contributions from interface disorder.

2.4 Experiments involving Ferromagnetic / Nonmagnetic metal interfaces

As mentioned in section 1.6, for potential use of CPP-MR in devices, it would be desirable to have large values of the interface parameters - $-2AR_{F/N}^*$ and γ . As mentioned in section 1.3, standard F/N pairs have $2AR_{F/N}^* \sim 1 \text{ f}\Omega\text{m}^2$ and $\gamma \sim 0.7$ -0.8 [85, 99, 43, 50, 49, 54, 53].

In this section, we present our studies on new F/N metal pairs in hopes of finding metal pairs with large values of $2AR_{F/N}^*$, γ and the product $2AR_{F/N}^*\gamma$. We have determined the interface parameters of two new sets of metal pairs: (a) F/Al (F:Py, Co, Fe & Cog₁Fe₉), and (b) F/N - - Py/Pd, Fe/V, Fe/Nb and Co/Pt.

As mentioned in section 1.3, values of β and spin diffusion lengths (l_{sf}) of the metals that we use in these studies have been previously estimated. To use those estimates in our analysis, we check that our sputtered metals have resistivities (at 4.2 K) in agreement with those earlier estimates. We have done Van der Pauw (VDP) resistivity measurement (see appendix A.1) for the metals we use in this present study. We list our resistivities in table 2.2. We also list the old value of the resistivities for comparison. Apart from Fe, our estimates are in agreement with the earlier estimates to within mutual uncertainties. We will thus use the corresponding values of l_{sf} and β from those studies (listed in table 1.1). For Fe, probably due to a new sputtering target, we get an average residual resistivity $\rho_{Fe} = 104 \pm 11 \text{ n}\Omega\text{m}$, which is much larger than the earlier estimate of $\rho_{Fe} \sim 40 \text{ nm}$. To cross check the new VDP ρ_{Fe} , we independently determined it using CPP samples as discussed in appendix

Element	$ ho new \ (ext{n}\Omega ext{m})$	$ ho_{m{old}} \ ({ m n}\Omega{ m m})$	
Py(FCC)	94 ±5	120±40 [49]	
Co(FCC)	61.5 ± 8.5	60±9 [49]	
$Co_{91}Fe_{9}$	70	$70 \pm 10 \ [45, 52]$	
Fe(BCC)	104 ±11	40±10 [53]	
Al(FCC)	4.5 ± 1	5±1 [45]	
Nb(BCC)	86	$78 \pm 15 [46, 45]$	
V(BCC)	125±25	$105 \pm 20 [46, 45]$	
Pd(FCC)	43±1	$40 \pm 3 [48, 45]$	
Pt(FCC)	35 ± 10	26±1 [48]	

Table 2.2: The structure, measured resistivity (ρ_{new}) , and earlier estimates of resistivity, ρ_{old} , for metals used in the present study. The residual resistivities of V and Nb were measured at 12K and all others were measured at 4.2K. For Co, one of the samples gave $\rho_{Co}=230~\mathrm{n\Omega m}$, but the surface was mottled, leading us to neglect it. For Fe, we did CIP measurements and an independent CPP based estimation (see text); the values and uncertainties listed are the average of both measuring techniques. For Co/Pt analysis, we use the ρ_{Pt} (and corresponding l_{sf}) from [48], which is within mutual uncertainties of our new measurement, but smaller than the values in [45].

A.3. From the CPP measurement technique, we get $\rho_{Fe}=95\pm6$ n Ω m which is similar to our new Van der Pauw CIP measurements. For ρ_{Fe} we list the average of estimates from both VDP and CPP techniques. For this new higher resistivity of Fe, the corresponding values of $l_{sf}=5\pm1$ nm and $\beta=0.77\pm0.04$ were determined by a collaborator (see appendix in ref. [94]). For our analysis, we also use $2AR_{Nb/F}=6\pm1$ f Ωm^2 (F:Py, Co, Co₉₁Fe₉, and Fe) [89, 85, 90, 49, 52, 50, 53, 54] determined from independent earlier measurements.

2.4.1 Specific resistance and scattering asymmetry parameter of F/Al interfaces (F:Py (= $Ni_{84}Fe_{16}$), Co, Fe & $Co_{91}Fe_{9}$)

This project was done in collaboration with Dr. N. Theodoropoulou, T. Haillard and R. Acharyya. It has led to four papers: (a) on interface parameters of Py/Al, in which I am the second author [100]; (b) on interface parameters of Co/Al, Fe/Al and Cog₁Fe₉, in which I am the second author [101]; (c) on structural studies of Co/Al and Py/Al in which I am the fourth author [102]; and (d) a long one with details of all our results and analysis, in which I am the first author [94].

2.4.1.1 Introduction

As mentioned in section 1.6, we started our F/Al studies with Py/Al. We were motivated by Py/Al nanopillar studies by Garcia et al [81] that suggested significantly different spin-dependent scattering properties of Py/Al interfaces from those of standard metal pairs. We found large $2AR_{Py/Al}^* \sim 8.5 \text{ f}\Omega m^2$ but small $\gamma \sim 0.025$. The large value of $2AR_{Py/Al}^*$ looked promising, so we extended our studies to other F = Co, Fe & Co₉₁Fe₉, with Al in the hopes of finding large values of both $2AR_{F/Al}^*$ and γ . For simplicity of presentation, in this thesis, we discuss the Py/Al data along with the other F/Al data. The diffusion distances between Al and F metals under study suggested interdiffusion, so we re-measured some samples after significant time and after annealing ($\sim 450 \text{ K}$). We find that the resistances are somewhat unstable with both aging and annealing. The changes in the resistance with aging and annealing suggest structural changes in the samples, which motivated us to collaborate for structural studies using advanced TEM, HRTEM and EELS.

2.4.1.2 Experiment

We used a combination of multilayer and EBSV samples to determine the interface parameters - - 2AR* and γ . First, we use multilayer data to estimate 2AR*. The structure of our multilayer samples is Nb(150)/ Cu(5)/ [F(6)/Al(t_{Al})]_n/ F(6) / Cu(5)/ Nb(150), where all layer thicknesses are in nm. Given that the largest A Δ R in figure 2.13 (b) is still only a small fraction (\sim 2%) of the total AR at n=30 in figure 2.13 (a), we expect that AR° should be a decent first approximation to AR(AP).

To reliably determine γ , we need clear anti-parallel states, for which we use EBSV samples with the structure Nb(150)/ Cu(5)/ FeMn(8)/ F(24)/Al(t_{Al})/ F(24) / Cu(5)/ Nb(150), where all layer thicknesses are in nm. These EBSV samples were pinned using the procedure given in section 2.1. Except for Co, all of the Fs in our EBSVs have $l_{sf} \ll t_F$ (using the values of l_{sf} from table 1.1). Thus, except for Co, we can use the closed form equation 2.14 for analysis. For Co, we do numerical fits to the full Valet Fert theory.

2.4.1.3 Results

Figure 2.13 (a) shows our multilayer data (open symbols) in a plot of $AR^{\circ} \approx AR(AP)$ vs n. The straight lines are numerical fits to the data. We also show data points for Py/Cu (solid symbols) for comparison. Figure 2.13 (a) shows that the AR° values for all four F-Al metal pairs (open symbols) are similar to each other, but much larger than those for Py/Cu. To get $AR^{\circ} \approx AR(AP)$ values, figure 2.13 (b) shows sample hysteresis curves (for n=30) for each F/Al pair. The AR(H)s are largest at H=0 (as-grown state) for CoFe/Al and Co/Al, marginal for Fe/Al and not clear for Py/Al.

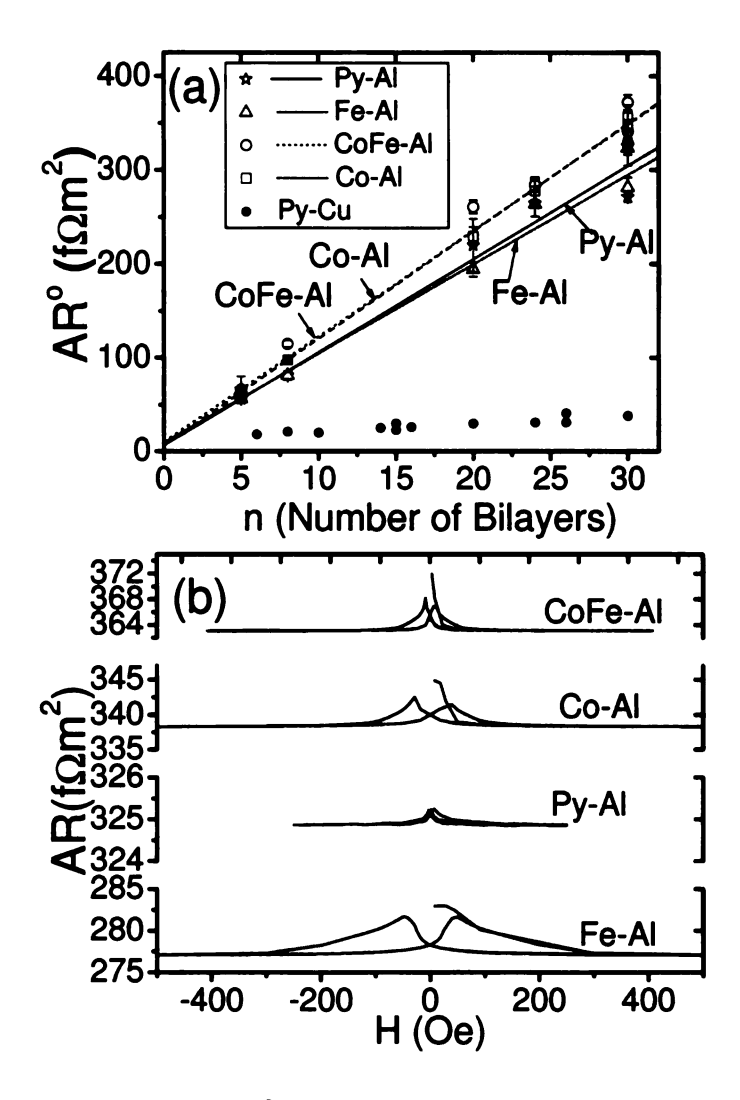


Figure 2.13: (a) AR(AP) \approx AR° (the maximum resistance for the as-sputtered state) against n for F/Al (F=Py, Co, CoFe(=Co₉₁Fe₉), Fe) multilayers. The straight lines are fits to the data. The Py/Cu data (filled circles) are shown for comparison. (b) AR vs H hysteresis loops for some of the n=30 multilayers in (a) F/Al multilayer data. The figure is from [94].

The AR(H)s decrease at high fields to a lowest 'saturation' value of AR(P), and then rise to an intermediate maximum - - AR(peak).

Figure 2.14 (a) shows $A\Delta R$ vs t_{Al} for our EBSVs. The open symbols represent the data for F-Al. For comparison, we also show the data for Py/Cu as solid symbols. To estimate $A\Delta R$, figure 2.14 (b) shows the hysteresis curves for F/Al samples with t_{Al} =10 nm.

Except for Co, we estimate $\gamma_{F/Al}$ using the values of A Δ R from figure 2.14 (a) in equation 2.14. For Co, we do numerical fits to the full VF theory.

To check our estimated values for internal consistency, we insert them into equation 2.8 to calculate $A\Delta R$ for multilayers with n=30, and compare the results with the data in figure 2.13. The calculated $A\Delta Rs$ ($\sim 6 \pm 1 \text{ f}\Omega m^2$) for CoFe/Al and Fe/Al are comparable to the measured values of $A\Delta R \sim 6$ -8 f Ωm^2 , indicating consistency. For Py/Al, the calculated $A\Delta R \sim 6 \text{ f}\Omega m^2$ is much larger than the measured $A\Delta R \sim 0.5 \text{ f}\Omega m^2$. Similarly to Py/Cu [43], this discrepancy is plausibly due to the inability to reach a full AP state in figure 2.13 (b). In contrast, for Co/Al, the calculated $A\Delta R \sim 1.5 \pm 1 \text{ f}\Omega m^2$ is much smaller than the measured $A\Delta R \sim 7 \text{ f}\Omega m^2$, indicating that our analysis is not internally consistent for Co/Al.

For Co/Al, the AR(AP) data, shown in figure 2.13 (a), and the A Δ R data shown in figure 2.13 (b) for the n=30 multilayer, are similar to those for CoFe/Al and Fe/Al. However, the A Δ R from the EBSV, figures 2.14 (a) and (b), is lower than for the other pairs. As our EBSVs are pinned at ~ 450 K, such a discrepancy might be due to differences in interfacial structure between the unannealed multilayers and the annealed EBSVs. But why Co/Al should differ so strongly in this way from

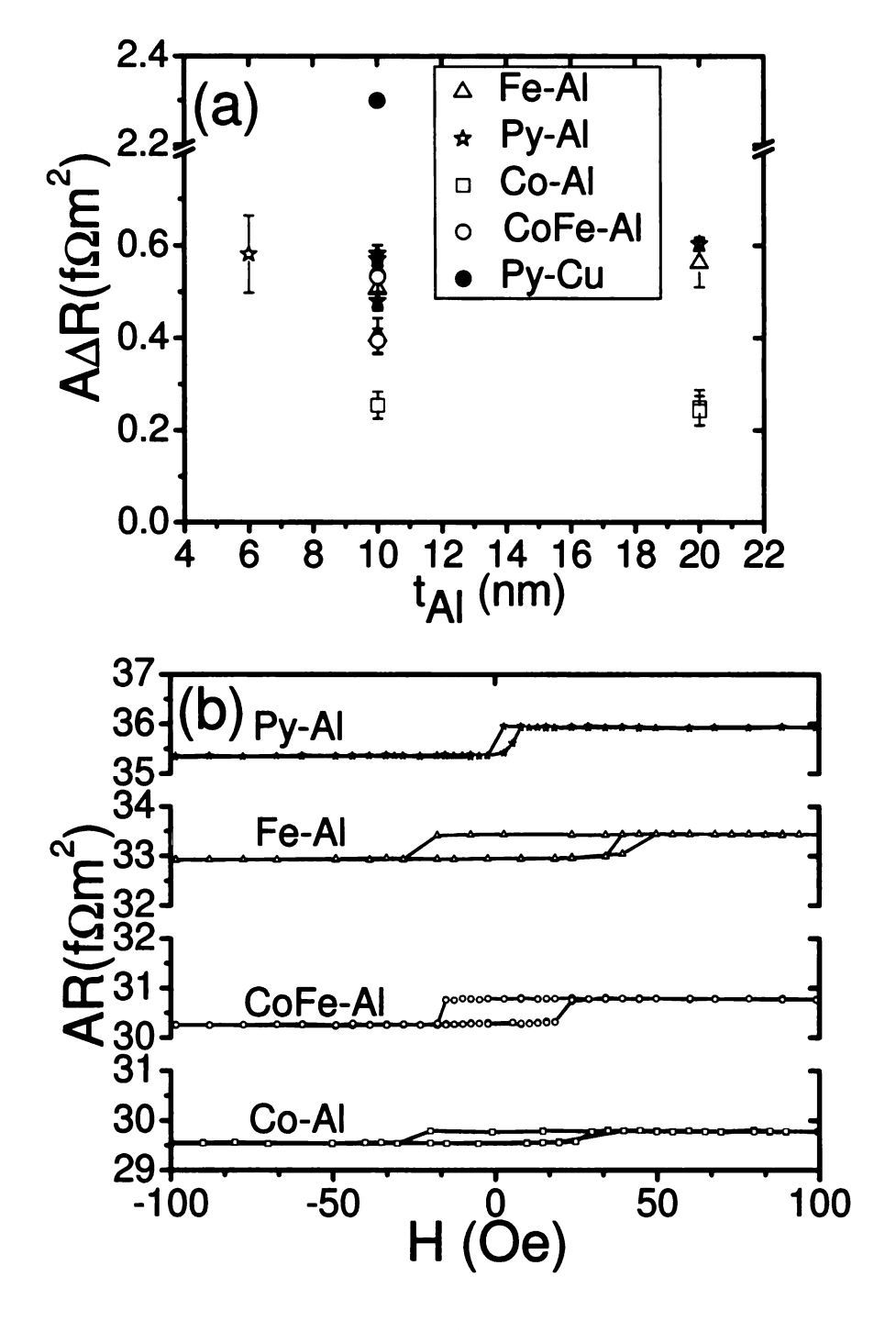


Figure 2.14: (a) A Δ R against t_{Al} for F/t($_{Al}$)/F (F=Py, Co, CoFe (= Co $_{91}$ Fe $_{9}$), Fe) EBSVs. The corresponding datum for a Py/Cu EBSV (filled circle) is shown for comparison. Note the scale break for this datum. (b) AR vs H hysteresis loops for some of the t_{Al} =10 nm EBSVs as shown in (a). The figure is from [94].

the other F/Al pairs studied is not clear. Another reason for this discrepancy could be due to spin-flipping at the Co/Al interface. Including spin-flipping in the VF theory has a much stronger effect on A Δ R for EBSVs than for multilayers. To check this possibility, we did new calculations for Co/Al including spin flipping, and found consistent estimates for both the multilayers and the EBSV data with a spin flip parameter ($\delta_{F/Al}$) = 1.8±0.5. However, if we have such large spin-flipping at the Co/Al interface, it is not clear why we could neglect spin-flipping at the other F/Al interfaces. We list our estimated values of $2AR_{F/Al}^*$, $\gamma_{F/Al}$ and the product $2AR_{F/Al}^*$, $\gamma_{F/Al}$ in table 2.3. For Co/Al, we have listed our estimates without (a) and with (b) spin flipping.

To check if these large values of $2AR_{F/Al}^*$ could be due just to interfacial alloying, we calculated the specific resistance of the interface assuming a 50-50 uniform alloy. For 50-50 % F/Al alloy, we estimate $\rho_{Alloy} \leq 1.5 \times 10^{-6} \Omega m$, using the procedure given in section 2.3.1. With such an alloy resistivity, an $AR^* \sim 5 \Omega m^2$ corresponds to an interface thickness = 3 nm, which is at the upper limit of our estimate of interface width (discussed next). The large $2AR_{F/Al}^*$ is thus likely not due solely to interfacial alloying. Another possible cause of the large $2AR_{F/Al}^*$ might be band structure mismatch.

The diffusion distances listed in Table A.1 for one minute, show small (up to a few percent of an Å) diffusion between F metals in the present study and Al at 295 K, but significant diffusion (up to a few nm) at 450 K. To check for changes in resistance due to interdiffusion, we remeasured some of the F/Al samples after \sim 6-11 months and upon annealing at \sim 450 K. Usually, for multilayers and EBSVs with N metals other

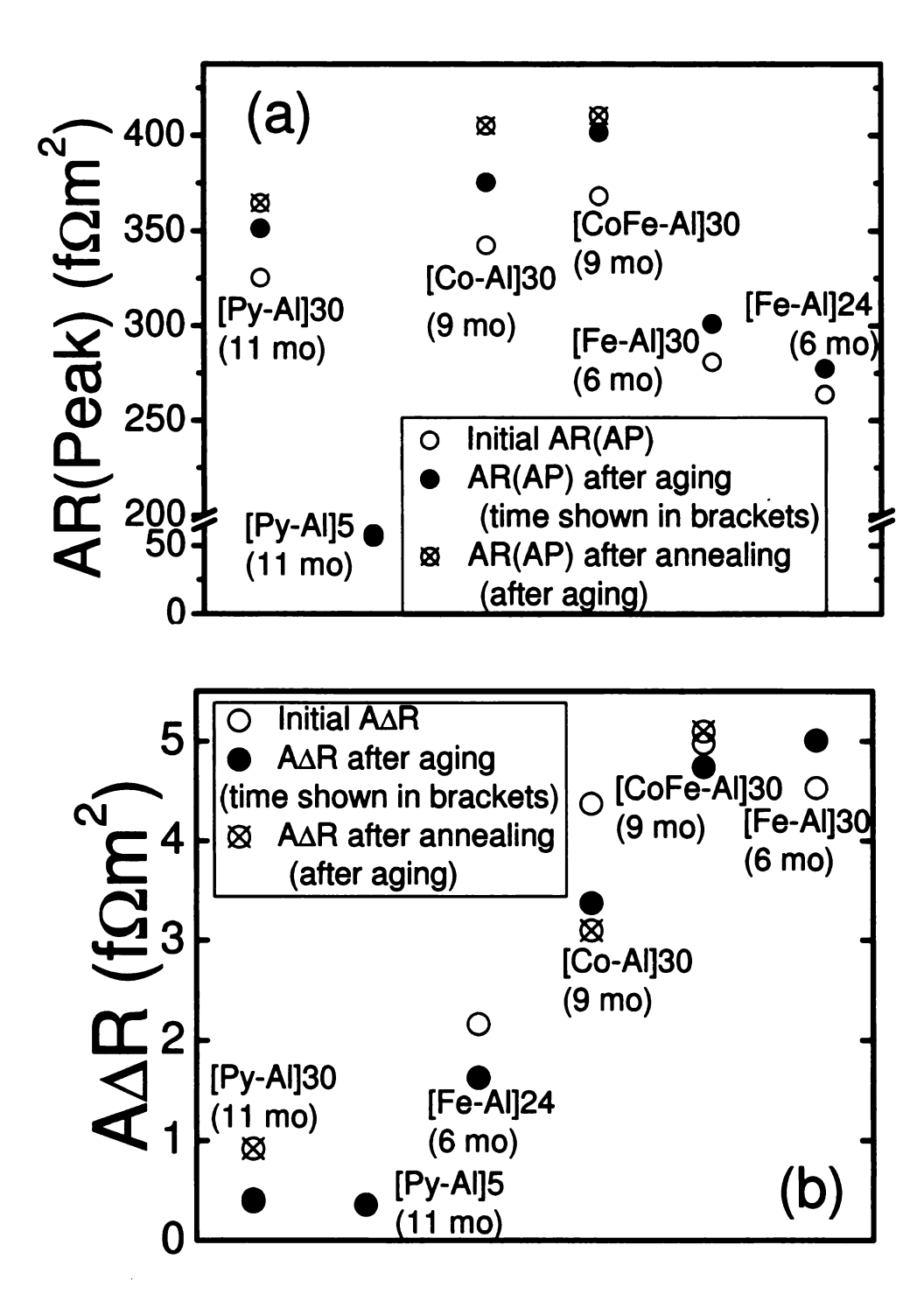


Figure 2.15: The effects of aging and annealing on: (a) AR(Peak), and (b) $A\Delta R$ on remeasured F/Al (F=Py,Co,Co₉₁Fe₉,Fe) multilayers. The number of bilayer repeats for each multilayer is shown after each F/N. The number in the bracket below shows the time after which the sample was remeasured. The figure is from [94].

than Al, the sample resistances vary only about 1% upon aging and/or annealing to ~ 450 K. We show the effects of aging (6-11 months) and annealing (~ 450 K) on selected n=30 and a few other F/Al multilayers in figure 2.15: (a) shows the AR(AP) data, and (b) shows the A Δ R data.

Because the as-grown anti-parallel states in figure 2.13 cannot be reproduced after the samples are subjected to high H, the values of $A\Delta R$ in figure 2.15 (b) are the intermediate maximum values referred to as AR(peak). We see in figure 2.15 (a) that the AR(peak) for our multilayers grows by 5-10 % after aging up to 11 months and increases by a further 2-7% upon annealing to ~ 450 K. The $A\Delta R$ in figure 2.15 (b) fluctuates randomly. The effects of aging on EBSV samples are shown in figure 2.16: (a) shows AR(AP) data, and (b) $A\Delta R$ data. In contrast to the multilayers, for which the resistances change significantly upon aging and annealing, the effects of aging on EBSVs are minimal, presumably because the EBSVs were already heated.

The possibility that the variations in the sample resistances with time and annealing shown in figures 2.15 and 2.16 could be due to interdiffusion motivated us to do advanced structural studies using TEM, HRTEM and EELS on our samples to look for structural changes. As these studies were done by our collaborators at Michigan State University, instead of going into details we just present a brief summary (see [103, 94] for details). Since the structural studies are difficult and time consuming, they were done on only two F/Al metal pairs, Co/Al and Py/Al, assuming that they can represent the complete set. The studies show: (a) There is some misfitting at F and Al interfaces, resulting in incoherent interfaces with nonparallel close-packed planes; (b) There is evidence of intermixing over at least 1 nm but not more than

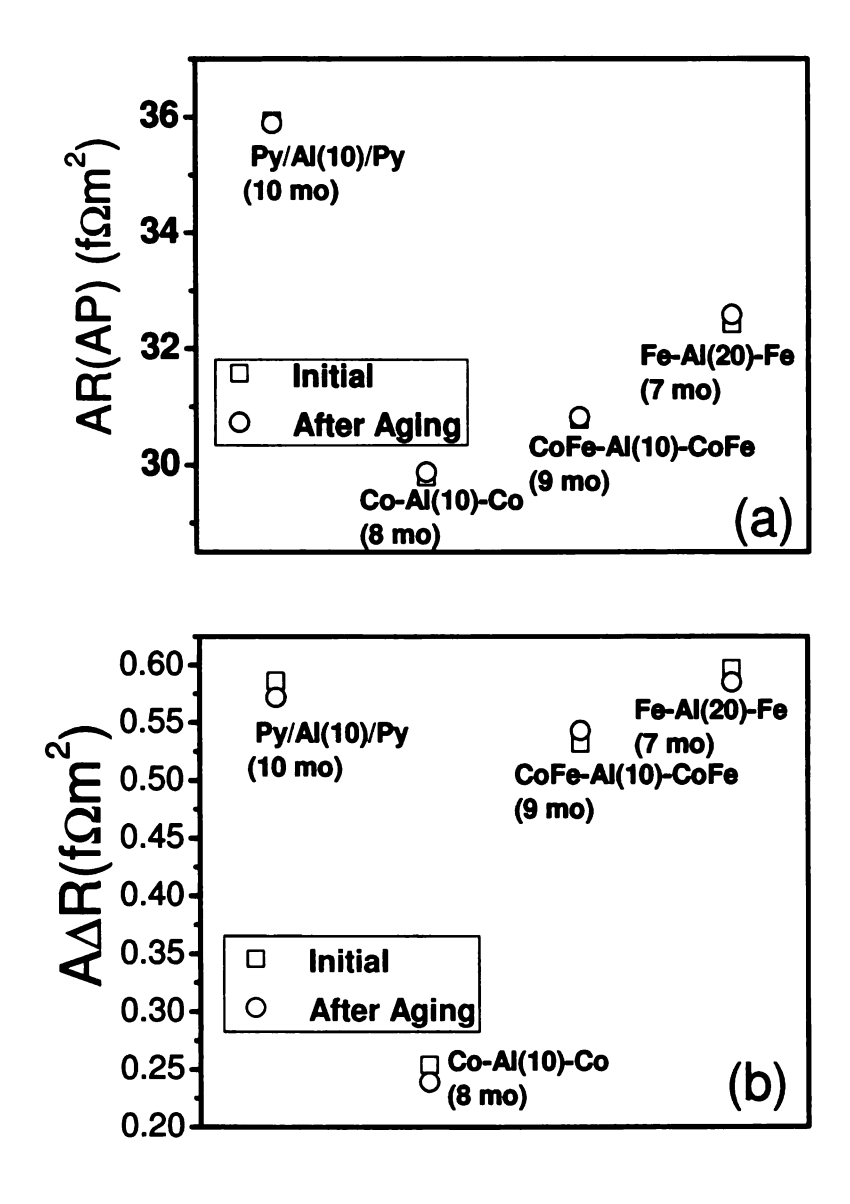


Figure 2.16: The effects of aging on: (a) AR(AP), and (b) $A\Delta R$ on remeasured F/Al/F (F=Py,Co,Co₉₁Fe₉,Fe) EBSVs. The number in the bracket below shows the time after which the sample was remeasured. The figure is from [94].

Metal Pair	$2AR_{F/Al}^*$	$\gamma_{F/Al}$	$2AR_{F/Al}^*\gamma_{F/Al}$
	$(f\Omega m^2)$		$(\mathrm{f}\Omega m^2)$
Py/Al	8.5±1	0.025 ± 0.01	0.21
Co ₉₁ Fe ₉ /Al	10.6±0.6	0.1 ± 0.001	1.06
Co/Al (a)	11.1±0.2	0.05 ± 0.01	0.56
Co/Al (b)	11.6±0.2	0.18 ± 0.02	2.1
Fe/Al	8.4±0.6	0.05 ± 0.02	0.42
Py/Cu	1±0.1	0.7±0.1	0.7

Table 2.3: Our estimates of renormalized interface specific resistance (2AR*), and scattering asymmetry parameter (γ) , for F/Al interfaces. The values for Co/Al (b) were estimated by taking spin flipping (with spin flip parameter $\delta_{F/Al} = 1.8 \pm 0.5$) into account (see text for details). For comparison, we also show values for Py/Cu.

3 nm, but no clear evidence of intermetallic phases; and (c) The thickness of the interface is greater than 1 nm, but less than 3 nm, and the widths do not significantly broaden upon annealing.

2.4.1.4 Conclusions

Motivated by the suggestions from Py/Al nano-pillar studies by the Cornell group that Py/Al interfaces have very different properties than the standard pairs, we determined the interface parameters - - 2AR* and γ for Py/Al. We found a large value of $2AR_{Py/Al}^* \sim 8.5 \text{ f}\Omega m^2$ but small $\gamma \sim 0.025$. We then extended our study to other F/Al interfaces (F = Co, Co₉₁Fe₉ and Fe) in the hopes of finding metal pairs with large values for both the parameters and thus better suited for devices. We again found large values of $2AR_{F/Al}^* = 8.4\text{-}11.6 \text{ f}\Omega m^2$ but small values of $\gamma_{F/Al} \leq 0.18$. Our analysis was internally consistent for all F/Al pairs except Co/Al. For consistency in the Co/Al analysis we included spin flipping at the Co/Al interface. Our diffusion calculations predict significant interdiffusion between F metals and Al. To check the effects of interdiffusion on sample resistance, we remeasured some samples after

significant time and after annealing. We found that the resistance of our multilayer samples changes with aging (\sim 6-11 months) and upon annealing to \sim 450 K. Our EBSV samples, however, did not show any such changes. To look for interdiffusion in our samples we collaborated for detailed TEM, HRTEM, and EELS studies. The structural studies showed some intermixing at the F/Al interfaces (over distances \sim 1 nm) but no evidence of intermetallic phase formation was found. Although all of the F/Al metal pairs have a large 2AR*, due to their small values of γ they do not offer any advantages for devices as compared to standard metal pairs.

2.4.2 Specific resistance and scattering asymmetry parameter of Py/Pd, Fe/V, Fe/Nb, and Co/Pt interfaces

This project was done in collaboration with Dr. N. Theodoropoulou and J. A. Romero. This work has led to one publication, in which I am the first author [104].

2.4.2.1 Introduction

Motivated by the large values of $2AR_{F/Al}^*$, we undertook this project to determine the interface parameters of four new N metals with structurally similar F metals in the hope of finding metal pairs with large values of both $2AR^*$ and γ . We chose four N metals with relatively long spin diffusion lengths [45]. We matched F-metals with the same crystal structure as the N metal to simplify the crystal structure of the multilayer. The metal pairs we studied are Co/Pt (FCC), Py/Pd (FCC), Fe/V (BCC), and Fe/Nb (BCC). Pd and Pt are of special interest because they are polarizable [105, 106]. They may become partly magnetic near the interfaces, and influence the Co/Pt and Py/Pd interface parameters. To look for such effects we will compare our derived Co/Pt and Py/Pd interface parameters with those of Fe/V and Fe/Nb and standard metal pairs.

In the present project, we were most interested to check if the product $2AR^*\gamma$ was large for any of the metal pairs. We thus took sufficient data for detailed analysis for Co/Pt and Py/Pd, but took only minimal data for Fe/Nb and Fe/V for preliminary analysis, to get an estimate of the interface parameters. We find that the interface parameters of the four metal pairs under study do not provide any advantage for devices as compared to those of standard pairs.

2.4.2.2 Experiment

Similar to our F/Al studies, the present study also involves a combination of multilayer and EBSV samples to determine the interface parameters for these four metal pairs - - use multilayers to initially determine $2AR^*$, and EBSVs to determine γ , and then vary the two for internal consistency. However, unlike with F/Al, for the metal pairs in this study, the values of $2AR^*$ were small enough so $A\Delta R$ has a significant effect on the estimate of AR(AP) for multilayers. Because of this problem, we have used a different analysis, in which parallel (P) states (which can be achieved reliably by applying large magnetic fields) are analyzed using the Valet-Fert (VF) formalism to determine $2AR^*$.

Our multilayer samples have the structure Nb(150nm)/ $[F(t_F)/N(t_N)]_n/F(t_F)$ / Nb(150nm) with $t_F = 6$ nm.

For our EBSV samples, we use the structure - - Nb(150)/ Cu(5)/ FeMn(8)/F(t_F) N(t_N)/ F(t_F) / Cu(5)/ Nb(150), where all layer thicknesses are in nm. The thicknesses of the pinned and the free F layers for the four sets of samples are: for Fe/V and Fe/Nb the pinned Fe layer = 12 nm and the free layer = 24 nm; for Py/Pd, both layers = 24 nm; and for Co/Pt, both Co layers = 20 nm. We keep t_N = 6-10 nm for all four sets of samples, large enough to minimize exchange coupling between the F-layers for Nb and V, or to make it weak enough for Pt and Pd such that the exchange bias dominates. Except for Co, which has a long spin diffusion length, $l_{sf}^{Co} \sim$ 60 nm [45], our EBSVs have t_F > l_{sf}^{F} so we can use equation 2.14 to determine γ .

Figure 2.17 (a) shows our multilayer data as a plot of AR(P) vs n. The solid lines

are calculations from joint numerical fits to the average values of AR(P) at n=30 and the EBSV data (shown in figure 2.18). For comparison, we show, as dashed lines, data for Py/Cu [43] and Co₉₁Fe₉/Al [94]. The solid lines fall between those for Py/Cu and Co₉₁Fe₉/Al. In figure 2.17 (b), we show one hysteresis sweep of an n=30 multilayer for each metal pair. As found previously for Py/Cu [43], and we also found in section 2.4.1 for Py/Al, hysteresis sweeps of Py/Pd show very little deviation from AR(P).

For the EBSVs, we measured two independent samples for every case except Fe/V, where only one was measured. The data for several of these pairs overlap to within the sizes of the symbols. Figure 2.18 (a) shows our EBSV data. For Py/Pd, the drop in A Δ R from t $_{Pd}$ = 10 to 20 nm is roughly consistent with $_{sf}^{Pd} \sim 25\frac{10}{-5}$ nm. Figure 2.18 (b) shows the hysteresis curves for t $_{N}$ = 10 nm EBSV samples. All of the curves are closely symmetric about H = 0, consistent with little coupling.

For the EBSV A Δ R data in figure 2.18 (a), A Δ R = 0 for t $_{Pt}$ =5 nm. Initially, we did not expect the interlayer exchange coupling to be strong enough for t $_{Pt}$ =5 nm to overcome the pinning. But we then discovered ref [106], which reported ferromagnetic coupling for t $_{Pt}$ = 5nm. We have omitted these zero values from the fit to the Co/Pt data.

2.4.2.3 Analysis

For our analysis, we combined the average values of AR(P) for n = 30 (figure 2.17 (a)) with the A Δ R data (figure 2.18 (a)) corresponding to $t_V = t_{Nb} = 6$ nm for Fe/V and Fe/Nb, $t_{Pt} = 10$ nm for Co/Pt, and $t_{Pd} = 10$ and 20nm for Py/Pd. We

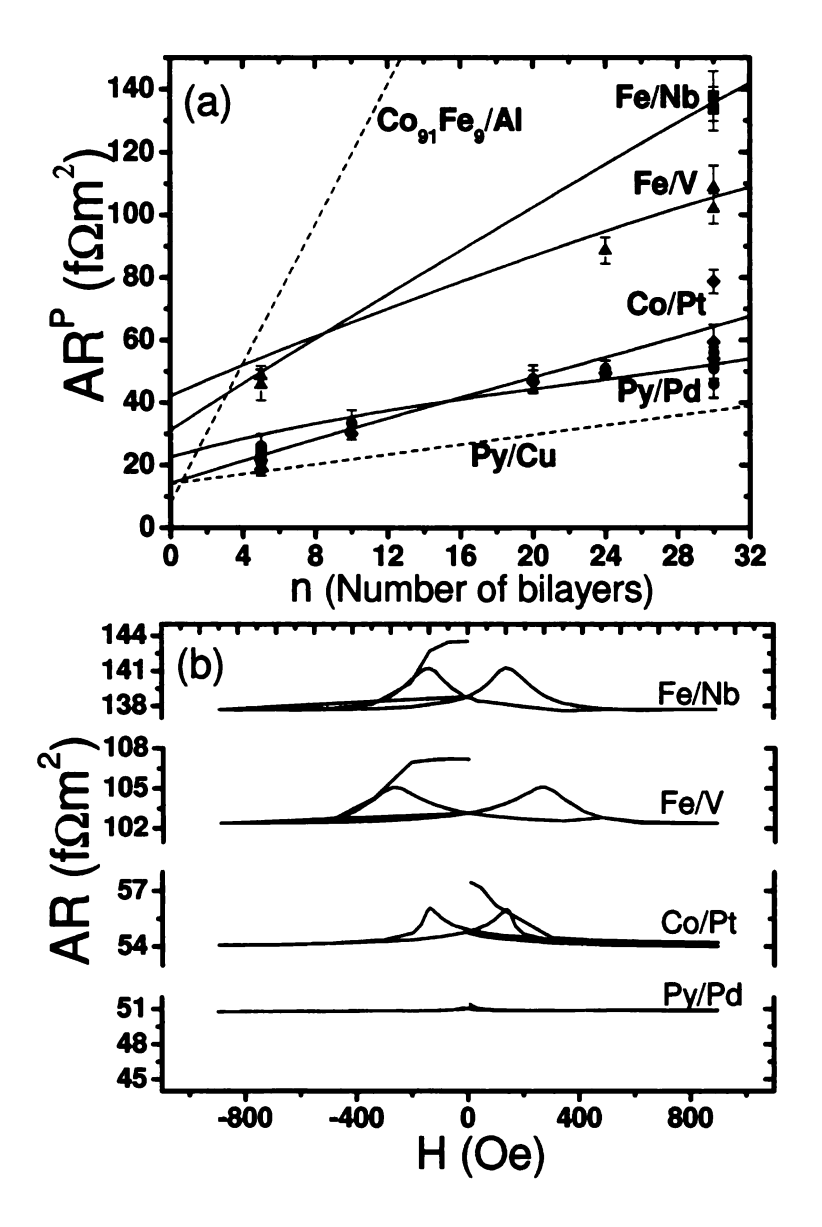


Figure 2.17: (a) AR(P) vs n data for the multilayer samples of the metal pairs under present study -- Co/Pt, Fe/Nb, Fe/V, and Py/Pd. Dashed lines show data for Py/Cu and $Co_{91}Fe_{9}/Al$ for comparison. The solid curves are based on the calculations from fits to the average values of AR(P) at n=30 and the EBSV data. (b) The corresponding hysteresis loops (AR vs. H) for n=30 multilayer samples. The figure is after ref [104].

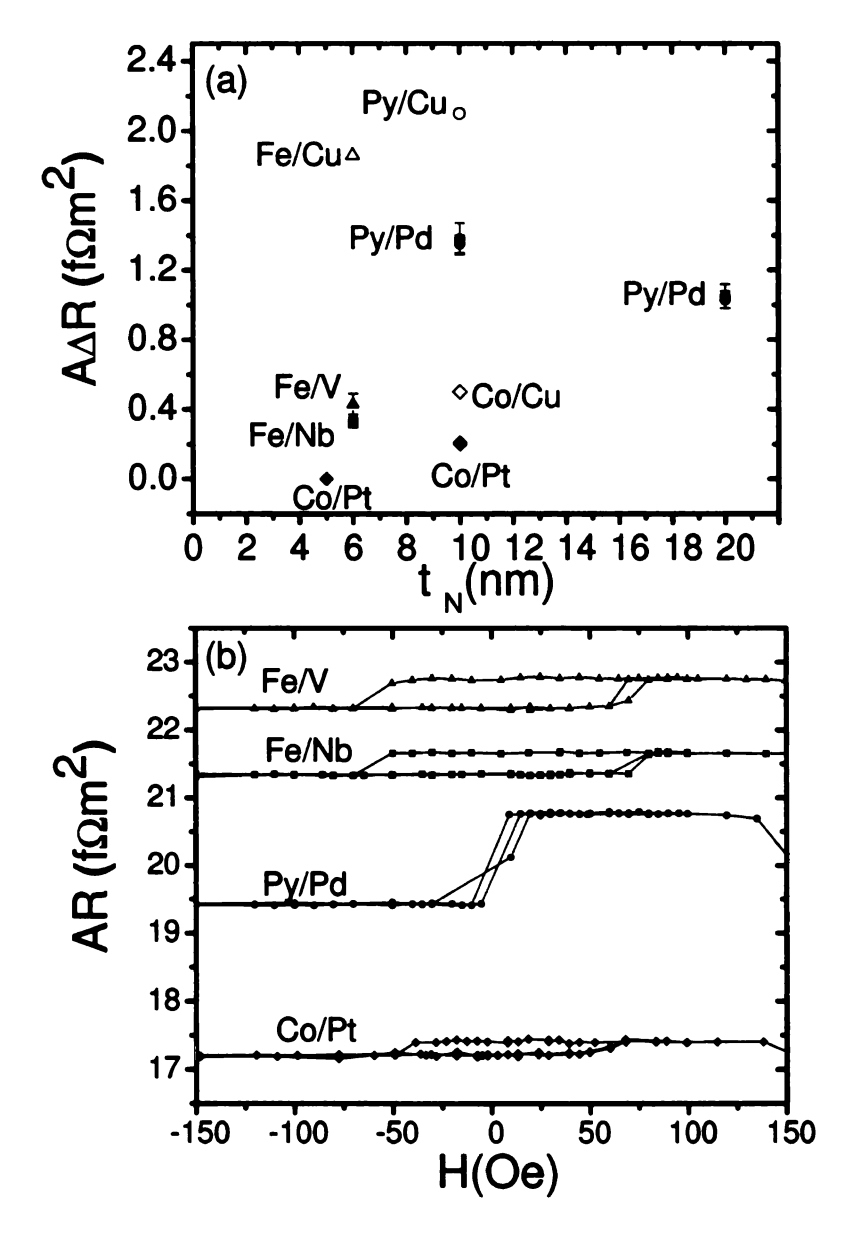


Figure 2.18: (a) $A\Delta R$ vs t_N data for EBSV samples with the trilayer structure -- $Co/t_{Pt}/Co$, $Fe/t_{Nb}/Fe$, $Fe/t_V/Fe$ and $Py/t_{Pd}/Py$. For comparison, we show data for F/Cu (Fe/Cu data from [107], Py/Cu data from [57], and Co/Cu data from [52]). The $A\Delta R=0$ data for $t_{Pt}=5$ nm is hardly visible. (b) The corresponding hysteresis minor loops (AR vs. H) for some of the $t_N=10$ nm EBSV samples. The figure is from ref [104].

then varied both the interface parameters until we got best fits, which we list in table 2.4. To check for internal consistency, we use these same parameters to predict $A\Delta R$ for all four types of multilayer samples with n=30, and compare the predictions to the observed $A\Delta R$ values as shown in figure 2.17 (b).

For Fe/V, the calculated value is similar to the observed value. For Co/Pt and Py/Pd, the calculations give larger values than the observed ones, which is consistent with the inability to reach true AP states. However, for Fe/Nb, calculations using the parameters listed as Fe/Nb (a) in table 2.4 give a smaller value of $A\Delta R$ than the observed one. Such a difference might be due to differences in the Fe/Nb interfaces in the unannealed Fe/Nb multilayers and the annealed Fe/Nb EBSVs. But it could also be due to spin-flipping at the Fe/Nb interface, as the VF theory shows that such spin-flipping reduces $A\Delta R$ more strongly in an EBSV than in a multilayer [93]. We thus added spin flipping at the Fe/Nb interface and did the numerical fits to the VF theory again for the Fe/Nb multilayer (n = 30) and EBSV samples. We got consistent results by including a large spin-flipping parameter $\delta_{Fe/Nb} = 0.83 \pm 0.08$ (similar to that for W/Cu interfaces [46]). The large value of $\delta_{Fe/Nb}$, however, suggests that the physics for Fe/Nb interfaces is much different than that for W/Cu. For the W/Cu interface, the large value of $\delta_{W/Cu}$ is probably due to a strong spin-orbit interaction between the heavy W and light Cu [46]. In contrast, for Fe/Nb, such a large value might be due to unbound paramagnetic moments at the Fe/Nb interface [108, 109].

2.4.2.4 Results

We list our estimates of $AR_{F/N}^*$ and γ in table 2.4. We also list the parameters for Fe/Nb (as case (b)) calculated upon including spin flipping. From the results, shown in table 2.4, we find that

- for Pd and Pt, the two polarizable metals, the parameters are roughly comparable to those for Fe/Nb and Fe/V.
- the estimated values of $2AR_{F/N}^*$ and γ for three of the metal pairs (Co/Pt, Fe/V and Fe/Nb) are intermediate between those of the standard pair, Py/Cu, and recently studied Co₉₁Fe₉/Al. For Py/Pd, $2AR_{F/N}^*$ is smaller than that of Py/Cu.
- We find $\gamma_{Fe/V}$ and $\gamma_{Fe/Nb}$ (case (a)) are negative. A negative value of $\gamma_{Fe/V}$ is consistent with the negative value of β for Fe(V) alloys [2]. As Nb is in the same column of the periodic table as V, a negative value of $\gamma_{Fe/Nb}$ is not unreasonable. However as we have no data for Fe(Nb) alloys, this case is not clearcut.
- For Fe/Nb, internal consistency requires spin flipping at the interface with spin flip parameter - $\delta_{Fe/Nb} = 0.83 \pm 0.08$. But including spin flipping also causes a reversal in the sign of $\gamma_{Fe/Nb}$.

Our studies show that none of the metal pairs studied in the present study give large value of $2AR_{F/N}^*\gamma$ as compared to previously studied metal-pairs.

Metal Pair	$rac{2 ext{AR}_{F/N}^*}{ ext{f}\Omega m^2}$	γ	$rac{\gamma_2 ext{AR}^*_{F/N}}{ ext{f}\Omega m^2}$
	${ m f}\Omega m^2$		${ m f}\Omega m^2$
$Co_{91}Fe_{9}/Al$	10.6 ± 0.6	0.1 ± 0.01	1.06
Co/Pt	1.7 ± 0.25	0.38 ± 0.06	0.65
Py/Pd	0.4±0.2	0.41±0.14	0.2
Fe/V	1.4±0.2	-0.27±0.08	- 0.4
Fe/Nb (a)	2.6±0.3	-0.17±0.04	- 0.4
Fe/Nb (b)	2.9 ± 0.3	0.11±0.04	0.3
Py/Cu	1.0 ± 0.1	0.7±0.1	0.7

Table 2.4: Our estimates of values of $\gamma_{F/N}$, $2AR_{F/N}^*$, and the product $\gamma_{F/N}2AR_{F/N}^*$ for Co/Pt, Py/Pd, Fe/V and Fe/Nb interfaces. For comparison we also list the corresponding parameters for Co₉₁Fe₉/Al and Py/Cu. The difference between the values for Fe/Nb (a) and (b) are explained in the text.

2.4.2.5 Conclusions

Motivated by large values $2AR_{F/Al}^*$ for F/Al (see section 2.4.1), but with small γ , we undertook this project to search for metal pairs with large values of the product $2AR_{F/N}^*\gamma$. We determined the interface parameters for four new metal pairs - - Py/Pd, Fe/V, Fe/Nb and Co/Pt using our standard CPP-MR technique on multilayers and exchange biased spin valves. The four N metals were chosen to have relatively large spin diffusion lengths so that spin-flipping would not affect the CPP-MR. The corresponding F-metals were chosen to match the crystal structure of the N metals to simplify the interfacial structure.

We list our estimates of $2AR_{F/N}^*$, γ and the product $2AR_{F/N}^*\gamma$ in table 2.4. We find that the values of $2AR_{F/N}^*$ and γ for the present metal pairs mostly (except for Py/Pd) fall between the values for Py/Cu and F/Al. We get a negative $\gamma_{Fe/V}$ which is consistent with ref [2]. For Fe/Nb, our analysis for internal consistency includes spin-flipping at the Fe/Nb interface with $\delta_{Fe/Nb}=0.83\pm0.08$. We also

find that the interface parameters for magnetically polarizable N-metals Pd and Pt are not significantly different than Fe/V and Fe/Nb. Unfortunately, the interface parameters of these four F/N metal pairs do not provide any advantages for devices as compared to the standard metal pairs. However, our estimates of $2AR_{F/N}^*$ and γ for new metal pairs provide additional values for theorists working to develop a detailed understanding of interfacial scattering in CPP transport.

2.4.3 Effect of Cu/Al/Cu sandwiches on the magnetoresistance of Py exchange biased spin valves

In this project, I was helped by Dr. N. Theodoropoulou. I expect to be first author in the eventual publication of this project.

2.4.3.1 Introduction

As mentioned in section 1.6, the Cornell group in their Py/ Al/ Py nano pillar studies also observed that bracketing thick Al (\sim 10nm) with thin Cu (\sim 0.6 nm) in Py/Cu/Al/Cu/Al/Py nanopillars gave an MR closer to the small one for Al than for the large one for Cu [82].

We initially thought that such thin Cu would be incorporated into the finite thickness F/Al interfaces, and thus play only a minor role. If so, then, unless the Al/Cu interface specific resistance in unusually large, making the Cu thick should give a MR similar to that for Cu.

To check our interpretation, we undertook a study of the effect of $\mathrm{Cu}(\mathsf{t}_{Cu})/\mathrm{Al}(\mathsf{t}_{Al})$ / $\mathrm{Cu}(\mathsf{t}_{Cu})$ sandwiches on $\mathrm{A}\Delta\mathrm{R}$ (and hence MR) of Py exchange biased spin valves(EBSV). We also undertook to measure $2\mathrm{AR}_{Al/Cu}$, which we discussed in section 2.3.2. We find that the estimated $2\mathrm{AR}_{Al/Cu}\sim 2.2~\mathrm{f}\Omega m^2$ is not large enough to explain the small MR seen by Cornell group.

This section describes the results of our study.

2.4.3.2 Experiment

To study the effect of $\mathrm{Cu}(\mathsf{t}_{Cu})/\mathrm{Al}(\mathsf{t}_{Al})/\mathrm{Cu}(\mathsf{t}_{Cu})$ sandwiches on $\mathrm{A}\Delta\mathrm{R}$, we use EBSV samples with the structure Nb(150) /FeMn(8) /Py(24) /[$\mathrm{Cu}(\mathsf{t}_{Cu})/\mathrm{Al}(\mathsf{t}_{Al})/\mathrm{Cu}(\mathsf{t}_{Cu})]/\mathrm{Al}(\mathsf{t}_{Al})$

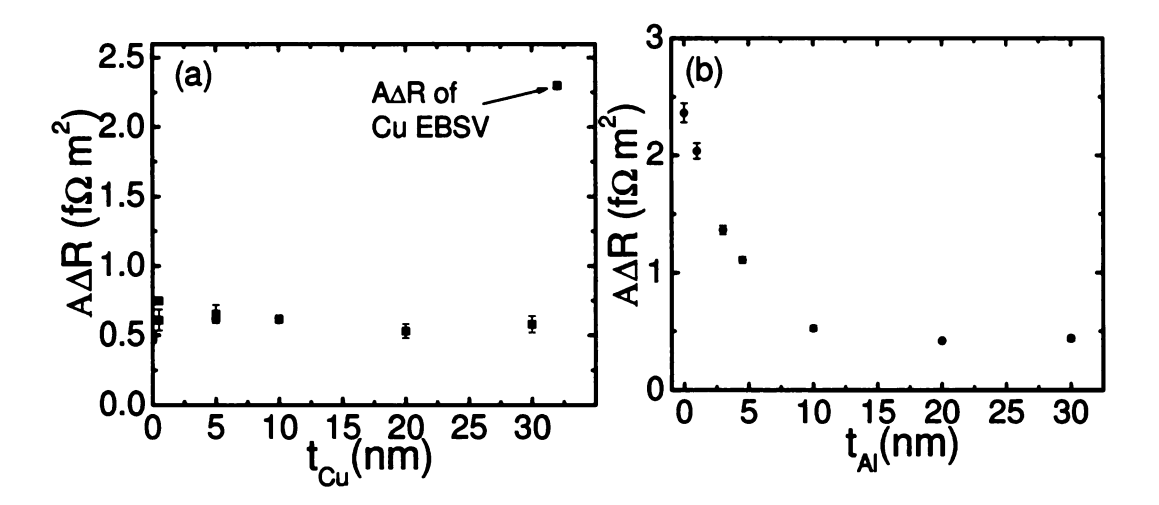


Figure 2.19: (a) Plot of $A\Delta R$ against \mathbf{t}_{Cu} for fixed $\mathbf{t}_{Al}=10$ nm. For comparison, we also show $A\Delta R$ data for a $\mathbf{t}_{Cu}=10$ nm EBSV. (b)Plot of $A\Delta R$ against \mathbf{t}_{Al} for fixed $\mathbf{t}_{Cu}=10$ nm.

Py(24)/Nb(150) (all thicknesses in nm). In each sample, Al is bracketed by two equal thickness Cu layers. We first fix $\mathbf{t}_{Al}=10\mathrm{nm}$ and vary $\mathbf{t}_{Cu}=0$ to 30 nm, and then fix $\mathbf{t}_{Cu}=10\mathrm{nm}$ and vary $\mathbf{t}_{Al}=0$ to 30 nm.

Figure 2.19 (a) shows $A\Delta R$ (for fixed $t_{Al}=10 \mathrm{nm}$) vs. t_{Cu} . For comparison, we also show $A\Delta R$ data for a $t_{Cu}=10 \mathrm{nm}$ EBSV. In contrast to our initial interpretation of the Cornell group's observations, for fixed $t_{Al}=10 \mathrm{nm}$, $A\Delta R$ remains similar to that of an Al EBSV, irrespective of the thickness of Cu. In figure 2.19 (b), we show $A\Delta R$ (for fixed $t_{Cu}=10 \mathrm{nm}$) vs. t_{Al} . Now $A\Delta R$ varies significantly with t_{Al} .

2.4.3.3 Interpretation of the data

The A Δ R for the EBSVs can be calculated using equation 2.14. The parameters in the numerator do not depend on $2AR_{Al/Cu}$. The denominator has contributions from both ρ_{Al} and ρ_{Cu} , and $2AR_{Al/Cu}$. As the resistivities of Al and Cu are small

 $(\sim 5 \text{ n}\Omega\text{m})$, the contribution from the bulk of Al and Cu is small and does not account for the small A Δ R. From our studies given in section 2.3.2 we found $2AR_{Al/Cu}=2.2\pm0.2~\text{f}\Omega m^2$, which is also not large enough to explain the small values of A Δ R. At most it would reduce A Δ R from $\sim 2.3~\text{f}\Omega m^2$ to $\sim 1.5~\text{f}\Omega m^2$.

The possibility of spin flipping at the Al/Cu interfaces causing the variation of $A\Delta R$ for fixed $t_{Cu}=10 \mathrm{nm}$ can be ruled out, as it would be similar for both fixed t_{Al} with variable t_{Cu} and fixed t_{Cu} with variable t_{Al} . Another possibility is formation of alloys or intermetallic compounds, depending on t_{Al} . The diffusion distance of Cu into Al at 450 K (the temperature at which EBSVs are processed) from table A.1 is a few nm for 1 minute suggesting strong interdiffusion between Al and Cu. The interdiffusion between Al and Cu thus might be the cause for the observed unusual EBSV $A\Delta R$. To look for such interdiffusion, we have collaborated at Michigan State University and Arizona State University for structural studies using high resolution transmission electron microscopy and electron energy loss spectroscopy.

The structural studies were done on separate CIP samples with EBSV structure -- Nb(150)/ FeMn(8)/ Py(24)/ [Cu(t_{Cu})/Al(t_{Al})/Cu(t_{Cu})]/ Py(24)/ Nb(150)). These studies were not done by me, so I present only a summary. We focus on the layers of interest 'Cu(t_{Cu})/ Al(t_{Al})/ Cu(t_{Cu})'. For a Cu(10nm)Al(10nm)Cu(10nm) unannealed sample, some intermixing in both the Al-Cu rich regions were found, but the analysis showed formation of Al_XCu_Y intermetallic phases in the Al rich region only. For a Cu(10nm)Al(30nm)Cu(10nm) unannealed sample, well defined Al layers with sharp contrast were observed, hinting much less diffusion by Al and Cu. However, upon annealing, this sample showed strong diffusion of Cu into Al. Prominent diffusion

sion of Al and Cu was also observed for Cu(10nm) Al(3nm) Cu(10nm) and Cu(10nm) Al(1nm) Cu(10nm) samples. All of the studies suggested formation of multiple Al-Cu alloys. For some samples the alloys were not uniform and seemed to be localized to certain grains. We thus infer that Al/Cu form intermetallic phases, but the observed phases vary with the overall stoichiometry of Cu and Al.

2.4.3.4 Conclusions

We have studied the effect of Cu/Al/Cu sandwiches on the A Δ R of EBSVs. We found that for fixed \mathbf{t}_{Al} =10nm, A Δ R is independent of \mathbf{t}_{Cu} . However, fixing \mathbf{t}_{Cu} = 10 nm and increasing \mathbf{t}_{Al} causes a significant drop in A Δ R. Our independently estimated $2AR_{Al/Cu} \sim 2.2~\mathrm{f}\Omega m^2$ is not large enough to explain the small A Δ R. The calculations of diffusion distance of Cu in Al at 450 K show strong diffusion (\sim few nm for 1 minute) between Al and Cu which might be the cause of the observed behavior of the A Δ R. To look for such structural changes, we collaborated for advanced structural studies using TEM, HRTEM and EELS. These structural studies show significant intermixing between Al and Cu causing formation of intermetallic phases, suggesting formation of multiple alloys. The strong interdiffusion between Al and Cu thus probably causes the observed behavior of A Δ R, but a detailed explanation is not yet clear.

Chapter 3

Spin transfer torque studies

This project was carried out jointly with Dr. N. Theodoropoulou. The project has led to two publications [110, 111], in which I am the second author.

In this chapter, we present our spin transfer torque based experiments. To help understand the physics underlying spin transport torque, we have devised a particularly simple test of models, involving a change in only one component of an F/N/F trilayer - - the non-magnetic (N) layer that separates the two ferromagnetic (F) layers. Specifically we have studied the effect on spin transfer torque of just changing the transport in the non-magnetic metal from 'ballistic' to 'diffusive' by comparing results for samples with nominally pure Cu and a dilute CuGe alloy where Ge is a strong scatterer. The transport in Cu is ballistic, in that on average the electrons do not scatter while traversing from one interface to the next - - the mean free path is larger than the layer thickness. In contrast, the transport in CuGe is diffusive, in that the electrons scatter multiple times while traversing from one interface to the next - - the mean free path is smaller than the N layer thickness.

This chapter is organized as follows. In section 3.1 we discuss various models of spin transfer torque. In Section 3.2 we present our 'nano-pillar' sample fabrication

and measurement techniques. In Section 3.3 we discuss our experiments. In section 3.4 we summarize our findings.

3.1 Theory of spin transfer torque (STT)

The first macroscopic model of magnetization dynamics of a magnetization M was given by Landau and Lifshitz in 1935 [112, 113]. They treated the effects from applied field, exchange interaction, and anisotropy, by an effective field $H_{\rm eff}$, which along with damping was taken into account phenomenologically. Gilbert in 1955, proposed that the phenomenological dissipation can be treated by introducing a kind of 'viscous' force. Both Landau-Lifshitz and the Landau-Lifshitz-Gilbert (LLG) formalism have been shown to be mathematically equivalent. We use the LLG equation which is given as

$$\frac{\partial \mathbf{M}}{\partial t} = -\gamma \mathbf{M} \times \mathbf{H}_{\mathbf{eff}} + \alpha \mathbf{M} \times \frac{\partial \mathbf{M}}{\partial t}$$
 (3.1)

where α is an assumed damping coefficient.

The effect of spin transfer torque on the magnetization dynamics can be taken into account as an additional contribution to the LLG equation 3.1 and is given as

$$\frac{\partial \mathbf{M}}{\partial t} = -\gamma \mathbf{M} \times \mathbf{H}_{\mathbf{eff}} + \alpha \mathbf{M} \times \frac{\partial \mathbf{M}}{\partial t} + \mathbf{STT}$$
 (3.2)

which we write here simply as STT and define in detail later.

Since the initial predictions in 1996, there have been various models of spin transfer torque. We will briefly review the models. A more detailed discussion on spin transfer torque can be found in refs. [114, 115, 116].

The initial theories of spin transfer torque in an F/N/F trilayer structure were

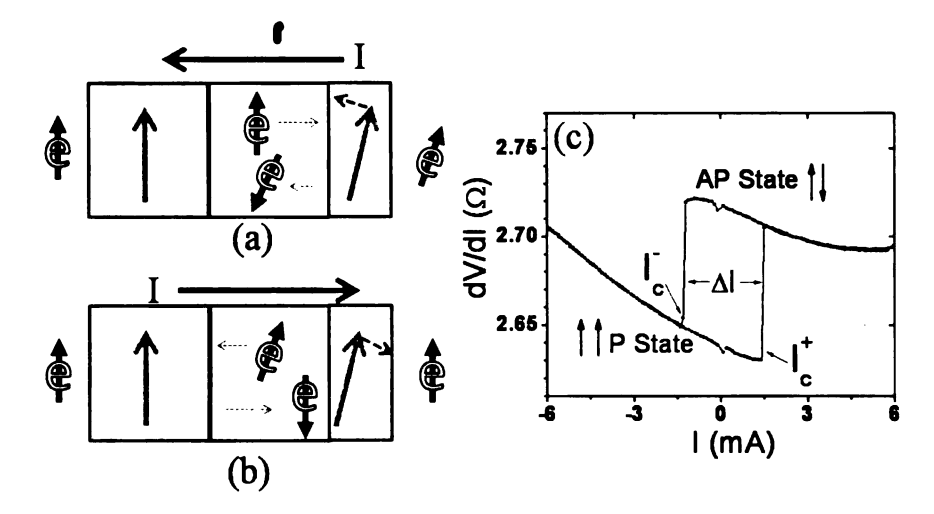


Figure 3.1: A cartoon to show the spin transfer torque in a F/N/F trilayer. The left F layer is a thicker layer than the right thin F layer. (a) The case when electrons propagate from the thicker F layer toward the thinner F layer (b) The case when electrons propagate from the thin F layer to the thick F layer. In (c) we show a typical differential resistance (dV/dI) vs. I plot of spin transfer torque induced switching. We show the higher resistance AP state, lower resistance P state, and the critical switching currents I_C^+ and I_C^- at which the magnetic configuration changes from P to AP and vice versa.

given independently by Slonczewski [8] assuming ballistic transport, and Berger [9] assuming diffusive transport. Berger later showed that the two initial models were generally equivalent [117, 118]. In the Berger model, a dc current passing through a non-magnetic metal (N)/ ferromagnetic metal (F) interface causes 'spontaneous' emission of spin waves, which leads to magnetization dynamics of the F layer. The formalism of Berger's model is very complicated so we will not discuss it further.

The Slonczewski ballistic model [8] is widely used to qualitatively explain the physics underlying spin transfer torque. In this model, a polarized current upon passing through a magnetic layer, with orientation of the magnetization non-collinear to that of the moment of the polarized electrons, exerts a torque on the magnetic layer.

The physics of this model is that the transverse component of the total spin angular momentum of the polarized electrons, traversing the N/F interface, is absorbed by the magnetic layer. The electrons passing through the magnetic layer only retain the component of the total spin angular momentum which is parallel to the moment of the magnetic layer. The absorbed transverse component of the total spin angular momentum, according to Newton's third law, then exerts a torque on the magnetic layer, called spin transfer torque. There is no spin torque for a magnetic layer with orientation of the magnetization perfectly collinear to that of the moment of the polarized electrons, as there is no transverse component of the total spin angular momentum.

The spin torque studies use a $F(t_{fixed})/N/F(f_{free})$ trilayer structure where the fixed layer is made thick and the free layer is made thin. The fixed F layer acts as a polarizer. The polarized electrons exert spin torque on the free F layer and cause switching to parallel or anti-parallel orientation of the two F layers which is then measured as GMR.

The spin transfer torque acts on both the F layers. But the moment of the thick F layer is hard to re-orient. So electrons impinging on it from the free layer are reflected back, which again leads to the re-orientation of the moment of the free layer.

Figure 3.1 (a) shows a cartoon of electrons getting polarized upon passing through the thick polarizing F-layer. The polarized electrons propagate through N and exert a spin-torque on the thin switching F-layer. Figure 3.1 (b) shows the case of electrons propagating from the thin F layer to the thick F layer. The polarized electrons exert a torque on the thick F layer. The thick F layer is very hard to reorient and in

turn reorients the polarized electrons which then apply a spin torque on the thin F layer. Figure 3.1 (c) shows the change in the resistance with current due to the GMR effects. The higher resistance state is the AP state and the lower resistance state is the P state. In the plot we show the critical currents, I_C^+ , I_C^- , at which the magnetic configuration changes from P to AP and vice versa, and the difference $\Delta I = I_C^+ - I_C^-$.

In the ballistic Slonczewski model, the spin transfer torque depends only on the polarization by the 'thick' polarizing layer. The polarizing factor P is defined in terms of n_{\pm} - - the majority/minority state Fermi level spin densities in the magnets, and is given by

$$P = \frac{n_{+} - n_{-}}{n_{+} + n_{-}} \tag{3.3}$$

The spin torque is given by (equation 13 of ref. [8])

$$\dot{\mathbf{S}}_{2} = \left(\frac{J_{eg}}{e}\right)\hat{\mathbf{s}}_{2} \times (\hat{\mathbf{s}}_{1} \times \hat{\mathbf{s}}_{2}) \tag{3.4}$$

where the scalar function q is given by

$$g = \left[-4 + \frac{(1+P)^3 (3+\hat{\mathbf{s}_1}.\hat{\mathbf{s}_2})}{4P^{3/2}} \right]^{-1}$$
 (3.5)

The $\hat{\mathbf{s}}_{1,2}$ are the unit vectors along the magnetizations of the two ferromagnets respectively and J_e is the current density.

Using free-electron models, and first-principles electronic structure calculations for real material interfaces, Stiles and Zangwill in 2002 [119] demonstrated explicitly that the transverse component of a spin current that flows from a non-magnet into a ferromagnet is absorbed at the interface and causes spin-transfer torques.

Another model of spin transfer torque was proposed by Heide and co-workers [74, 73, 75]. The Heide model is based on nonequilibrium exchange interaction (NEXI)

between the ferromagnetic layers. In this model, the longitudinal spin accumulation in both the free and fixed layer acts as a current dependent effective field and causes switching. The Heide model predicted that the effective critical current density (ΔJ_C) is proportional to the ratio of thicknesses of the free and the fixed layers $(\mathbf{t}_{Free}/\mathbf{t}_{Fixed})$. The experimental observations of Albert et al [120] showed that ΔJ_C is proportional to \mathbf{t}_{Free} but not to $1/\mathbf{t}_{Fixed}$. The calculations by Berger [121] show that NEXI torques are significant only if the free layer is very thin (\sim few monolayers). The spin torque samples usually have $t_{free} \sim$ few nm and thus the contributions from NEXI torques are expected to be small.

An alternate model for spin transfer torque induced switching, including exchange interaction between local moments and spin accumulation of conduction electrons, was proposed by Zhang et al [122]. In this model, the transverse spin accumulation at the surface of the free layer (with a characteristic decay length $\lambda_J \sim 2$ nm) acts both as spin torque and an effective field. They predicted that for $\mathbf{t}_{Free} \gg \lambda_J, \, \Delta J_C \propto \mathbf{t}_{Free}$ and for $\mathbf{t}_{Free} < \lambda_J, \, \Delta J_C \approx \mathrm{constant}.$ In contradiction to the predictions, the experimental observations of Albert et al [120] show that ΔJ_C remains proportional to \mathbf{t}_{Free} even down to $\mathbf{t}_{Free} \sim 1$ nm. Shpiro et al [123] use this same approach to calculate spin torque due to the bulk of the layers and diffusive scattering at interfaces. They argue that the spin torque is probably due to contributions from both bulk and interfaces.

A 'thermal activation' model of the spin torque induced switching was proposed independently by Wegrowe et al, Myers et al, and Urazhdin et al. [124, 125, 126, 127, 128]. It was subsequently argued whether the thermal activation is governed

by sample temperature or a higher effective magnetic temperature T_m . A good discussion of these models can be found in ref. [129]. In later experimental studies, Krivorotov et al. [130] argued from measuring the switching rates that the switching was governed by the temperature of the sample and not the higher effective T_m .

Brataas et al [131] used a finite-Element based circuit theory approach to model spin dependent transport. Slonczewski in 2002 took the circuit theory approach and extended his initial ballistic model to include diffusive transport in the ferromagnetic layers [132]. The transport in the non-magnetic metal was still treated as ballistic. This Slonczewski theory is for a symmetric trilayer structure. The theory is based on a density matrix description of the spacer layer and a circuit theory description of the rest of the structure. Slonczewski showed that the predictions of his diffusive model were in general agreement with his earlier ballistic model.

The Slonczewski diffusive model for the symmetric case was extended to the asymmetric case by Xiao and coworkers [133]. Xiao et al [134, 133] calculated spin transfer torques using numerical solutions to the Boltzmann equation. They found that the spin torques calculated using the Boltzmann equation agreed well with the Slonczewski diffusive model. The critical current in this model is inversely proportional to the slope of the torque curve

$$\Delta I \propto \left| \frac{d\tau(P)}{d\theta} \right|^{-1} + \left| \frac{d\tau(AP)}{d\theta} \right|^{-1}$$
 (3.6)

Another model for spin transfer torque, under a small angle approximation was developed by Fert and co-workers [135, 136]. This Fert model is based on the classical spin diffusion equations used in CPP-MR theory. These spin diffusion equations are

used with relevant boundary conditions for the longitudinal and transverse components of the spin current with quasi-interfacial absorption of the transverse components. The advantage of this model is that the spin transfer torque can be expressed in terms of the usual CPP-MR parameters and two additional parameters, and is given as

$$\tau = -\hbar \left[\left(\frac{v_F m_N^{P(AP)}}{8} + \frac{j_{m,N}^{P(AP)}}{2} \right) (1 - e^{-d_{\odot}/\lambda}) \right] (\hat{\mathbf{s}} \times (\hat{\mathbf{s}} \times \hat{\mathbf{S}})$$

$$-\hbar \left[\left(\frac{v_F m_{F1}^{P(AP)}}{4} + j_{m,F1}^{P(AP)} \right) e^{-d_{\odot}/\lambda} \right] (\hat{\mathbf{s}} \times (\hat{\mathbf{s}} \times \hat{\mathbf{S}})$$
(3.7)

where $m_N^{P(AP)}$ $(j_{m,N}^{P(AP)})$ is the spin accumulation density (spin current) in the N layer at the N/F2 interface in the P and AP configuration, $m_{F1}^{P(AP)}$ $(j_{m,F1}^{P(AP)})$ are the same quantities in F1 at the F1/N interface and λ is the mean free path in N.

Recently, the spin transfer torque has been calculated from first principles using a non equilibrium Green's function (NEGF) and density functional theory (DFT) approach [137, 15]. The NEGF + DFT based calculations of spin transfer torque for Co/Cu/Co spin valves were found to be in agreement with the calculations from other spin transfer torque models [137].

3.2 Nano-pillar sample fabrication and measurement

As noted in section 1.4, the samples for spin transfer torque studies require ultra small cross sections \sim few 100 nm in diameter: (a) to achieve the required large current densities $\sim 10^8$ A/cm² needed to observe STT effects, and (b) for the STT

effects to dominate over self Oersted field effects due to the propagating current. To achieve these ultra small cross sections we begin with multilayer samples with the structure Cu(80)/F(24)/N(10)/F(6)/Cu(2.5)/Au(10), where all layer thicknesses are in nm. We then pattern the top Au, the free F layer and part of the middle N layer into $\approx 70 \times 130 \text{ nm}^2$ nanopillars. The remainder of the middle N layer and the fixed F layer are left unpatterned to minimize magnetic coupling between the two F layers. The middle N layer is kept sufficiently thick $\sim 10 \text{ nm}$ to minimize any exchange coupling between the two F layers (see section 1.2.3)

3.2.1 Nano-pillar fabrication process

The nano-pillar fabrication process that we follow has been discussed briefly in ref. [127] and in detail in ref. [88]. We have added a few steps to the process. We review our nano-pillar fabrication and measurement process here. The complete nano-pillar process is shown schematically in figure 3.2.

The fabrication of nano-pillar samples to study spin transfer torque driven switching requires a complex multi-step process involving optical lithography, evaporation, e-beam lithography (EBL), sputtering, and ion-milling. During the fabrication process, the samples are inspected using optical microscopy, electron microscopy, and atomic force microscopy. Details of the processes for optical lithography and e-beam lithography are listed in appendix A.4 and A.5 respectively.

Step 1: Generate window and deposit bottom Au leads.

Optical lithography: We do optical lithography on a 3" Si(100) wafer to generate the windows for the Au 'leads' used to make contacts to the nano-pillars.

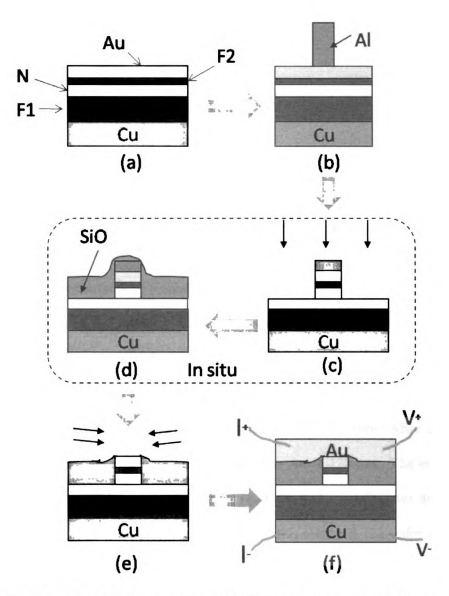


Figure 3.2: A cartoon showing our nano-pillar fabrication process. (a) The sputtered multilayer. (b) The Al pillar $\sim 70 \times 130 \text{ mm}^2$, as a ion-mill mask, is evaporated onto the sputtered multilayer. (c) The sample is ion-milled approximately until the middle of the N layer. (d) SiO is evaporated 'in-situ' onto the ion-milled substrate. (e) The sample is ion-milled from sides. (f) The top Au pads are evaporated and the nano-pillar is ready to measure. In (f) we also show schematically the leads connected to measure the nano-pillar resistance.

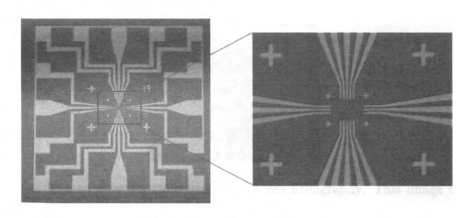


Figure 3.3: Optical microscope image of a 1/2" chip with leads. The right picture is a blow up of the central region.

Our photo-mask is such that we get 21 identical 1/2" substrates. Each 1/2" substrate has leads to make contacts to 5 nano-pillars.

Evaporation of Au leads: The evaporator chamber is prepared for evaporating Ti and Au. We deposit a little Ti (~ 10 Å) before the Au for better adhesion. The processed 3" wafer is loaded into the evaporator. The chamber is then closed and pumped for few hours to achieve a vacuum $\sim 2 \times 10^{-7}$ torr. After achieving a good vacuum, we evaporate Ti ~ 10 Å and then Au ~ 120 nm. The evaporator is then allowed to cool for ~ 45 mins, after which the wafer is taken out and put in acetone for few hours for lift-off. After a good lift-off is observed, the wafer is cleaned with IPA, blow dried and inspected with an optical microscope.

The 3" wafer is diced into 1/2" substrates using a diamond wafer dicing machine.

Each 1/2" substrate is then individually processed. Figure 3.3 shows one of the 1/2" substrate with Au leads. The substrate has leads to connect to five pillars. The image on the right is a blow up of the central region.

Step 2: Shape sputtering window and deposit Multilayers.



Figure 3.4: The window for sputtering by e-beam lithography. This image is taken by an optical microscope.

E-beam Lithography: E-beam lithography is used to prepare the window to sputter into. Figure 3.4 shows an optical image of the sputtering window.

Sputtering: The substrates are loaded into the sputtering chamber and sputtered similarly to the samples mentioned in chapter 2. Up to sixteen 1/2" substrates can be sputtered in one sputtering run. The sputtered substrates are kept in acetone for few hours for lift-off. After a good lift-off is observed, the substrate is cleaned with Isopropyl Alcohol (IPA), blow dried and inspected with an optical microscope.

Step 3: Prepare mask holes and evaporate Al

E-Beam lithography: The e-beam lithography to make nano-pillar sized 'holes' to deposit Al, which acts as a ion-mill mask, is done on the sputtered substrates. Figure 3.5 (a) shows an optical image of the nano-pillar holes after e-beam lithography.

Evaporation: The substrates with the nano-pillar sized 'holes' are loaded into the evaporator chamber. After a good vacuum is achieved, ~ 60 nm of Al is evaporated, which fills the holes. We deposit Al as it has a low ion-milling rate and thus acts as a good ion-milling mask. The processed substrate is then taken out

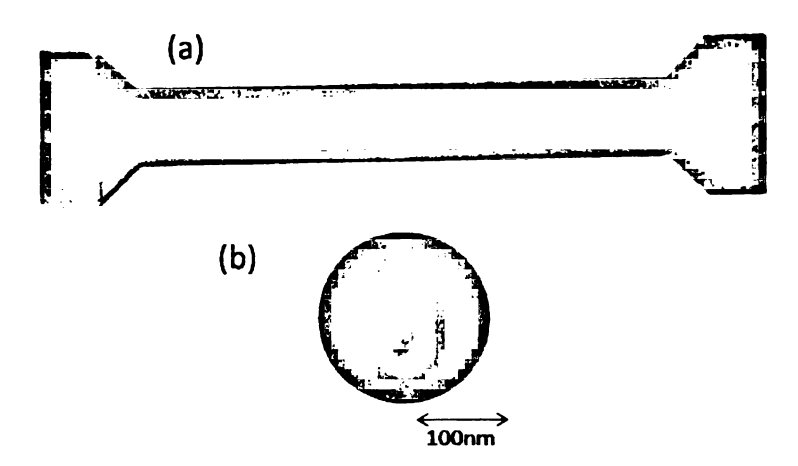


Figure 3.5: The top figure is the optical image of nano-pillar holes after e-beam lithography. The bottom inset is an image of one of the Al nano-pillars taken by electron microscope.

(after ~ 45 mins) and put in acetone for few hours for lift-off. After a good lift-off is observed, the wafer is cleaned with IPA, blow dried and inspected initially with an optical microscope to check for cleanliness. Of five substrates prepared at a time, one or two are selected for examination with an electron microscope. From one to five Al nanopillars on each substrate are inspected with the electron microscope to check for size and shape. We examine only a few 'representative' Al nano-pillars since the electron beam affects the nano-pillars. Figure 3.5 (b) shows an image of one of the Al nano-pillars taken by electron microscope. As Al has very low mass, it does not image well.

Step 4: Prepare ion-milling window and ion mill from top

E-beam lithography: E-beam lithography for the ion-milling window is then done on the substrates with the Al nanopillars.

Calibrating time to ion mill: Our nano-pillar sample geometry requires precision ion-milling to stop in the middle of the N layer. For this precision ion-milling,

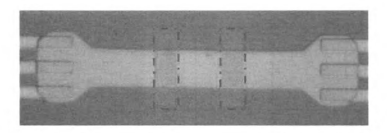


Figure 3.6: Optical image of the substrate with the sputtered multilayer. The dashed lines schematically show the windows generated by e-beam lithography on a real multilayer for ion-mill calibration.

we calibrate the time to ion mill. For such calibration, we do e-beam lithography on separate sputtered 1/2" substrates with identical multilayer structure, except but not processed for the Al nano-pillar step. An example of an ion-mill calibration sample is shown in figure 3.6. The dashed lines schematically show the windows generated for ion-mill calibration.

The 'calibration' samples and the real ones are mounted on the sample holders and loaded into the ion-mill chamber through a load lock mechanism. The ion-mill chamber can accommodate up to five 1/2" substrates. The chamber is pumped for a few hours until a good vacuum ($\sim 9 \times 10^{-8}$ torr) is achieved. Ar is slowly introduced into the chamber and the rate is stabilized to maintain the chamber pressure $\sim 1.2 \times 10^{-4}$ torr. The ion-mill is turned on and run for ~ 20 mins for stabilization. To calibrate the ion-mill time, the 'calibration' samples are ion-milled for a set time with set ion-mill parameters. The ion-mill is turned off. The calibration samples are taken out of the chamber, and cleaned with acetone and IPA and blow dried. The depth of the ion-milled region in the calibration samples is measured using an atomic force microscope (see figure 3.7). If the measured depths match with the intended ion-mill depth, then the corresponding time and ion-mill parameters are used to ion mill the

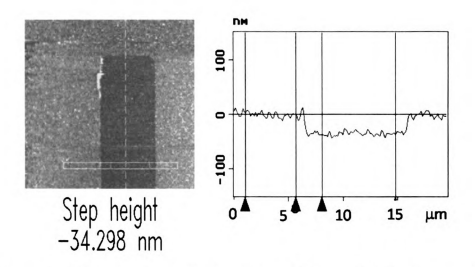


Figure 3.7: The atomic force microscope scan of a ion-mill calibration sample.

real samples. If the measured depths disagree significantly with the intended ionmill depths, then we repeat the process of calibration till a set of standard time and
ion-mill parameters agree with each other.

Ion Milling: After calibrating the ion mill time, the ion-milling is done on all the 'real' samples, the ion-mill is turned off but the samples are left in the chamber for additional processing as described next.

Step 5: In-situ deposition of SiO

Evaporate SiO: We now cover the the ion-milled samples with an insulating layer of SiO. The SiO evaporation system is a part of the ion-mill chamber so that the ion-milled samples can be covered with SiO without breaking the vacuum. The SiO evaporator is turned on and the rate is measured with a Sycon film thickness monitor. The ion-milled samples are then covered with ~ 24 nm of SiO. The SiO evaporator is turned off and the SiO evaporated samples are taken out of the ion-mill chamber (after ~ 40 mins), and put in acetone (sometimes, boiling acetone is used

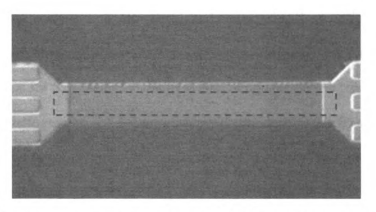


Figure 3.8: Optical image of the substrate after SiO liftoff. The dashed lines schematically show the window generated by e-beam lithography for ion-mill by sides.

instead to achieve faster liftoff) for few hours. After a good lift-off is observed, the samples are cleaned with IPA, blow dried and inspected with the optical microscope.

Step 6: Prepare window for ion-milling from the sides and ion mill

To break the insulating layer of SiO to connect the upper leads to the multilayer region, we ion mill the samples by sides.

E-beam lithography: The e-beam lithography for 'ion-milling from sides' window is done on the SiO evaporated samples. This 'ion-milling from sides' window is such that it protects the edges of the sputtered multilayer region during ion-milling. The dashed line in figure 3.8 schematically shows the rectangular window generated by e-beam lithography for ion-mill by sides.

Ion milling by sides: The samples with the 'ion-milling from sides' window are mounted on special holders such that the plane of the sample is $\sim 3^{\circ}$ with the vertical. Each sample is ion-milled from the first side for ~ 2 mins. The samples are taken out, rotated by 180° (in the plane of the sample) and loaded again to ion-mill from the other side. The ion-milled samples are taken out of the ion-mill chamber

and cleaned with acetone, IPA, blow dried, and inspected with an optical microscope.

Step 7: Generate window for top leads and deposit top Au leads

The samples are now ready for the final step of putting on the top Au leads.

E-beam lithography: E-beam lithography is done to generate windows for the top leads.

Cleaning surface by ion milling and evaporation of Au: The samples with the 'top leads' window are mounted on the sample holders and loaded into the ion-mill chamber. In addition to the ion-mill and the SiO evaporator, this chamber also has a small Au sputtering gun. The samples are first ion-milled for ~ 5 secs to clean the top Au surface of each nano-pillar, and then 100 nm of Au is sputtered onto each sample. The samples are taken out of the chamber and put in acetone for a few hours for lift off. After a good lift off is observed, the samples are cleaned with IPA and blow dried and inspected with an optical microscope. The samples are now ready to be measured. Figure 3.9 shows an optical image of the sample with the top Au leads. Figure 3.10 shows a schematic drawing of a finished nano-pillar. The finished nano-pillar has a patterned nano-pillar structure for the thin F layer and approximately half of the middle N layer. The rest of the structure is extended.

3.2.2 Nano-pillar Measurement

The resistance of the nano-pillar is measured using a lock-in based dV/dI setup. The samples are mounted on a quick-dipper stick - - a stick with connecting wires and with an option to attach a superconducting magnet for 4.2 K measurements. The current and voltage leads are connected to the extended leads using Indium (see figures 3.9

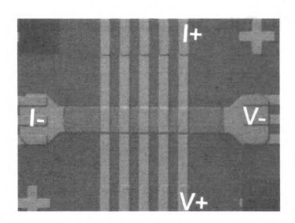


Figure 3.9: The optical image of the sample with top Au leads. The current and voltage leads to measure the resistance are marked as I⁺, I⁻, V⁺ and I⁻.

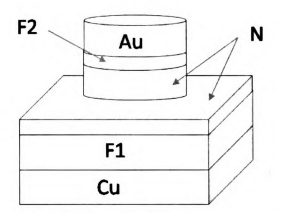


Figure 3.10: A cartoon of the finished nano-pillar.

and 3.3). For protection against static charge, all the leads are initially shorted on the substrate (see outer edges on figure 3.3 left). The leads of the pillar we want to measure are scratched, to isolate that nano-pillar from the shorting structure on the substrate. To put the DC bias current through the sample, we use a battery operated current source. The quick dipper is inserted into an electromagnet and the sample is measured at 295 K with both field and current sweeps. Measurements at 4.2 k are done by attaching a superconducting magnet to the quick dipper stick and then inserting the stick in a liquid He dewar.

3.3 Experiment: ballistic vs. diffusive transport in the N layer

We wish to determine the following two experimental ratios, for comparison with various theories.

- The first ratio is $\Delta I(Diffusive)/\Delta I(Ballistic) = \Delta I(CuGe)/\Delta I(Cu)$ where $\Delta I = I_c^+ I_c^-$ is the difference between the positive and negative switching currents I_c^+ and I_c^- (shown in figure 3.1)
- \bullet The second ratio is I_c^+/I_c^- for each Cu and CuGe.

We have chosen to compare ratios in the hope that most, if not all, of any systematic errors will cancel.

3.3.1 Selection of N metals

For the two N metals in this study, we needed metals (or alloys) with spin diffusion lengths several times greater than the N layer thickness, but one with mean free path less, and the other with mean free path greater, than the N layer thickness. To meet these criteria we chose nominally 'pure' Cu and a dilute Cu(5 at.% Ge) alloy. We chose Cu because it has both a long mean free path (low resistivity) and a long spin diffusion length at both 295 and 4.2 K (see table 3.1).

We chose a Cu(5 at % Ge) alloy (hereafter referred as CuGe) because Ge in Cu

1. greatly shortens the mean free path due to the addition of a large resistivity per atomic percent of Ge - - $\rho_{Ge~in~Cu} \approx 37~\text{n}\Omega\text{m/at}$. % [95],

Metal	T	ρ	λ	$r = \lambda/10$ nm	l_{sf}	$r^*=l_{sf}/10nm$
	K	$\mathbf{n}\Omega\mathbf{m}$	nm		nm	,
Cu	295	21±1	31±2	~3.1	~290	~ 29
CuGe	295	180±9	3.7 ± 0.2	~0.37	~50	~ 5
Cu	4.2	5±1	132±20	~13.2	~1000	~ 100
CuGe	4.2	162±7	4.1±0.2	~0.41	55±5	~ 5.5

Table 3.1: The resistivity (ρ) , mean free path (λ) and spin diffusion lengths (l_{sf}) for Cu and CuGe at 295 and 4.2 K. We also list the ratios $\mathbf{r} = \lambda/10$ nm and $\mathbf{r}^* = l_{sf}/10$ nm for reference.

- 2. causes only weak spin flipping, as Ge has a small spin orbit cross section in Cu $-\sigma_{so}\approx 5.2\times 10^{-19}~{\rm cm}^2~[138], \text{ and thus a long spin diffusion length,}$
- 3. is soluble in $Cu \approx 10\%$ [139].

3.3.2 Parameters

To specify the differences between our samples with Cu and CuGe, we need estimates of the mean free paths (λ) and spin diffusion lengths (l_{sf}^N) for our samples. We used the free electron relation between mean free path (λ) and resistivity (ρ) for Cu: $\lambda \rho = 0.66 \text{ f}\Omega\text{m}^2$ [95, 24] to estimate λ using the values of ρ measured independently on 200 nm thick films by the Van der Pauw technique [55] (see appendix A.1). We list our estimates of resistivity (ρ) and mean free path (λ) in table 3.1. The ratio $r = \lambda/(t_N=10\text{nm})$ specifies whether the transport is ballistic $(r\gg 1)$ or diffusive $(r\ll 1)$. For Cu we find $r \geq 3$ and for CuGe $r \leq 0.4$.

The value of l_{sf}^{Cu} at 4.2 K has been estimated by earlier studies (see for example [45]). Since the value of our ρ_{Cu} agrees well with the earlier values, we used l_{sf}^{Cu} from those earlier studies [45]. The values at room temperature are obtained by scaling l_{sf} using the approximate relation $l_{sf}\rho\sim$ constant. The value of l_{sf}^{CuGe} was estimated

using the spin orbit cross section (σ_{SO}) measured by electron spin resonance [138], and λ , in the Valet Fert equation for l_{sf}^N [33], as we now describe. The value of σ_{SO} for Ge in Cu in ref. [138] is $\sigma_{SO} \approx 5.2 \times 10^{-19}$ cm². Using this σ_{SO} , the spin flip length (λ_{sf}) for this dilute alloy can be calculated using the relation [45].

$$\lambda_{sf}^{N} = \lambda_{N}^{so} = \frac{1}{nc\sigma_{so}} \tag{3.8}$$

where n is the number of host atoms per unit volume and c is the Ge concentration in %. For our CuGe alloy, we have $n=4/(3.61 \text{ Å})^3=11.664\times 10^{-30} \text{ m}^3$ (Cu is FCC with 4 atoms per unit cell, and lattice constant of Cu = 3.61 Å), and c = 5 /100. Using these parameters, and σ_{so} for Ge in Cu, we get $\lambda_{sf}^{CuGe} \approx 4500 \text{ nm}$. l_{sf}^{CuGe} at 4.2 K is then estimated using λ_{sf}^{CuGe} and λ_{CuGe} in the Valet-Fert equation [33]

$$l_{sf}^{N} = \sqrt{\frac{\lambda \lambda_{sf}}{6}} \tag{3.9}$$

The result is l_{sf}^{CuGe} (4.2 K) $\approx 55 \pm 5$ nm. The values at room temperature are obtained by scaling l_{sf} as mentioned above. Recently, a value of l_{sf} (Cu(2 at. % Ge) $\sim 117^{10}_{-6}$ nm [140] was obtained experimentally. Scaling to 5%, this value agrees, to within experimental uncertainties, with the present estimate of l_{sf}^{CuGe} . We list our spin diffusion lengths in table 3.1 along with the ratios $\mathbf{r}^* = l_{sf}/(\mathbf{t}_N = 10 \, \mathrm{nm})$. For both Cu and CuGe, we find $\mathbf{r}^* \geq 5$.

3.3.3 Samples and Data

To measure the switching current, we fabricated and measured nano-pillar samples with the structure Cu(80)/Py(24)/N(10)/ Py(6)/Cu(2.5)/Au(100), with N= Cu or CuGe, using the process described in section 3.2. All layer thicknesses are in nm.

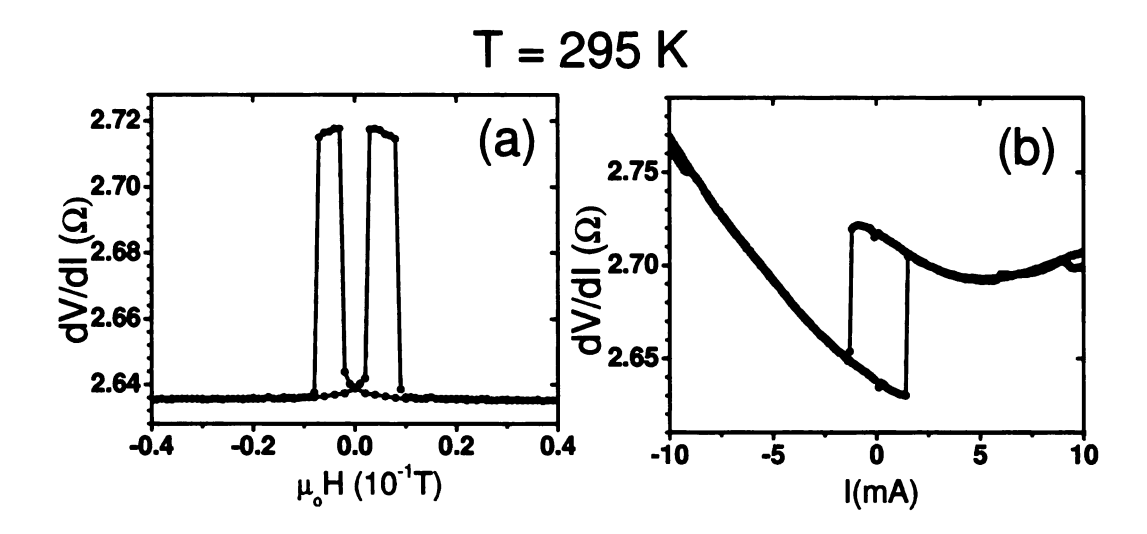


Figure 3.11: An example of: (a) Magnetoresistance, and (b) Spin torque induced switching for a Cu sample measured at 295 K. The parabolic nature of the background dV/dI curve, and the asymmetry about I=0, are probably due to Joule heating and the Peltier effect [141].

Strictly, the spin transfer torque models discussed in section 3.1 predict torque, which relates to the onset of dynamical instability. Unfortunately the onset of dynamical instability is hard to directly measure. To obtain parameters that are well defined, we chose to measure the currents at which sharp switching occurs, such as shown in figures 3.1 and 3.11.

In figures 3.11 and 3.13, we show: (a) magnetoresistance, and (b) current switching data for Cu and CuGe nano-pillar samples at 295 K. At 295 K, the switching was usually simple and clean. In figures 3.12 and 3.14 we show: (a) magnetoresistance, and (b) current switching data for Cu and CuGe nano-pillar samples at 4.2 K. At 4.2 K, although we can infer single switching steps in both figures, the overall structures are more complex. In figure 3.12, we may be seeing evidence of onset of instabilities before the switching.

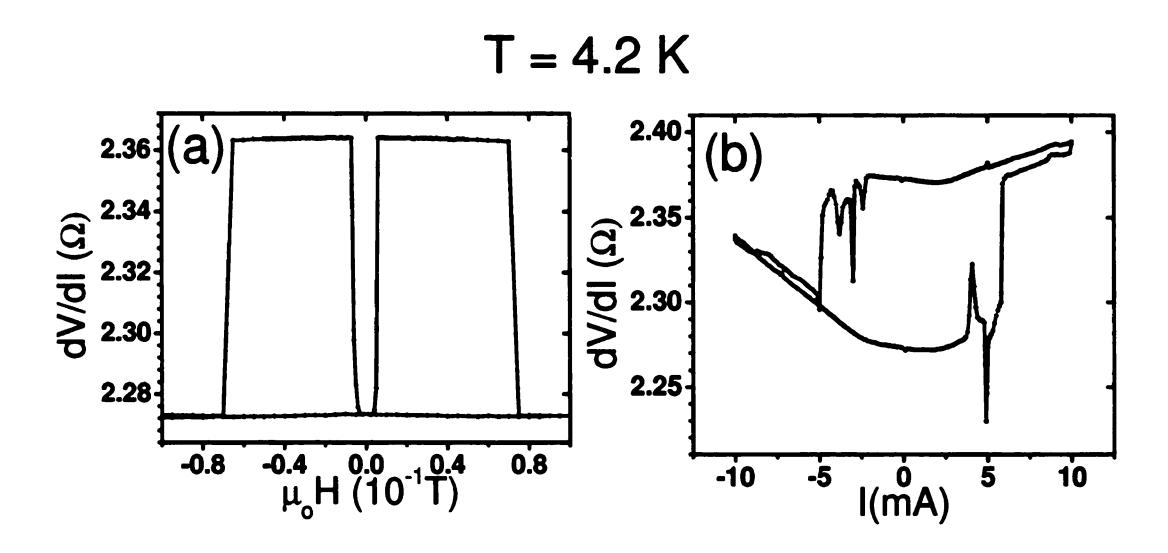


Figure 3.12: An example of: (a) Magnetoresistance, and (b) Spin torque induced switching for a Cu sample measured at 4.2 K. The spin torque induced switching is noisy but still the sharp transition from P to AP and vice-versa could be identified.

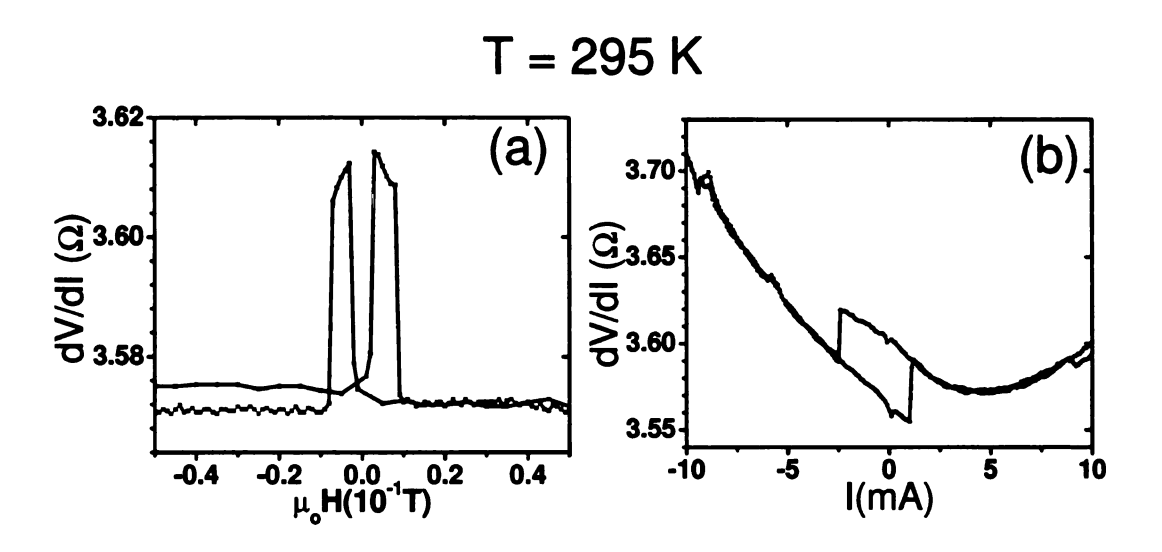


Figure 3.13: An example of: (a) Magnetoresistance, and (b) Spin torque induced switching for a CuGe sample measured at 295 K.

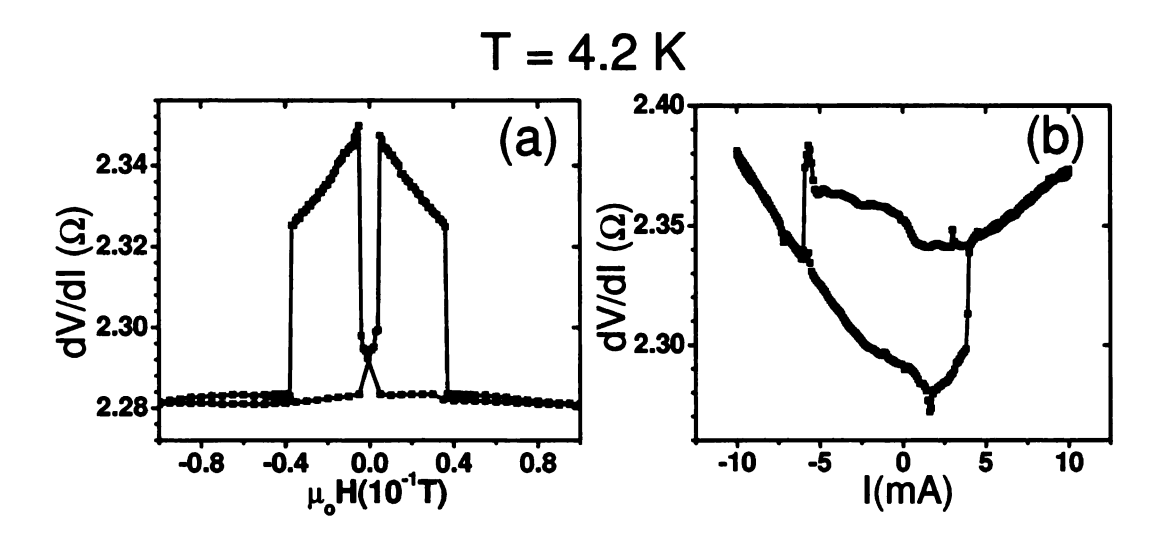


Figure 3.14: An example of: (a) Magnetoresistance, and (b) Spin torque induced switching for a CuGe sample measured at 4.2 K.

Sharp switching is however not always achieved; i.e the transition from P to the AP and vice versa sometimes involves multiple steps. We show an example of two step switching in figure 3.15. To avoid bias from alternative choices of ΔI , we exclude such multi-step data from our analysis and consider only samples for which we get sharp single step switching.

As noted in section 1.6, this project was carried out jointly by me and Dr. N. Theodoropoulou. We made and measured samples independently. Our joint data is listed in table 3.2. The subset of data from my samples only is listed in table 3.3. My data subset is for 19 samples, of which five (3 Cu, 2 CuGe) gave sharp switching at both 295 K and 4.2 K, with the remaining fourteen samples giving sharp switching at 295 K only. Comparison of my data subset with the joint data shows that both generally agree to within mutual uncertainties. We will thus use the estimates from the joint data set to compare with the theory.

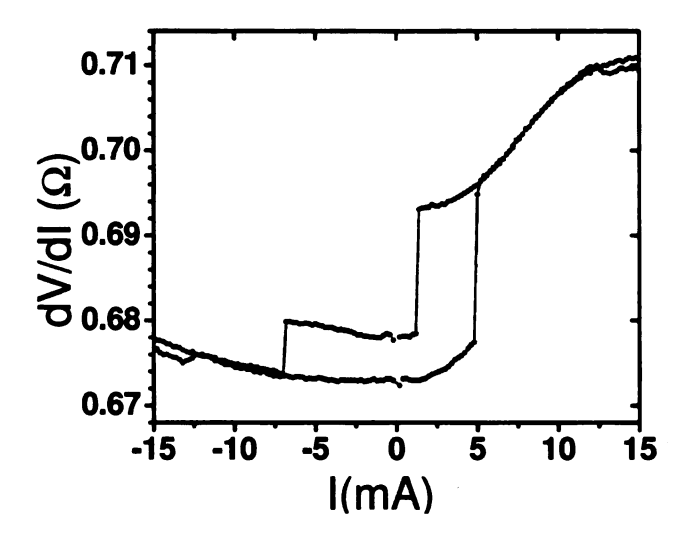


Figure 3.15: An example of switching from P to AP in two steps. We **exclude** such data from our analysis.

3.3.4 Check for systematic errors

Before comparing our data with theory, it is important to check for possible systematic errors. First we do an internal check between our Cu and CuGe data, and then an external Check, where we compare our Cu data with earlier values.

Both checks involve a result from an earlier nano-pillar study [142] by our group with F1 = F2 = Py and N = Cu, or Cu(5 at. % Pt) alloys sandwiched between Cu. Pt causes strong spin flipping but modest elastic scattering. For those samples, the inverse of the critical switching currents, $1/I_c^+$ or $1/I_c^-$, were found to be directly proportional to the change in resistance $\Delta R = R(AP)-R(P)$. Linear fits to the data gave nearly zero intercepts for both $1/I_c^+$ and $1/I_c^-$. We, thus, assume that any non-zero intercepts are small and that we can express the relation as $\Delta R\Delta I = \text{constant}$.

For the internal check, we use this relation to compare our data for Cu with CuGe. We see in table 3.2 that the data agree with this relation, to within mutual

Sample	R(AP)	ΔΙ	ΔR	$\Delta R \Delta I$	I_c^+/I_c^-
	Ω	mA	$\mathbf{m}\Omega$	mV	
295 K					
Cu (7)	2.2±0.8	5.5 ± 1.0	56 ± 16	0.31 ± 0.11	1.22±0.16
CuGe (6)	2.2±1.0	7.5±1.6	41±4	0.31 ± 0.07	1.1±0.3
Cu (29)	2.0 ± 0.4	6.0 ± 0.8	57±14	0.34 ± 0.10	1.25±0.12
CuGe (23)	1.5 ± 0.2	8.3±0.8	35±6	0.29 ± 0.06	1.03±0.15
4.2 K					
Cu (7)	1.9±0.8	$9.4{\pm}1.4$	114±30	1.07±0.32	1.5±0.3
CuGe (6)	1.9 ± 1.0	10.2±2.0	87±14	0.89 ± 0.22	0.9±0.1

Table 3.2: The values from a joint data set (see text). The numbers in the brackets show the number of samples. The Cu(7) and CuGe(6) samples gave good switching at both 295 K and 4.2 K. The remaining samples gave good switching only at 295 K. The uncertainties are twice the standard deviation of the mean. The table is after [110, 111].

Sample No.	R(AP)	ΔΙ	ΔR	$\Delta R \Delta I$	I_c^+/I_c^-
	Ω	mA	$m\Omega$	mV	
295K					
Cu(3)	3.1±1	4.8 ± 2.1	60±30	0.24 ± 0.02	1.2 ± 0.3
CuGe(2)	3.6±0.1	5.3±3.4	43	0.21±0.12	0.8 ± 0.8
Cu(7)	1.8±0.7	6.5 ± 1.7	50±10	0.3±0.04	1.2 ± 0.2
CuGe(7)	1.44±0.14	$9.4{\pm}1.7$	40±10	0.35 ± 0.05	1.3 ± 0.2
4.2K				-	
Cu(3)	2.9±1.2	9.4±2.6	100±40	1±0.1	1.2 ± 0.2
CuGe(2)	3.4±2.2	8.7±2.4	80±40	0.67±0.17	0.8 ± 0.3

Table 3.3: The subset data for my samples only. The numbers in the brackets show the number of samples. The Cu(3) and CuGe(2) samples gave good switching at both 295 K and 4.2 K. The uncertainties are twice the standard deviation of the mean.

uncertainties, at both 4.2 K and 293 K.

For the external check, we compare our values with the prior measurements for Cu nanopillars by Kurt et al [143], which gave $\Delta R\Delta I = 0.399 \pm 0.024$ at 295 K and $\Delta R\Delta I = 1.09 \pm 0.054$ at 4.2 K. Our estimates listed in table 3.2 agree, to within mutual uncertainties, with those prior estimates.

These two agreements suggest that possible systematic errors at 4.2 K and 295 K are not large.

3.3.5 Results

For the data in table 3.2, we calculate the ratio $X = \Delta I_{CuGe}/\Delta I_{Cu}$. At 295 K, we find $X = 1.4 \pm 0.4$ for 13 samples and 1.4 ± 0.2 for the rest of the 52 samples and at 4.2 K, $X = 1.1 \pm 0.3$ for 13 samples. In principle, the values of 4.2 K should be more appropriate to be compared with theory. However, possibility of unwanted effects at 4.2 K, such as surface oxide (see section 3.3.7), may affect this value. We thus take the best estimate as an average of our 4.2 K and 295 K values - - $X \approx 1.25 \pm 0.2$.

For the data in table 3.2, the ratio of switching currents for Cu are $I_{Cu}^+/I_{Cu}^- \sim 1.25$ at 295 K and $I_{Cu}^+/I_{Cu}^- \sim 1.5$ at 4.2 K. For CuGe $I_{CuGe}^+/I_{CuGe}^- \sim 1.05$ at 295 K and $I_{CuGe}^+/I_{CuGe}^- \sim 0.9$ at 4.2 K.

3.3.6 Calculations

For comparison with the ratios derived from the experimental data, the calculations were done for the following four models. We list a summary of the estimates from the calculations in table 3.4. The values of calculations are taken from ref. [110, 111] (a) Ballistic Slonczewski model [8]: The ballistic Slonczewski model, without any spin flipping in the N layer, predicts X = 1, as the N layer does not matter. Correcting this model using equations 3.4 and 3.5 for spin flipping in N, gives $X = \exp(-t/l_{sf}^{Cu})/\exp(-t/l_{sf}^{Cu}Ge) \approx 1.2$. Neglecting any spin flipping, this model predicts $I_c^+/I_c^- = 4.8$ for a polarization P = 0.4, and reduces to $I_c^+/I_c^- = 2.0$ in the limit that P goes to zero.

(b) Experimental Model - - $\Delta R\Delta I$ = constant [142]: This model can be used to estimate X by calculating the ratio $\Delta R(\text{CuGe})/\Delta R(\text{Cu})$. For this model we get X

Model	X	$I_c^+/I_c^-(Cu)$	$I_c^+/I_c^-(CuGe)$
Ballistic	(a) 1.0	2.0	4.8
Slonczewski model [8]	(b) 1.2		
Experimental model	1.6	-	-
$\Delta R\Delta I = constant [142]$			
Fert model [135]	2.2	0.9	2
Boltzmann eq. model [134]	2.0±0.13	2.7±0.27	1.8±0.06
Experiments (295 K)	1.4±0.2	1.24±0.15	1.1±0.3
Experiments (4.2 K)	1.1±0.3	1.5±0.3	0.9±0.1

Table 3.4: Calculated estimates of $X = \Delta I_{CuGe}/\Delta I_{Cu}$ and I_c^+/I_c^- for Cu and CuGe samples. The calculations based on the Ballistic Slonczewski model are for: (a) no spin flipping, and (b) with spin flipping. For comparison we also list in bold the estimates from our experiments based on the joint data set. The data listed in this table are taken from Refs. [110, 111].

- = 1.6. This model does not make any prediction for I_c^+/I_c^- .
- (c) Fert model [135]: This model calculates torque in terms of a combination of longitudinal spin currents and spin accumulations in a small angle approximation (almost collinear moments of the two F layers). It gives X = 2.2. For the ratio of switching currents, it predicts $I_c^+/I_c^- = 0.9$ for Cu and $I_c^+/I_c^- = 2$ for CuGe.
- (d) **Boltzmann equation model** [134]: This model calculates torque at all angles by numerically solving the Boltzmann equation. This model predicts $X = 2.0\pm0.12$. For I_c^+/I_c^- , this model predicts $I_c^+/I_c^- = 2.7\pm0.27$ for Cu and $I_c^+/I_c^- = 1.8\pm0.06$ for CuGe

We find that, except for the ballistic Slonczewski model, the calculated values of X are larger than the experimental values at both 295 K and 4.2 K. The agreement of our values with ballistic Slonczewski model is surprising as it cannot correctly describe our samples, which involve diffusive scattering. The estimates of I_c^+/I_c^- for both Cu and CuGe also do not agree with the calculations.

3.3.7 Sources of uncertainties

The discrepancy between the calculated and the experimental values might be due to several possible causes, which we list below. However, none of them looks compelling (a) **Thermal effects**: Formally, the calculations for the transport and magnetic dynamics are done for zero temperature. The likely effect of temperature on electronic transport would be to change scattering rates. The temperature dependence of torque should thus be weak.

(b) Magnetic effects: Especially at 4.2 K, magnetic anisotropies in the F layers might lead to complicated processes of reversal where ΔI is not closely related to the torque, as assumed in this study. However, such anisotropies are expected to be small in Py. Another possible effect at 4.2 K is formation of antiferromagnetic NiO on the surfaces of the Pv layers. Such NiO has been argued to affect switching [144] by producing local exchange bias, which produces variations in the switching field and occasional multiple steps. Our samples do show some variations in switching field at 4.2 K and 295 K. But any effects due to NiO should also be similar for Cu and CuGe. (c) Experimental: The models calculate the initial dynamical instability, whereas we measure reversal. The models assume a macrospin, whereas the experimental reversal may be non-uniform. But as these complications do not differ for Cu and CuGe, it isn't clear that they would simply affect the results. The structure of the sample also differs from that assumed in the calculations. The calculations assume linear devices with uniform current flow, whereas our sample geometry is more complex leading to non-uniform flow of current. As discussed in refs. [145, 146], the corrections for such non uniformity might differ for Cu and CuGe. But as our nano-pillar samples have a larger cross-section than both the layer thicknesses and the mean free paths (except for Cu at 4.2 K), we don't expect the three dimensional treatments of the two sets of samples to differ much.

(d) Theoretical approach: The models approximate the Fermi surfaces as spheres. They also treat interfaces as specular and ignore any spin flipping at the interfaces. But how much change would be achieved by relaxing these conditions is not yet known. An alternative theoretical approach would be to do full quantum mechanical calculations [147, 137]. But it is hard to include diffusive scattering in such calculations.

3.4 Summary

We have studied the effect on the spin transfer torque of changing the transport in the N layer separating the fixed and free F layers from ballistic to diffusive. For ballistic transport we chose N = Cu (r \geq 3), and for diffusive transport we chose N = Cu(5 at.% Ge) (r \leq 0.4). We compared two quantities at both 295 K and 4.2 K: (a) X = $\Delta I_{CuGe}/\Delta I_{Cu}$, and (b) I_c^+/I_c^- for Cu and CuGe. We found that X = 1.4 \pm at 295 K and X = 1.1 \pm 0.3 at 4.2 K. These values are not far from unity, suggesting that there is not much difference in spin torque for ballistic or diffusive transport in the N metal. The estimates of I_c^+/I_c^- are \sim 1.24 (295 K) and \sim 1.5 (4.2 K) for Cu and \sim 1.1 (295 K) and \sim 0.9 (4.2 K) for CuGe. We compared our experimental estimates with calculations based on four spin torque models, as listed in table 3.4. Our estimate of X is less than both the Fert and Boltzmann equation models. Our estimate of X at

4.2 K is also less than that from an experimental model assuming $\Delta R\Delta I = {\rm constant.}$ In contrast, our estimate of X is close to that of the initial ballistic Slonczewski model. Such an agreement is surprising, as the ballistic Slonczewski model cannot correctly describe our samples, which involve diffusive scattering. For I_c^+/I_c^- , we found that our estimates do not agree with any of the three models that make predictions. Though our estimates do not generally agree with the various theories, we hope that our results will stimulate new work on spin torque theories, and thereby help to better understand the physics of spin transfer torque.

Chapter 4

Antiferromagnetic spintronics studies

These projects have been done in collaboration with Z. Wei, J. Basset and Prof. M. Tsoi at University of Texax, Austin. The collaborative work has led to five publications. The first publication, in which I am the second author, was on the effect of current on exchange bias on FeMn/CoFe samples [17]. Experiments extending these studies on effect of current on exchange bias to another AFM = IrMn, and then to another F = Py, led to two publications [18, 19], where I am the second and the third author, respectively. The studies to search for AGMR effects led to one publication [148], in which I am the second author. The studies on effect of current on exchange bias, based on our FeMn/CoFe experiments and related studies by others, led to a review article [149], in which I am the second author.

In this chapter, we present our experiments to search for spintronics effects with antiferromagnets (AFM) predicted by Nunez, Haney and coworkers [13, 14, 15, 16]. We have done two sets of experiments to look for: (a) the effect of current on exchange bias in exchange biased spin valves (EBSV), and (b) antiferromagnetic giant magnetoresistance (AGMR) effects in multilayers containing antiferromagnets. In these

projects I fabricated and processed the multilayer samples which were measured by our collaborators at University of Texas, Austin. For these studies, I will limit my self to describing the experiments and listing the main experimental findings.

Apart from our experiments, the effects of current on exchange bias has also been examined by Urazhdin and Anthony [20] in the CPP geometry, and by Tang et al [21] and Nam et al [22] in the CIP geometry. These three studies, in addition to our F = CoFe, AFM = FeMn experiments, were recently reviewed in ref [149]. The review suggests that the understanding of the effect of large currents on the exchange bias is still 'incomplete'.

The chapter is organized as follows. In section 4.1, we give a brief overview of the role of antiferromagnets in 'exchange bias'. In section 4.2 we review the theoretical predictions of antiferromagnetic spintronics effects. In section 4.3, we describe our samples and the point contact measurement procedure. The experiments to study the effects of current on exchange bias are presented in section 4.4. The experiments to look for AGMR effects are presented in section 4.5. In section 4.6 we summarize our findings.

4.1 Exchange Bias

The use of antiferromagnets in ferromagnetic spintronics studies is not new. Antiferromagnets have been actively used in ferromagnetic spintronics studies to pin an adjacent F metal by exchange bias, which provides control of the magnetic configuration [44] in F/N/F layers. The role of AFMs in spintronics studies, however, has been limited to pinning only. Our studies are the first to look for effects of large current

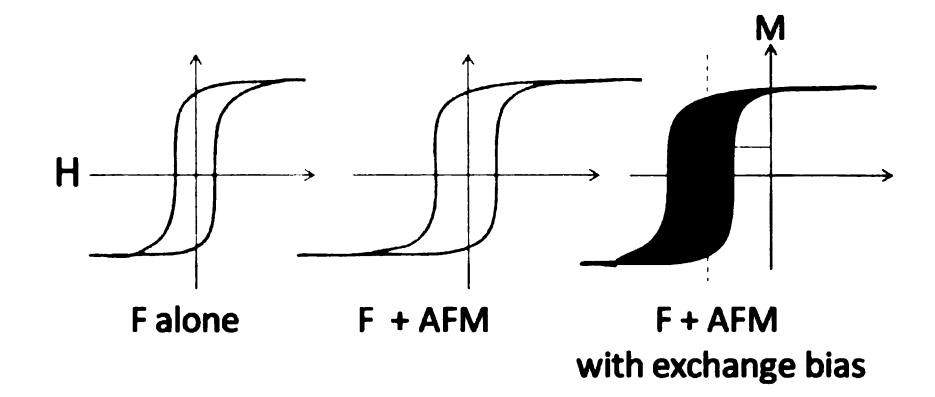


Figure 4.1: A cartoon showing the effect of exchange bias at an F/AFM interface on hysteresis. The left figure shows a hysteresis curve for a F layer. The middle figure shows the hysteresis curve for a F + AFM layer, but without any exchange bias. The right curve shows the hysteresis curve for F + AFM layer with exchange bias. As mentioned in the text, the exchange bias is induced by heating the sample above the blocking temperature of the AFM and then cooling in a field.

densities on exchange bias.

Exchange bias was first observed by Meiklejohn and Bean [150] in 1956 in surface oxidized fine particles of Co. The surface oxidation of Co formed CoO, resulting in an inner core of ferromagnetic Co but an outer shell of anti-ferromagnetic CoO, thus forming a F/AFM structure. The exchange bias between the F and AFM layer was induced by heating the samples above the Neel temperature of the AFM and then cooling in a magnetic field. The exchange bias pins the adjacent F so that higher fields are required to switch it as compared to an unpinned F.

In F/N/F trilayers, such pinning can be used to achieve well defined parallel (P) and anti-parallel (AP) states (see section 1.2.3). We show in figure 4.1, a cartoon of the role of exchange bias on the hysteresis curve of an F layer, an F layer with an AFM layer, and an F layer with an AFM layer and exchange bias induced. The models of exchange bias attribute pinning to F/AFM interfacial moments [151, 152].

4.2 Theoretical predictions

Nunez et al [13] and Haney et al [14, 15, 16], used a non equilibrium Green's function (NEGF) approach, with density functional theory (DFT), to predict that spintronics effects, similar to GMR and STT, could occur in systems where the F layers are replaced by AFM layers. The use of AFM metals in place of F metals eliminates the effects of shape anisotropy and could thus offer better control of the magnetic state.

Nunez, Haney and coworkers [13, 14, 15, 16] proposed that the exchange bias at the F/AFM interface could be affected by application of a large perpendicular to the plane (CPP) current density 'j'. Affecting exchange bias with currents opens up the possibility of controlling the exchange bias in magnetic devices. In addition to the prediction of affecting exchange bias by current, Nunez, Haney and coworkers [13, 14, 15, 16], also proposed that the resistance of an AFM trilayer -- AFM/N/AFM, assuming ordered AFMs, could change when the relative orientation of the magnetic moments in the two AFM layers next to the N-layer changes. The configuration, parallel (P) or anti-parallel (AP), was defined by the relative orientations of the AFM layers next to the N layer separating the two AFMs. We show a cartoon of such an AFM/N/AFM trilayer in figure 4.2. In analogy to GMR with ferromagnets, they called this effect antiferromagnetic giant magnetoresistance (AGMR). The resistance changes were predicted to be comparable in size to those for ferromagnetic GMR.

They further predicted that the magnetic order of the AFM/N/AFM trilayer could also be changed by injecting large currents perpendicular to the plane. They

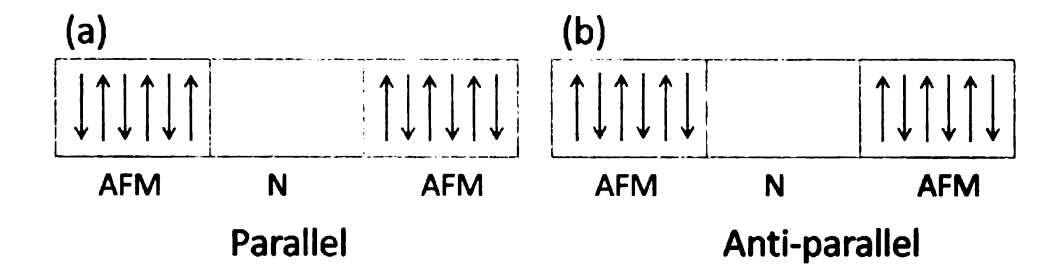


Figure 4.2: A cartoon showing AFM orientations for an antiferromagnetic GMR effect. The arrows represent the orientations of the individual moments. (a) The moment orientations adjacent to the middle N layer are parallel - - parallel configuration. (b) The moment orientations adjacent to the middle N layer are anti-parallel - - anti-parallel configuration.

estimated a critical $j_{AFM}\sim 10^5$ A/cm² needed to reverse the magnetic order (P to AP or vice versa) of an AFM/N/AFM trilayer. Such a critical j_{AFM} is much less than the critical $j_F\sim 10^7$ A/cm² [8] needed to reverse the magnetic order in F/N/F multilayers. They claimed that the predicted $j_{AFM}\ll j_F$ because the spin transfer torque in the AFMs acts on a large portion of the AFM metal, in contrast to F Metals where the spin transfer torque acts only near the N/F interface.

In addition to calculations by Nunez, Haney and coworkers [13, 14, 15, 16], Gomonay and Loktev [155] used numerical calculations to confirm that polarized currents can destabilize the equilibrium state of an AFM.

Recently, Xu et al [156], using first principles, calculated AGMR for AFM/ N/AFM/ N = FeMn/ Cu/FeMn/ Cu multilayer structure and found it to be in agreement with the predictions of Nunez, Haney and coworkers [13, 14, 15, 16].

All of the calculations mentioned above assumed perfect layers and ballistic transport. The predicted AFM spintronics effects are due to quantum coherence. In contrast, real samples are generally imperfect and have diffusive scattering, which should weaken quantum coherence and thereby the predicted AFM spintronics effects. Experiments are thus crucial to see if such effects can be observed in real samples. The models mentioned above can only serve as qualitative guidelines to the experiments.

4.3 AFM samples and measurement

The samples to study the antiferromagnetic spintronics effects were sputtered using a process described in chapter 2. The samples fall into two categories

- Simple Exchange biased spin valve (EBSV) to study the effect of large current density on exchange bias. The structure of these samples is $\text{Cu}(80\text{nm})/\text{AFM}/\text{F}_1/\text{N}(10\text{nm})/\text{F}_2/\text{Au}(5\text{nm})$ (regular), or $\text{Cu}(80\text{nm})/\text{F}_2/\text{N}/\text{F}_1/\text{AFM}/\text{Au}(5\text{nm})$ (inverted) where AFM = FeMn or IrMn and F₁ = F₂ = CoFe or Py.
- Mixed multilayer samples with variable constituents to search for AGMR.

The EBSVs and mixed multilayers with F/AFM layers were pinned by heating above the blocking temperatures of the AFM ~ 450 K for FeMn and ~ 527 K for IrMn, and then cooling in a magnetic field ~ 180 Oe. A bottom thick buffer Cu (~ 50 nm) layer was grown before the active sample structure for an approximately perpendicular to the plane current flow. To protect the samples from atmospheric contamination, the top layer of the sample was covered by ~ 5 nm thick Au layer.

These multilayer films were fabricated and processed by me, but were measured at 295 K by our collaborators at University of Texas, Austin, using a mechanical point contact set up. Mechanical point-contacts $\sim 10\text{-}100$ nm in diameter were used to inject a large CPP current density (up to $\sim 10^8$ A/cm²) into the film. The resistance

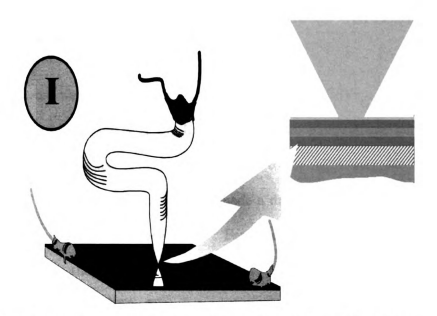


Figure 4.3: A cartoon of the point contact measurement setup. The inset shows a blowup of the point contact and the multilayer region. The figure is courtesy of Prof. M. Tsoi, University of Texas, Austin.

of the contact was measured as a function of the in-plane magnetic field at different values of currents. Figure 4.3 shows a cartoon of the point contact measurement setup. The inset shows a blowup of the point contact and the multilayer region. Here negative current corresponds to the flow of electrons from the tip into the multilayer.

4.4 Experiments to study the effect of current on exchange bias

In these experiments we used EBSV samples. In the regular EBSVs, as described in section 4.3, the AFM layer is at the bottom of the two F layers and negative current corresponds to the flow of electrons through F to the AFM layer. To test if growing the AFM layer on top of the F layers made a difference, we also measured inverted EBSVs, as described in section 4.3. For inverted samples, the negative current corresponds to the flow of electrons through the AFM to the F layer. For both regular and inverted EBSVs, F_1 refers to the fixed 'pinned' layer and F_2 to the free layer. The N layer was kept thick enough (\sim 10 nm) to minimize exchange coupling (see section 1.2.3) between the two F-layers. Further, the two F-layers were wide enough (\sim mm) to minimize dipolar coupling. The external magnetic field was applied in the plane of the layers. Initially these studies were done for AFM = FeMn (=Fe₅₀Mn₅₀) and F = CoFe (=Co₉₁Fe₉). To test effects by changing AFM or F, the studies were then extended to another AFM = IrMn (= Ir₂₀Mn₈₀) and then to another F = Py (=Ni₈₄Mn₁₆).

4.4.1 AFM= FeMn (=
$$Fe_{50}Mn_{50}$$
), F = CoFe (= $Co_{91}Fe_{9}$)

We started with AFM = FeMn (3 or 8nm) and F_1 (3 or 10 nm), F_2 (3 or 10 nm)= CoFe for all combinations of the specified F and AFM thicknesses.

Figure 4.4 shows an example of the switching curves for a sample with t(FeMn)=8nm, $t(F_1)=10nm$, and $t(F_2)=3$ nm, at different applied currents. The point contact resistance was R=0.92 Ω and I=30 mA corresponds to $j\sim 2$ x 10^8 A/cm².

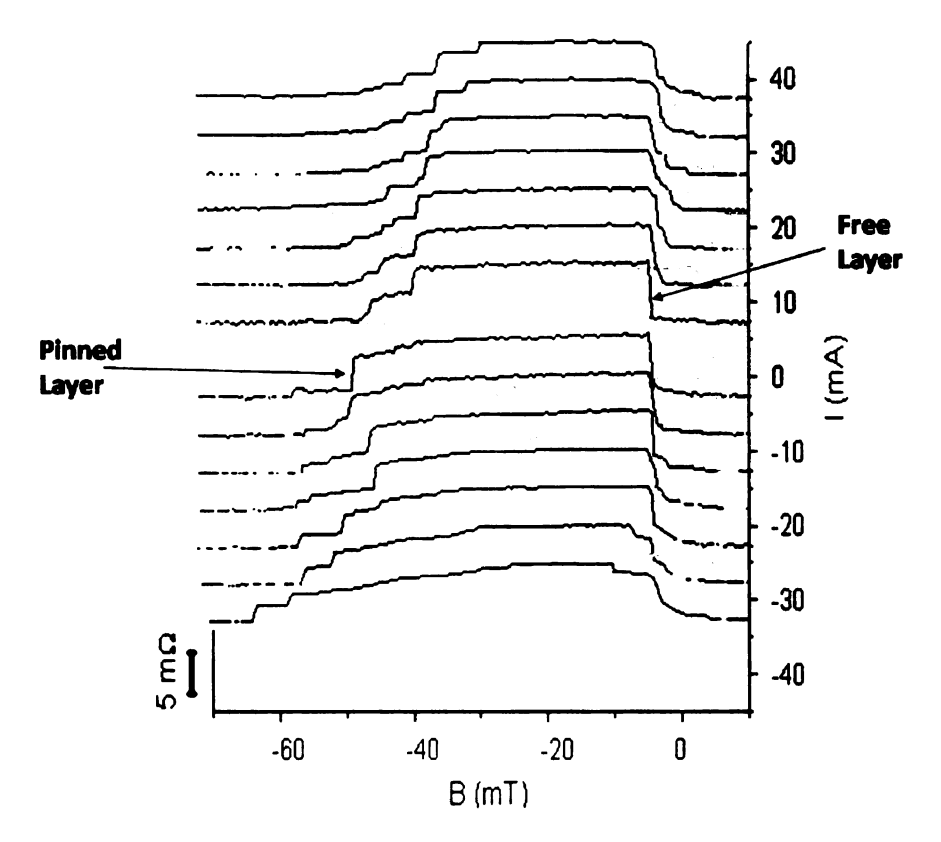


Figure 4.4: Resistance vs. magnetic field for a series of applied currents for a FeMn(8)/CoFe(3)/Cu(10) / CoFe(10) sample. All layer thicknesses are in nm. The solid black curves are down sweeps (positive to negative magnetic fields) and grey curves are up sweeps (negative to positive magnetic fields). The figure is from [17].

The dark curves represent sweeps from positive to negative field, and the light curves show reverse sweeps from negative to positive field.

We see in figure 4.4 that the switching field of the free layer F1 is independent of the magnitude of I and shows very little broadening. In contrast, the switching field of the fixed layer F_2 varies with the applied current - - the midpoint of the F_2 switching field shifts with I - - increases for negative I and decreases for positive I. The F_2 switching field also broadens as the magnitude of I increases. The shifts in the switching field of the fixed layer are opposite for positive and negative currents. The opposite shifts in the switching field of the fixed layer rule out the possibility of

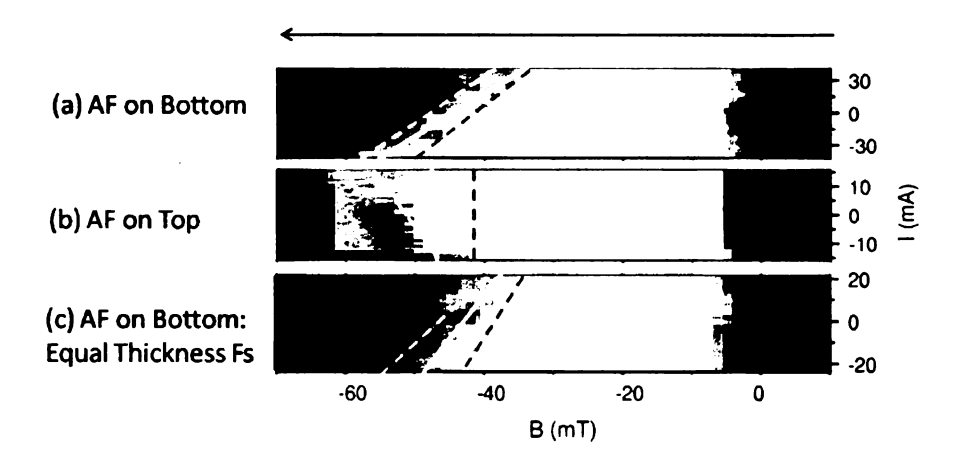


Figure 4.5: Grey scale plots of resistance vs magnetic field for different values of current. Here white represents the maximum R and black represents minimum R. The data shown is for an down sweep - - positive to negative magnetic field. The lines show linear fits to the data at 30% (dashed white), 50% (solid white) and 70% (dashed black) of full scale [100% = R(AP) - R(P)]. The three plots are for: (a) an FeMn(8)/ CoFe(3)/ Cu(10) / CoFe(10) sample (same as that of figure 4.4); (b) CoFe(10)/ Cu(10) / CoFe(3)/ FeMn(8) sample (inverted); and (c) FeMn(8)/ CoFe(3)/ Cu(10) / CoFe(3) sample. All layer thicknesses are in nm. The figure is from [17].

these effects being due to Joule heating, which should be symmetric with respect to I=0. Joule heating, however, might contribute to the broadening of the switching transitions.

We plot the resistances as a function of magnetic field and applied current on a gray-scale plot to fit the shifts of the switching fields of the fixed and the free layers. For the fit, we assumed straight lines. Figure 4.5 (a) shows the gray-scale plot for the dark curve data of figure 4.4. The white color in figure 4.5 (a) represents the maximum resistance (corresponding to the anti-parallel (AP) state of F_1 and F_2) and black represents the minimum resistance (corresponding to the parallel (P) state of F1 and F2). The straight lines are fits to 30% (dashed white), 50% (solid white), and 70% (solid black) of the full scale [100% = R(AP) - R(P)]. We include three fits

to show the sensitivity of variations to the choice of %. Qualitatively the result is independent of the choice of 30%, 50% or 70%.

About 29 point contacts were measured on different samples. All measurements gave generally similar results, indicating that the observed effects were not limited to any particular contact or layer thicknesses. Out of those 29 contacts, we show representative data for two more measurements in figure 4.5 (b) and (c). The data in figure 4.5 (b) are for a inverted sample with t(FeMn) = 8nm, $t(F_1) = 10nm$, and $t(F_2) = 3$ nm. Due to the inverted structure, each current direction is reversed and thus the current induced effects on the F_2 switching field should also be reversed. Aside from the reversal, the general behavior is similar to that of the data in figure 4.5 (a). In figure 4.5 (c), we show data for a regular EBSV with $t(F_1) = t(F_2) = 3$ nm and t(FeMn) = 8nm. The data for this sample look very similar to the data in figure 4.5 (a).

4.4.2 AFM=IrMn (=
$$Ir_{20}Mn_{80}$$
), F = CoFe (= $Co_{91}Fe_{9}$)

To test if changing the AFM would make a difference, we extended our experiments to another AFM = IrMn(8nm) but still with same F_1 (3 or 10 nm) = F_2 (3 or 10 nm)= CoFe. We found generally similar results to those for the AFM = FeMn case. As representatives of our IrMn studies, we show data for a regular IrMn(8 nm)/ CoFe(3 nm)/ Cu(10 nm)/ CoFe(10 nm) EBSV in figure 4.6: (a) for up sweep - - negative to positive magnetic field, and (b) for down sweep - - positive to negative magnetic field. We chose data for a sample with the same structure as that of the AFM = FeMn sample in figure 4.5. We follow the same notation as in figure 4.5, white represents

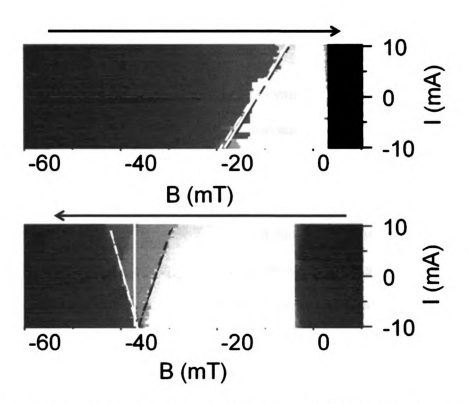


Figure 4.6: Grey scale plots of resistance vs magnetic field for different values of current for an IrMn(8)/CoFe(3)/Cu(10)/CoFe(10) sample. All layer thicknesses are in nm. Here white represents the maximum R and black represents minimum R. The upper figure is for an up sweep - - negative to positive magnetic field, and the bottom figure is for a down sweep. The lines show linear fits to the data at 30% (dashed white), 50% (solid white) and 70% (dashed black) of full scale [100% = R(AP) - R(P)]. The figure is from [18].

the maximum resistance and black minimum resistance. The straight lines are fits to 30% (dashed white), 50% (solid white), and 70% (solid black) of the full scale [100% = R(AP) - R(P)].

4.4.3 AFM=FeMn (=
$$Fe_{50}Mn_{50}$$
) and IrMn (= $Ir_{20}Mn_{80}$),
F = Py (= $Ni_{84}Mn_{16}$)

In the previous subsection, we saw that changing the AFM from FeMn to IrMn for F = CoFe gave little change in results. To test if changing F affects our observations,

we extended our studies to F = Py for both AFM = FeMn and IrMn. We present together our initial studies of both AFMs with Py.

For F = Py, the current generally affects the switching fields of both the fixed and free layers. The effects, however, differ with the sample structure - - different for the two AFMs, and for a given AFM but with different thicknesses of F1 and F2. These results are in contrast to our observations with F = CoFe (for both AFM = FeMn or IrMn), where the current only affected the switching field of the fixed layer.

To illustrate the effects with F = Py, we present two representative data sets, one each for AFM = FeMn and IrMn. Figure 4.7 shows the data for an FeMn(8nm)/Py(10nm) / Cu(10nm) / Py(3nm). The current has a small effect on the switching field of the fixed layer, but a larger effect on the switching field of the free layer. In figure 4.7, the top plot is for an up sweep - - from negative to positive fields, and the bottom plot is for a down sweep. The fits show that both free layer and fixed layer switching fields move towards negative field with positive current and vice versa. Negative current also broadens the free layer switching field.

The data for an IrMn(8)/ Py(10) / Cu(10)/ Py(10) sample are shown in figure 4.8. Compared to data for Py with FeMn, this sample shows a more complicated behavior. The free layer switching field moves to more negative fields at positive currents, but remains unchanged for negative currents. Further, the fixed layer switching field moves to smaller negative field at negative currents, but remains unchanged for positive currents. The effect are mixed and complicated for these samples

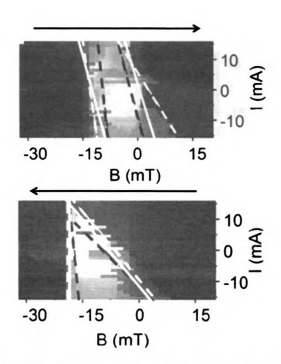


Figure 4.7: Grey scale plots of resistance vs magnetic field for different values of current for an FeMn(8)/ Py(10)/Cu(10) / Py(3) sample. All layer thicknesses are in m. Here white represents the maximum R and black represents minimum R. The upper figure is for an up sweep-negative to positive magnetic field, and the bottom figure is for a down sweep. The lines show linear fits to the data at 30% (dashed white), 50% (solid white) and 70% (dashed black) of full scale [100% = R(AP) - R(P)]. The figure is from [18].

4.4.4 Effect of current on exchange bias - - Analysis

The effects of current on exchange bias differ for different F metals.

- For F = CoFe, with both AFM = FeMn or IrMn, the free layer switching field is unaffected by current, but the fixed layer switching field shifts as well as broadens with current.
- For F = Py, the measurements show shifts in the switching field of both the free and fixed layers in a complicated manner. To have a better understanding of the physics, more experiments with F = Py are planned.

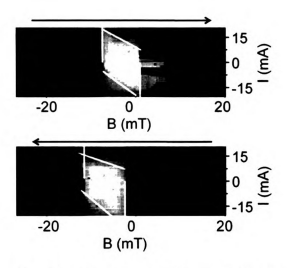


Figure 4.8: Grey scale plots of resistance vs magnetic field for different values of current for IrMn(8)/ Py(10)/ Cu(10) / Py(10) sample. All layer thicknesses are in m. Here white represents the maximum R and black represents minimum R. The upper figure is for an up sweep-negative to positive magnetic field, and the bottom figure is for a down sweep. The white lines show linear fits to the data at 50% of full scale [100% = R(AP) - R(P)]. The figure is from [18].

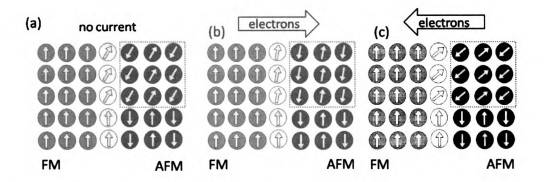


Figure 4.9: A schematic model showing the effect of the current on exchange bias. The grey color represents F metal and the black color represents an AFM metal. The vertical arrows at the F/AFM interface are fixed moments that give the exchange-bias. The tilted light grey arrows at the F/AFM interface are free moments, exchange coupled to the black AFM domain indicated by the dotted box. As current rotates this domain, the free grey moments rotate with it. Electrons going from F to AFM rotate the AFM domain toward the vertical, increasing the exchange-bias. Electrons going from AFM to F rotate the AFM domain away from vertical, decreasing the exchange-bias. The figure is taken from [17].

The general behaviors for F = CoFe observations are: (a) the switching field of the free layer remains independent of applied current; (b) electrons flowing through the AFM to F_1 layer (positive current) reduces the F_1 switching field - - i.e reduces pinning, and electrons flowing through F_1 to the AFM enhances pinning. Following the predictions of Nunez, Haney and coworkers [13, 14, 15, 16], the shift in the F_1 switching field could be qualitatively explained by a 'spin torque' model, which we show in figure 4.9.

The exchange bias between F (grey circles) and AFM (black circles) is attributed to the moments at the F/AFM interface [153, 26] (shown as light grey circles). Some of the interfacial moments are assumed to be fixed (vertical arrows in grey circle) and do not change with either magnetic field or applied current, giving pinning at I=0. The remaining F/AFM interfacial moments are assumed to be free (tilted arrows in light grey circle) but strongly exchange coupled to the bulk AFM domain. The applied current is assumed to exert a spin transfer torque on the bulk AFM domain, rotating it toward the direction of the F-moments for negative I or away from this direction for positive I. This rotation of the AFM domain causes rotation of the strongly coupled free moments at the F/AFM interface, thus increasing or decreasing pinning eventually affecting the F_1 switching field. For the free layer, the switching field appears independent of applied current, suggesting that regular spin transfer torque effects on the free layer are weak.

The model described above however does not fully explain our F = Py data. Moreover this model is not unique. Strictly, our measurements do not let us definitely establish whether the effects that we see are driven by spin torque effects in the AFM

(as in the model above), or are associated solely with the ${\it F/AFM}$ interface.

4.5 Experiments to search for antiferromagnetic giant magnetoresistance effects (AGMR)

To further try to test predictions by Nunez, Haney and coworkers [13, 14, 15, 16], we have also done experiments to search for antiferromagnetic giant magnetoresistance (AGMR) effects in AFM/N/AFM layers.

We initially started our measurements on AFM/N/AFM layers. But we saw no effects of current. We thus extended our studies to structures where the AFM/N/AFM layers had an F layer outside of one AFM. In our initial F/AFM/N/AFM samples, we only tested $t_F=3$ nm. Again we found no MR. We then studied structures where the AFM/N/AFM layers were sandwiched between two F layers. For these samples, we chose F1 = 3 or 10 nm and F2 = 3 or 10 nm. We saw a positive MR for samples with at least one $t_F=10$ nm.

We later realized that our observations, might be sensitive to the F layer thickness, so we extended our measurements to other sample structures of the form: AFM/F/N/AFM, F/AFM, and single F and AFM layers.

For these experiments, we chose AFM = FeMn and F = CoFe. To test for dependence on exchange bias and F thicknesses, we tested various combinations of layer thicknesses FeMn = 3 or 8 nm and CoFe = 2,3,4,6 or 10 nm. For the AFM/ N/AFM structures we tested all possible combinations of the two AFM thicknesses - - 3 /N /3, 3 /N /8, 8 /N /3, 8/N /8.

We found that the effects are sensitive to thickness of the F layer. We first list our observations (see figures 4.11 and 4.12) for different sets of samples, and then analyze

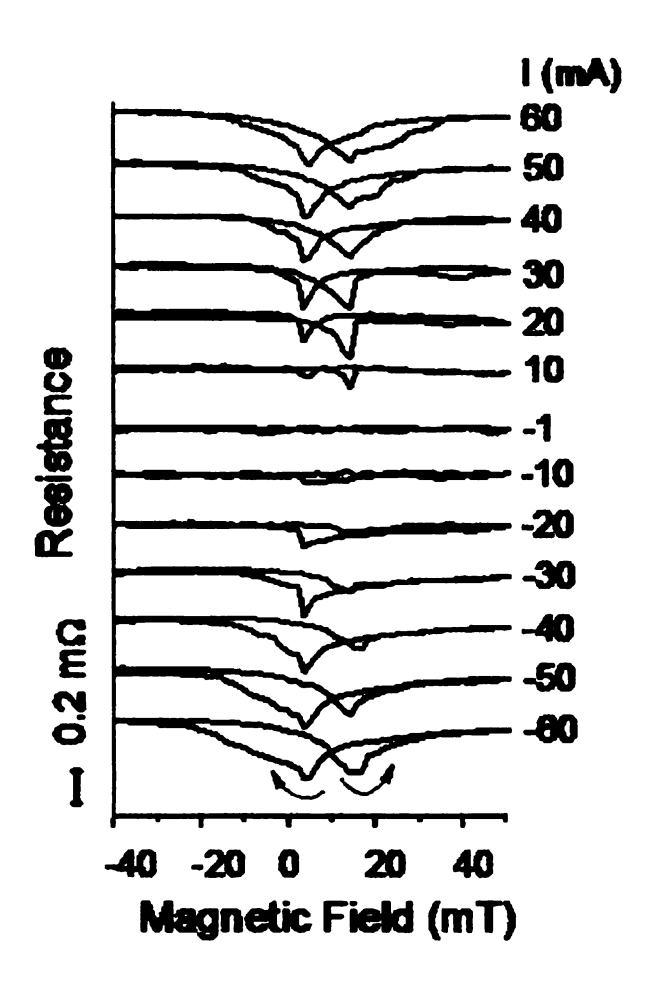


Figure 4.10: Point-contact magnetoresistance at different bias currents for a 1.3 Ohm point contact to sample CoFe(10)/ FeMn(8)/ Cu(10)/ FeMn(8)/ CoFe(3). All layer thicknesses are in nm. The solid traces show point-contact resistance versus applied magnetic field for a series of applied currents. The figure is from [19].

the results.

- We observed no MR for all of the samples at small applied currents.
- AFM/N/ AFM: We observed no MR for these samples.
- F/AFM/N/AFM: For t(F) = 3nm we saw no MR. For t(F) = 10nm, we usually saw positive MR - large resistance at saturation fields - above a critical applied current but no MR at small currents.

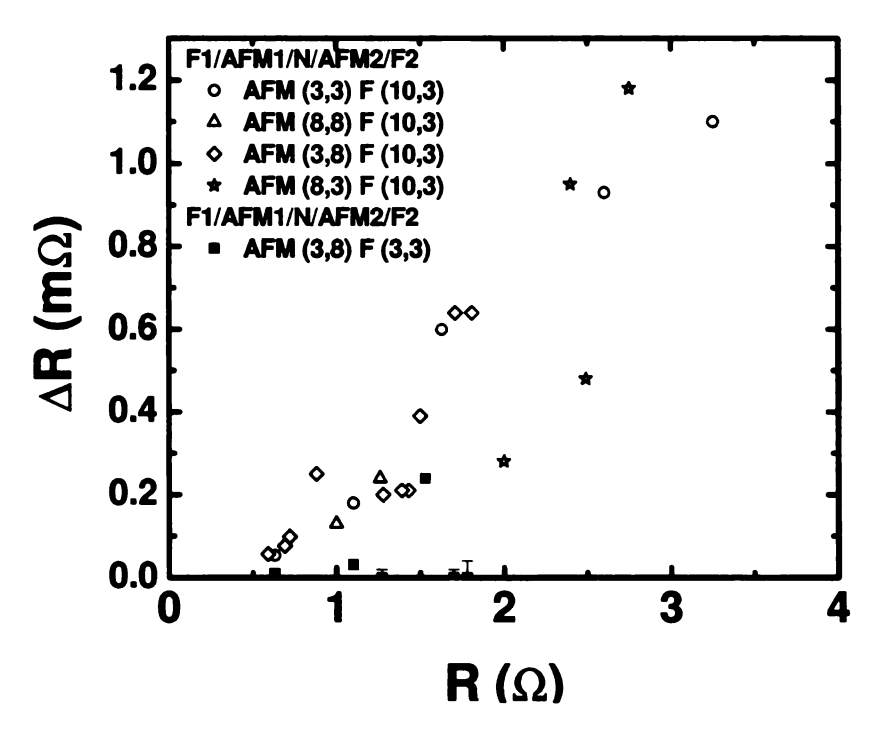


Figure 4.11: The maximum change in resistance, ΔR , vs. point contact resistance at I = 30 mA for down-sweeps. The open symbols show data for four different F1/AFM1/N/AFM2/F2 samples with $t(F_1) = 10$ nm, $t(F_2) = 3$ nm and t(AFM1, AFM2) = (3,3), (3,8), (8,3) and (8,8). All layer thicknesses in nm. F1 = F2 = CoFe and AFM = FeMn. The error bars are smaller than the symbol sizes. We also show, for comparison, data for F1/AFM1/N/AFM2/F2 samples with $t(F_1) = t(F_2) = 3$ nm (solid symbols). Note that the MRs for F1/F2 = 3/3 are much less than that for F1/F2 = 10/3. The figure is after [19].

- F/AFM/ N/AFM/F: For these samples, the results, discussed below, depend on the choice of F layer thickness.
 - 1. At least one t(F) = 10 nm: We usually found a positive MR - large resistance at saturation fields, above a critical applied current but no MR at small currents. The MR became larger in magnitude with increasing applied current but often saturated after certain value of current. We show an example of the positive MR data for an F(10)/AFM(8)/N/AFM(8)/F(3)

sample in figure 4.10. The sweeps in figure 4.10 represent the point-contact resistance vs. applied magnetic field at different applied currents. The minima in resistance for the sweeps figure 4.10 appear at ~ 5 mT for down sweeps (positive to negative fields) and at ~ 15 mT for up sweeps.

We observed similar MR effects in 28 other contacts to F1/AFM/N/AFM /F2 samples with $t(F_1)=10$ nm and $t(F_1)=3$ nm. We show the $\Delta R=R_{max}-R_{min}$ vs. R data for these point contacts (for down sweeps) at I=30 mA, in figure 4.11 as hollow symbols. The thicknesses of the two AFMs adjacent to F1 and F2 are denoted as 8/8, 3/3, 8/3, and 3/8 respectively and represented by different symbols as shown in the legend. We find that for the data shown in figure 4.11 (hollow symbols) ΔR increases with increasing contact resistance.

- t(F₁) = t(F₂) = 3 nm : The data for five of six contacts were very small. But one out of the six contacts gave a larger positive MR. Figure 4.11 shows these data as solid square symbols.
- AFM/F/N/AFM, N/F/AFM, and N/F/N samples: The data in figure 4.11 suggest that at least one 10nm thick ferromagnet is required to observe positive the MR effects. To test for this possibility we measured different sample structures with t(F) = 3 or 10 nm. These sample structures include AFM/F/N/AFM, N/F/AFM, N/F/N structures apart from single F layer sandwiched between Au, Cu, or AFM layers. We found that the samples with t(F) = 3 nm rarely gave MRs. In contrast, the samples with t(F) = 10 nm, (data

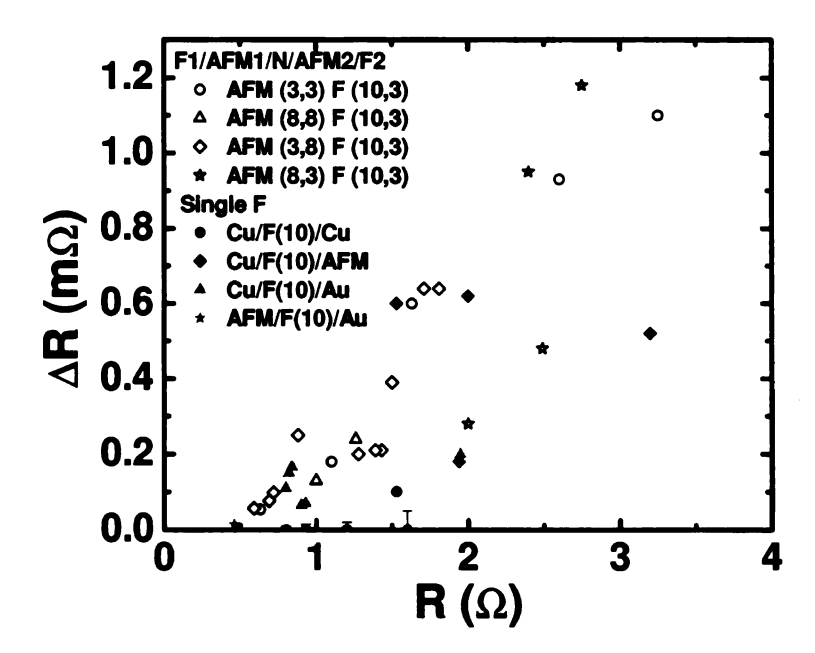


Figure 4.12: The maximum change in resistance, ΔR , vs. point contact resistance at I=30 mA for down-sweeps. The open symbols show same data as shown in figure 4.11. The filled symbols show data for samples with F (= CoFe) = 10 nm sandwiched between different metals, as shown in the legend. The error bars are smaller than the sizes of the symbols. The figure is from [19].

shown in figure 4.12 as solid symbols) generally gave positive MR. For comparison, figure 4.12 also shows the data for F1(10 nm)/AFM/N /AFM/F2(3nm) samples (hollow symbols)

4.5.1 Search for AGMR effects - - Analysis

The possibility of the observed positive MRs in F1/AFM/N/AFM/F2 samples being due to the two outer ferromagnets can be ruled out, as any such MR should be negative. The observed positive MR seems unlikely to be the AGMR as predicted by Nunez, Haney and coworkers [13, 14, 15, 16], since it never appeared with just AFMs alone, and almost required a 10nm thick F layer. The observation of MRs in samples

with at least one layer of t(F) = 10 nm suggests that the MR could possibly be related to the F layer as observed by Urazhdin et al [157] in Py nanodiscs. Urazhdin et al [157] explained their observations as due to the suppression by high currents of spin accumulation induced around and within the F-layer. At large magnetic fields, the magnetization of F is uniform and the pillar resistance is higher due to an extra contribution from spin accumulation. At low fields, the Oersted field induced vortex state suppresses the spin accumulation, decreasing the pillar resistance. Similar phenomenon might be responsible for the effects we see. The samples used by Urazhdin et al had a geometry preferring formation of vortices, which our extended samples do not have. Thus our results would be first such observation in extended samples.

4.6 Summary

We have done experiments to look for anti ferromagnetic spintronics effects predicted by Nunez, Haney and coworkers [13, 14, 15, 16]: (a) large current densities affecting exchange bias, and (b) antiferromagnetic GMR in AFM/N/AFM trilayers.

The first experiments were to study the effect of large current densities on exchange bias using mechanical point contacts on exchange bias spin valve samples. For F = CoFe, we found that the switching field of the fixed layer was affected by external applied currents. We observed both shifting and broadening of the fixed layer switching field. In contrast, the switching field of the free layer was not affected much. The effects were generally consistent for AFM = FeMn or IrMn with F = CoFe. We tentatively attributed the shifts in the switching field of the fixed layer (For F = CoFe) to spin transfer torque acting on bulk AFM domains. The bulk AFM domains

then affected the strongly coupled pinned F/AFM interfacial moments which caused the shifts in the fixed layer switching field. However we cannot rule out interface effects instead. Upon changing F from CoFe to Py, we found that the switching fields of both the fixed and free layers were affected. For Py, the spin transfer torque seems to act on both the free and the fixed layer. To get a clear picture of what might be going on with F = Py, more experiments are planned.

Our second set of experiments were to search for antiferromagnetic GMR effects in multilayers with AFMs. These studies were also done using mechanical point contacts on mixed multilayer samples. The samples for these studies had AFM = FeMn and F = CoFe. No MR was observed for these samples at small currents. We started with AFM/N/AFM samples but found no MR.

We then tested F/AFM/N/AFM samples with $t_F = 3$ nm and found no MR.

We then extended our studies to F/AFM/N/AFM/F samples and found small positive MR (largest resistance at saturation fields), at large currents, but for samples with at least one t(F) = 10 nm. In contrast, for F/AFM/N/AFM/F samples with both t(F) = 3 nm, we found positive MR only for one out of six contacts. The MRs thus appear to be sensitive to the thickness of the F layer.

To test this possibility, we studied samples with structures AFM/F/N/AFM, F/AFM/N/AFM, N/F/AFM, or N/F/N with F = 3 or 10 nm. We found that for F = 3 nm, none of the sample structures, gave any MR. However, the sample structures with F=10 nm usually gave small positive MRs. The source of the MR looks complicated. For F/AFM/N/AFM/F samples, the MR could not possibly be due to the two outer F-layers as any MR due to these Fs would be negative - - smallest resistance

at saturation fields. Positive MRs, similar to those we see, were previously shown by Urazhdin et al [157] to exist in Py nanodiscs. Their interpretation involved spin accumulation effects and vortex states. Their nano-disc sample geometry promoted formation of vortex states, which our extended layers do not have. Thus, if our results are due to such effects, it would be the first such observations in extended layers.

Chapter 5

Conclusions

In this thesis, I have done experiments to produce new information about three topics:

(a) current perpendicular to the plane magnetoresistance (CPP-MR) and (b) spin transfer torque (STT), both with ferromagnets (F), and (c) predicted spintronics effects with antiferromagnets (AFM).

CPP-MR studies

The CPP-MR experiments were done to determine interface parameters, both to search for metal pairs with a combination of large values of $2AR^*$ and γ (making them better suited for devices than standard metal pairs), and to compare our results with calculations. We used our standard CPP-MR technique to determine these interface parameters, combining multilayer and exchange biased spin valve samples.

Motivated by the Cornell group's Py/Al/Py nanopillar studies [81], we started our CPP-MR studies by determining the interface parameters of Py/Al. We found unusually large specific interface resistance, $2AR_{Py/Al}^* \sim 8.5 \text{ f}\Omega m^2$, but small asymmetry parameter, $\gamma \sim 0.025$. The large value of $2AR_{Py/Al}^*$ motivated us to extend our CPP-MR studies to other F = Co, Fe, & Co₉₁Fe₉, with Al, in the hopes of finding large values of both $2AR_{F/Al}^*$ and γ . We again found large values of $2AR_{F/Al}^* \sim 8.4$

- 11.6 f Ωm^2 but small $\gamma \leq 0.18$. We also found the resistance of the samples to be unstable with time and upon annealing, suggesting significant interdiffusion between F metals and Al, later confirmed by detailed structural studies. Still motivated by the large values of $2AR_{F/Al}^*$, we extended our CPP-MR studies to new N metals. We chose N metals with relatively large spin diffusion lengths compared to t_N , and paired each with an F metal with matching crystal structure. We studied Py/Pd, Fe/V, Fe/Nb and Co/Pt metal pairs. Except for Py/Pd, the interface parameters of these four new metal pairs fall between the values for standard Py/Cu and our recently determined ones for Co₉₁Fe₉/Al. None of the newly studied F/Al or F/N pairs looks competitive for devices.

The Cornell group additionally found that bracketing thick Al (\sim 10nm) with thin Cu (\sim 0.6 nm) gave an MR closer to Py/Al/Py than to Py/Cu/Py [82]. We initially thought that such thin Cu would be incorporated into the finite thickness F/Al interfaces, and thus play a minor role. To check our interpretation, we extended our CPP-MR experiments to study the effect of Cu(t_{Cu})/Al(t_{Al})/Cu(t_{Cu}) sandwiches on the A Δ R of Py based exchange biased spin valves(EBSV). For fixed t_{Al} =10nm, A Δ R was small and independent of t_{Cu}, but fixing t_{Cu} = 10 nm and increasing t_{Al} caused a significant drop in A Δ R to the small value for fixed t_{Al} = 10nm. Our independently determined 2AR_{Al/Cu} = 2.2 ± 0.2 f Ω m² was not large enough to explain the observed behavior. Diffusion distance calculations predicted strong interdiffusion between Al and Cu, later confirmed by our collaborative structural studies. The strong interdiffusion appears to be the cause of the observed unusual behavior of the the A Δ R but a detailed explanation is not yet clear.

We also determined $2AR_{Al/Ag}$ to compare with calculations predicting a strong dependence on orientation as well as on alloying. Our estimates of $2AR_{Al/Ag}$ (111) = $1.4 \pm 0.2 \ f\Omega m^2$ agree with the calculations if we include 4 monolayers of disorder - $2AR_{Al/Ag}$ (111) (calc) = $1.31 \ f\Omega m^2$ [96]. We also found that the sample resistances of Al/Ag multilayers increase with time, suggesting continuing interdiffusion between Al and Ag.

STT studies

To help us understand the underlying physics of spin transfer torque in F/N/F trilayers we have done experiments where we change only the transport in the N layer from ballistic to diffusive. To minimize systematic errors, we compared the ratios of our experimental estimates with calculations.

One of the ratios - - Δ I(Diffusive)/ Δ I(Ballistic), where Δ I is the difference between the positive and negative switching currents, I_c^+ and I_c^- - - agrees with only the ballistic Slonczewski model, which is surprising as this model cannot correctly describe our samples, which involve diffusive scattering. Otherwise our ratios disagree with standard models expected to be more reliable.

AFM studies

Based on the predictions of Nunez, Haney and coworkers [13, 14, 15, 16], we have done experiments to: (a) study the effect of large current densities on exchange bias between an F and an AFM metal, and (b) to look for antiferromagnetic GMR in AFM/N/AFM trilayers.

We first studied the effect of large current densities on exchange bias using mechanical point contacts to exchange biased spin valves consisting of one free F layer and one F layer pinned by an adjacent AFM layer. We initially started with F = CoFe and AFM = FeMn. The switching field of the free CoFe layer was not affected by current. In contrast, the switching field of the fixed CoFe layer both shifted and broadened with current. Changing the pinning AFM from FeMn to IrMn, but keeping F = CoFe, gave similar results. In contrast, for both AFM = FeMn and IrMn, changing F from CoFe to Py gave more complex shifts in the switching fields of both the fixed and free layers.

We then extended our experiments to search for antiferromagnetic GMR effects. The samples for these studies had AFM = FeMn and F = CoFe. We initially started with AFM/N/AFM samples but found no MR. We then tested F/AFM/N/AFM samples with $t_F = 3$ nm and again found no MR. We then extended our studies to F/AFM/N/AFM/F samples and found positive MR (largest resistance at saturation fields) for samples with at least one t(F) = 10 nm, at large currents. Samples having both t(F) = 3 nm gave positive MR for only one out of six contacts. The thicknesses of the F layers thus seem to affect MR. To test this possibility, we extended our studies to samples with structures AFM/F/N/AFM, F/AFM/N/AFM, N/F/AFM, or N/F/N with F = 3 or 10 nm. For t(F) = 3 nm, usually the sample gave no MR. In contrast, the samples with F=10 nm usually gave positive MRs.

Our studies show effects of large current densities on the exchange bias, and some evidence of positive MR in mixed multilayer samples. However, the observed positive MR cannot be directly attributed to antiferromagnetic GMR, which is thus yet to be observed.

APPENDIX

Appendix A

A.1 Van der Pauw resistivity measurement.

We generally measure the resistivities of our metals using the Van der Pauw technique [55] on ~ 200 nm thick sputtered films. Such a thick film (~ 200 nm) is much larger than the mean free path, making the contributions from surface scattering small. The Van der Pauw technique has the advantage of allowing measurement of the resistivity of any uniform thin metal or alloy of arbitrary shape, but without holes.

This technique gives us sheet resistance - - ρ /t, where t is the thickness of the film. For our samples, t is known within \pm 5%. For our sputtered films, grown with the same target, we generally get ρ within \pm 10%.

We measure the resistivity at room temperature as well as at 4.2 K, so that we can check for consistency of the difference between the room temperature and 4.2 K resistivities with the known phonon resistivity of the bulk metal [95]. The samples are mounted on a quick dipper - - a stick with connecting leads. The leads are connected to the outer corners of the sputtered region, using Indium, as shown in figure A.1. The samples are first measured at room temperature, and then at 4.2 K by slowly dipping the quick dipper into a liquid helium dewar. A Lakeshore current source is used to apply currents and the voltages are measured with a Keithley nanovoltmeter.

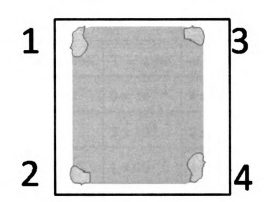


Figure A.1: A schematic drawing of a film used to do Van der Pauw resistivity measurement. The shaded central region is the sputtered film. The small irregular regions on the edges represent the Indium contacts.

The measurements are done for several currents < 30 mA (we use small currents to avoid Joule heating) to check for current independence of the resistance. To eliminate thermoelectric effects, and also the voltage offset of the nanovoltmeter, each measurement is done for both polarities of the currents.

For a measurement, the current I_1 is first sent through two neighboring leads (e.g., 1 and 2 in figure A.1) and the voltage V_1 is measured across the other two neighboring leads (3 and 4). The current I_2 is then sent through a different set of neighboring leads (e.g., 1 and 3 in figure A.1) and the voltage V_2 measured across the other two leads (2 and 4). The resistances $R_1 = V_1/I_1$ and $R_2 = V_2/I_2$ are then calculated and the resistivity is determined using the equation

$$\rho = \frac{\pi t}{ln(2)} \frac{(R_1 + R_2)}{2} f \tag{A.1}$$

where t is the thickness of the film and f is a factor depending on the ratio R1/R2 given in [55].

Metal 1 in 2	d (nm) in 1 min		d (nm) in 1 week	
	at T = 300K	T = 450K	at T = 300K	T = 450K
Al in Cu	4×10^{-9}	9×10^{-4}	4×10^{-7}	9×10^{-2}
Cu in Al	2 x 10 ⁻⁴	2×10^0	2 x 10 ⁻²	2×10^2
Al in Ni	4×10^{-15}	1×10^{-7}	4×10^{-13}	1×10^{-5}
Ni in Al	7×10^{-5}	1 x 10 ⁰	7×10^{-3}	1×10^2
Al in Fe	3×10^{-12}	1×10^{-5}	3×10^{-10}	1×10^{-3}
Fe in Al	8×10^{-8}	2×10^{-2}	8 x 10 ⁻⁶	2 x 10 ⁰
Co in Al	2×10^{-6}	2 x 10 ⁻¹	2×10^{-4}	2×10^1
Al in Ag	7×10^{-7}	3×10^{-2}	7×10^{-5}	3×10^0
Ag in Al	3×10^{-3}	9 x 10 ⁰	3×10^{-1}	9×10^2
Al in Au	1×10^{-5}	2 x 10 ⁻¹	1×10^{-3}	2×10^{1}
Au in Al	4×10^{-3}	1 x 10 ¹	4×10^{-1}	1 x 10 ³

Table A.1: Our estimates of diffusion distances d(nm) for t=1 min and t=1 week at both 300 K and 450 K for dilute concentrations of various metals in Al and vice versa.

A.2 Estimates of diffusion distances of various metals in Al and vice-versa

The diffusion distances of various metals in Al, and of Al in those metals, were calculated for t=1 min and t=1 week at both 300K and at 450 K - - the temperature at which the exchange biased spin valve samples are pinned.

To determine these diffusion distances, we first estimate the diffusion constants D(T) for bulk motion of the metals of interest into Al, and vice versa, at the temper-

atures of present interest - - 300 and 450 K. As the data for such interdiffusion have been taken only at much higher temperatures [158], and only for dilute concentrations of the diffusing atoms, we have to extrapolate the coefficients from these higher temperatures to 300 K and 450 K, and assume that the resulting coefficients can be used for our samples where the concentrations for interdiffusion are not dilute. Moreover, our sputtered multilayers grow as columnar polycrystals, with columns \sim 20-40 nm in diameter (see section IV in [94]). At our lower temperatures, mass transport might be dominated by diffusion along the column boundaries. Our estimates of bulk diffusion are, thus, likely to be only lower bounds on the actual diffusion rates.

We assume the standard Arrhenius form $D(T)=D_o\exp(-Q/kT)$ where D_o is the prefactor in units of m/s², Q is the activation enthalpy for diffusion in eV/atom, k is Boltzmann's constant, and T is the absolute temperature. To estimate the distances that each metal can diffuse into the other, we use the standard one-dimensional diffusion equation

$$d = \sqrt{4D_0 texp(-Q/kT)} \tag{A.2}$$

where t is the diffusion time.

We list our estimated values of d for t=1 min and t=1 week in table A.1, where we have listed the linear average of the resulting values of d for metal pairs with more than one pair of D_0 and Q as given in [158]. We have listed d to only one significant figure due to typical variations in these values and uncertainties in the extrapolations, The uncertainty in each d should be at least a factor of two. The distance diffused in one year can be estimated by multiplying the listed value for 1 min by 0.73×10^3 .

The data in table A.1 show that Ag and Au should diffuse a few monolayers in Al

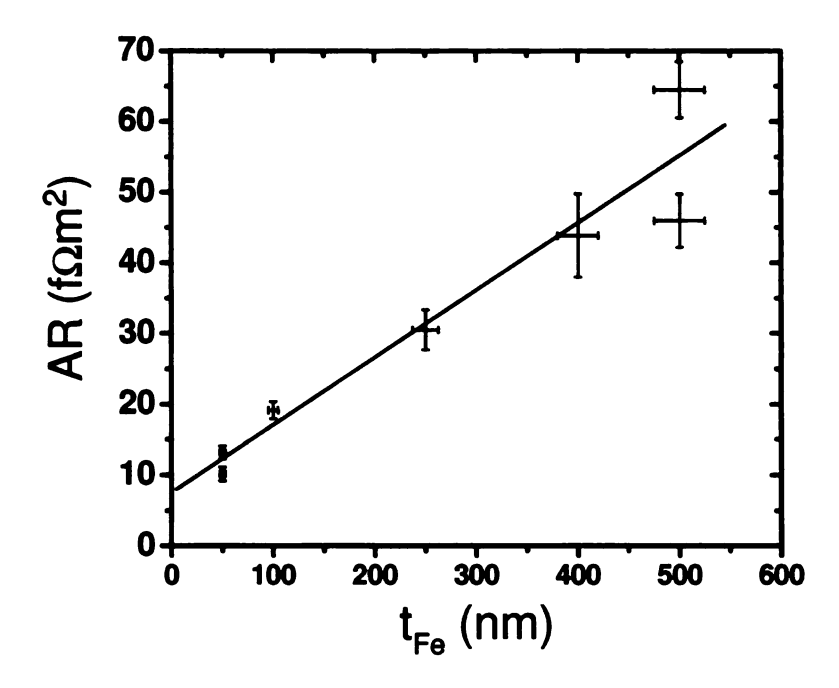


Figure A.2: AR versus t_{Fe} plot for Nb(150nm)/ Fe(t_{Fe})/Nb(150 nm) multilayers. The slope of the best-fit straight line gives $\rho_{Fe}=95\pm6$ n Ω m and the intercept gives $2AR_{Nb/Fe}=7.6\pm0.8$ f Ωm^2 . The value of the intercept agrees with the prior estimates of Bozec et al [54] and Zambano et al [53]. The figure is from [104].

in 1 week at 300 K, and tens of nm at 450 K. Cu in Al diffuses a fraction of an Å in a week at 300 K but tens of nm at 450 K. In a week, Ni, Co and Fe have small diffusion in Al at 300 K but strong diffusion at 450 K. Except for Ag and Au, the diffusion of Al in other metals is pretty small at both 300 K and 450 K. But in concentrated systems, diffusion of N into Al probably leads to diffusion of Al into N.

A.3 Estimating $2AR_{Nb/Fe}$ and ρ_{Fe} by the CPP technique

To estimate ρ_{Fe} by the CPP technique, we use samples with the structure Nb(150nm) /Fe(t_{Fe})/ Nb(150nm) and determine ρ_{Fe} from a plot of AR vs t_{Fe} as shown in figure

A.2. The slope of the best fit straight line in figure A.2 gives $\rho_{Fe}=95\pm6$ n Ω m and the intercept gives $2AR_{Nb/Fe}=7.6\pm0.8$ f Ωm^2 . The previous estimates of $2AR_{Nb/Fe}=7.2\pm0.5$ f Ωm^2 by Bozec et al [54] and $2AR_{Nb/Fe}=6\pm1$ f Ωm^2 [53] by Zambano et al, were both for $\rho_{Fe}\sim40$ n Ω m. Our estimate of $2AR_{Nb/Fe}$ thus agrees, within mutual uncertainties, with the earlier estimates, but our ρ_{Fe} is much larger than previous values. For simplicity, we use $2AR_{Nb/Fe}=6\pm1$ f Ωm^2 in our analysis.

A.4 Recipe for optical lithography

- 1. Spin photo resist S1805 on the substrate for 40 secs at 4000 RPM.
- 2. Bake at 95° C on a hot plate for 60 mins.
- 3. Stabilize the UV lamp by turning it on for ~ 20 mins before exposing the sample.
- 4. Check the UV lamp intensity by a intensity meter. Reference values are 13 mW/cm² and 19 mW/cm² for the A and the B channels respectively.
- 5. Place the baked wafer and then the photo-mask, which contains the lithography pattern, on the mask aligner. The photo-mask is carefully aligned with the wafer. The photo mask and the wafer are carefully brought into contact by using a set of vacuum systems.
- 6. The photo mask + wafer is exposed to the UV light for 2.5 secs.

- 7. After the exposure, the UV lamp is first brought to stand-by position. The photo-mask and the wafer are removed and the UV lamp turned off.
- 8. The exposed substrate is dipped in chlorobenzene for ~20 secs and then cleaned with plenty of running de-ionized (DI) water and blow dried by compressed air.
- 9. The processed substrate is then dipped in photo-developer 452 till the exposed pattern slowly appears (~ 50 secs).
- 10. The developed wafer is then cleaned with plenty of running DI water.
- 11. The wafer is then blow dried by compressed air and inspected with the optical microscope with the UV filter ON.

A.5 Recipe for e-beam lithography

- For e-beam lithography, a bi-layer e-beam resist structure is used to get a better undercut for liftoff. The bilayer resists are spun at 4000 RPM for all the e-beam lithography steps except for the nano-pillar e-beam lithography step for which the resists are spun at 6000 RPM.
- 2. Spin first layer of e-beam resist - MMA (9 % ethyl lactate) for 40 secs.
- 3. Bake at 170° on a hot plate for 5 mins to dry the resist.
- Spin second layer of e-beam resist - PMMA (2 % chlorobenzene) on top of first layer of e-beam resist.
- 5. Bake at 170° on a hot plate for 30 mins to dry the resist and get rid of any moisture.

- 6. Stabilize the electron microscope magnetic lens for \sim 60 mins, by turning down the magnification to 20X.
- 7. Load the substrates in the chamber of the electron microscope through the load lock and wait till a vacuum 2×10^{-7} of torr is achieved.
- 8. Design a pattern to be written using the DesignCad software.
- 9. Slowly saturate the filament till the second intensity peak is observed.
- 10. Slowly ramp up the beam current to the desired value
- 11. Wait for \sim 20 mins to stabilize the filament and beam currents.
- 12. Set the dose at which the pattern needs to be written. Generally, our patterns are composed of a inner region and an outer slightly larger region, with both patterns written one after the other. The inner region is thus exposed twice. The typical values of area doses are ~ 150 μC/cm² for the inner region and ~ 90 μC/cm². However, to determine correct dose, a dose test is recommended. In the dose test, many copies of a pattern are written at different doses and developed by e-beam developer. Then some metal is evaporated into these patters and checked on electron microscope to determine which dose works best.
- 13. Correct the beam for astigmatism using some convenient defect.
- 14. Turn on the beam blanker and enable external scan

- 15. Align the substrate using the alignment marks at the respective magnifications they are designed for.
- 16. Write the pattern using the nano-pattern generation system (NPGS).
- 17. Turn off the beam blanker and disable external scan. Turn down the beam current slowly and then turn down the filament current slowly.
- 18. Take out the wafer through the load lock.
- 19. Develop the wafer in e-beam developer-MIBK:IPA (1:3) for \sim 30 secs and then immediately dip in IPA for \sim 10 secs and blow dry.
- 20. Inspect the wafer with an optical microscope using the Normarski differential interference contrast feature with the polarizer.

BIBLIOGRAPHY

Bibliography

- [1] For coining of the term 'Spintronics' see IBM Journal of Res. & Dev. 50, 101 (2006).
- [2] I. A. Campbell and A. Fert, in *Ferromagnetic Materials*, edited by E. P. Wolfarth (North-Holland, Amsterdam, 1982), Vol. 3, p. 747.
- [3] M. Johnson and R. H. Silsbee, Phys. Rev. Lett. **55**, 1790 (1985).
- [4] R. Meservey, D. Paraskevopoulos, and P. M. Tedrow, Phys. Rev. Lett. 37, 858 (1976).
- [5] M. N. Baibich, J. M. Broto, A.Fert, F. N. V. Dau, and F. Petroff, Phys. Rev. Lett. 61, 2472 (1988).
- [6] G. Binasch, P. Grunberg, F. Saurenbach, and W. Zinn, Phys. Rev. B 39, 4828 (1989).
- [7] http://nobelprize.org/.
- [8] J. C. Slonczewski, J. Magn. Magn. Mater. 159, L1 (1996).
- [9] L. Berger, Phys. Rev. B **54**, 9353 (1996).
- [10] M. Tsoi, A. G. M. Jensen, J. Bass, W. C. Chiang, M. Seck, V. Tsoi, and P. Wyder, Phys. Rev. Lett. 80, 4281 (1998).
- [11] E. B. Myers, D. C. Ralph, J. A. Katine, R. N. Louie, and R. A. Buhrman, Science 285, 867 (1999).
- [12] J. A. Katine, F. J. Albert, R. A. Buhrman, E. B. Myers, and D. C. Ralph, Phys. Rev. Lett. 84, 3149 (2000).
- [13] A. S. Nunez, R. A. Duine, P. M. Haney, and A. H. MacDonald, Phys. Rev. B 73, 214426 (2006).
- [14] P. M. Haney and A. H. MacDonald, arXiv:0708.3231 (2007).
- [15] P. M. Haney, Ph.D. thesis, The University of Texas at Austin, 2007.
- [16] P. M. Haney, D. Waldron, R. A. Duine, A. S. Nunez, H. Guo, and A. H. MacDonald, Phys. Rev. B 75, 174428 (2007).

- [17] Z. Wei, A. Sharma, A. S. Nunez, P. M. Haney, R. A. Duine, J. Bass, A. H. MacDonald, and M. Tsoi, Phys. Rev. Lett. 98, 116603 (2007).
- [18] J. Basset, A. Sharma, Z. Wei, J. Bass3, and M. Tsoi, SPIE **7036**, 703605 (2008).
- [19] Z. Wei, A. Sharma, J. Bass, and M. Tsoi, J. Appl. Phys. (In Press).
- [20] S. Urazhdin and N. Anthony, Phys. Rev. Lett. 99, 046602 (2007).
- [21] X. L. Tang, H.-W. Zhang, H. Su, Z.-Y. Zhong, and Y.-L. Jing, Appl. Phys. Lett. 91, 122504 (2007).
- [22] D. N. H. Nam, N. C. Thuan, L. V. Hong, N. X. Phuc, S. A. Wolf, N. V. Dai, and Y. P. Lee, arxiv:0801.1515 (2008).
- [23] W. Thomson, Proceedings of the Royal Society of London 8, 546 (1856).
- [24] N. W. Ashcroft and N. D. Mermin, Solid State Physics (Harcourt Brace College Publishers, Fort Worth, 1976).
- [25] N. F. Mott, Proceedings of the Royal Society of London. Series A, Mathematical and Physical Sciences 153, 699 (1936).
- [26] J. Stöhr and H. C. . Siegmann, in Magnetism: From Fundamentals to Nanoscale Dynamics, edited by M. Cardona, P. Fulde, K. Klitzing, R. Merlin, H. J. Queisser, and H. Störmer (Springer series in Solid State Sciences (152), New York, 2006).
- [27] P. Grünberg, R. Schreiber, Y. Pang, M. B. Brodsky, and H. Sowers, Phys. Rev. Lett. 57, 2442 (1986).
- [28] P. Grünberg, R. Schreiber, Y. Pang, U. Walz, M. B. Brodsky, and H. Sowers, J. Appl. Phys. 61, 3750 (1987).
- [29] http://www.research.ibm.com/research/gmr.html.
- [30] W. P. Pratt, Jr., S. F. Lee, J. M. Slaughter, R. Loloee, P. A. Schroeder, and J. Bass, Phys. Rev. Lett. 66, 3060 (1991).
- [31] S. Zhang and P. M. Levy, J. Appl. Phys. 69, 4786 (1991).
- [32] J. Bass and W. P. Pratt, Jr., J. Magn. Magn. Mater. 200, 274 (1999).
- [33] T. Valet and A. Fert, Phys. Rev. B 48, 7099 (1993).
- [34] S. F. Lee, W. P. Pratt, Jr., Q. Yang, P. Holody, R. Loloee, P. A. Schroeder, and J. Bass, J. Magn. Magn. Mater. 118, L1 (1993).
- [35] P. M. Levy, in *Solid State Physics*, edited by H. Ehrenreich and D. Turnbull (Academic Press, Cambridge MA, 1994), Vol. 47, Chap. Giant magnetoresistance in magnetic layered and granular materials, pp. 367–462.

- [36] M. A. M. Gijs and G. E. W. Bauer, Adv. in Phys. 46, 285 (1997).
- [37] E. Tsymbal and D. Pettifor, in *Solid State Physics* (Academic Press, San Diego, 2001), Vol. 56, p. 113.
- [38] A. Fert and L. Piraux, J. Magn. Magn. Mater. 200, 338 (1999).
- [39] J. Childress, M. Carey, S. Maat, N. Smith, R. Fontana, D. Druist, K. Carey, J. Katine, N. Robertson, T. Boone, M. Alex, J. Moore, and C. Tsang, IEEE Trans. Magn. 44, 90 (2008).
- [40] S. S. P. Parkin, N. More, and K. P. Roche, Phys. Rev. Lett. 64, 2304 (1990).
- [41] S. S. P. Parkin, R. Bhadra, and K. P. Roche, Phys. Rev. Lett. 66, 2152 (1991).
- [42] J. A. Borchers, J. A. Dura, J. Unguris, D. Tulchinsky, M. H. Kelley, C. F. Majkrzak, S. Y. Hsu, R. Loloee, W. P. Pratt, and J. Bass, Phys. Rev. Lett. 82, 2796 (1999).
- [43] P. Holody, W. C. Chiang, R. Loloee, J. Bass, W. P. Pratt, and P. A. Schroeder, Phys. Rev. B 58, 12230 (1998).
- [44] B. Dieny, V. S. Speriosu, S. Metin, S. S. P. Parkin, B. A. Gurney, P. Baumgart, and D. R. Wilhoit, J. Appl. Phys. 69, 4774 (1991).
- [45] J. Bass and W. P. Pratt, Jr., J. Phys.: Condensed Matter 19, 183201 (2007).
- [46] W. Park, D. Baxter, S. Steenwyk, I. Moraru, W. P. Pratt, Jr., and J. Bass, Phys. Rev. B 62, 1178 (2000).
- [47] J. Y. Gu, J. A. Caballero, R. D. Slater, R. Loloee, and W. P. Pratt, Phys. Rev. B 66, 140507 (2002).
- [48] S. K. Olson, R. Loloee, N. Theodoropoulou, J. W. P. Pratt, J. Bass, P. X. Xu, and K. Xia, Appl. Phys. Lett. 87, 252508 (2005).
- [49] W. P. Pratt, Jr., S. D. Steenwyk, S. Y. Hsu, W.-C. Chiang, A. C. Schaefer, R. Loloee, and J. Bass, IEEE Trans. Magn. 33, 3505 (1997).
- [50] S. D. Steenwyk, S. Y. Hsu, R. Loloee, J. Bass, and W. P. Pratt, Jr., J. Magn. Magn. Mater. 170, L1 (1997).
- [51] L. Piraux, S. Dubois, A. Fert, and L. Belliard, Eur. Phys. J. B 4, 413 (1998).
- [52] A. C. Reilly, W. Park, R. Slater, B. Ouaglal, R. Loloee, W. P. Pratt, Jr., and J. Bass, J. Magn. Magn. Mater. 195, 269 (1999).
- [53] A. Zambano, K. Eid, R. Loloee, W. P. Pratt, Jr., and J. Bass, J. Magn. Magn. Mater. 253, 51 (2002).
- [54] D. Bozec, Ph.D. thesis, Leeds University, Leeds, UK, 2000.

- [55] L. J. van der Pauw, Philips Tech. Rev. 20, 220 (1958).
- [56] W. Park, R. Loloee, J. A. Caballero, W. P. Pratt, Jr., P. A. Schroeder, J. Bass, A. Fert, and C. Vouille, J. Appl. Phys. 85, 4542 (1999).
- [57] L. Vila, W. Park, J. A. Caballero, D. Bozec, R. Loloee, J. W. P. Pratt, and J. Bass, J. Appl. Phys. 87, 8610 (2000).
- [58] J. Bass and W. P. Pratt, Jr., Physica B 321, 1 (2002).
- [59] C. Galinon, K. Tewolde, R. Loloee, W.-C. Chiang, S. Olson, H. Kurt, W. P. Pratt, Jr., J. Bass, P. X. Xu, K. Xia, and M. Talanana, Appl. Phys. Lett. 86, 182502 (2005).
- [60] P. X. Xu, K. Xia, M. Zwierzycki, M. Talanana, and P. J. Kelly, Phys. Rev. Lett. 96, 176602 (2006).
- [61] G. E. W. Bauer, Phys. Rev. Lett. **69**, 1676 (1992).
- [62] H. E. Camblong, S. Zhang, and P. M. Levy, Phys. Rev. B 47, 4735 (1993).
- [63] K. M. Schep, J. B. A. N. van Hoof, P. J. Kelly, G. E. W. Bauer, and J. E. Inglesfield, Phys. Rev. B 56, 10805 (1997).
- [64] K. Schep, J. van Hoof, P. Kelly, G. Bauer, and J. Inglesfield, J. Magn. Magn. Mater. 177-181, 1166 (1998).
- [65] M. D. Stiles and D. R. Penn, Phys. Rev. B 61, 3200 (2000).
- [66] K. Xia, P. J. Kelly, G. E. W. Bauer, I. Turek, J. Kudrnovský, and V. Drchal, Phys. Rev. B 63, 064407 (2001).
- [67] M. Tsoi, A. G. M. Jansen, J. Bass, W.-C. Chiang, M. Seck, V. Tsoi, and P. Wyder, Phys. Rev. Lett. 81, 493 (1998).
- [68] J. Z. Sun, J. Magn. Magn. Mater. **202**, 157 (1999).
- [69] M. Tsoi, A. G. M. Jansen, J. Bass, W.-C. Chiang, V. Tsoi, and P. Wyder, Nature 406, 46 (2000).
- [70] S. I. Kiselev, J. C. Sankey, I. N. Krivorotov, N. C. E. R. J. Schoelkopf, R. A. Buhrman, and D. C. Ralph, Nature 425, 380 (2003).
- [71] W. H. Rippard, M. R. Pufall, S. Kaka, S. E. Russek, and T. J. Silva, Phys. Rev. Lett. 92, 027201 (2004).
- [72] I. N. Krivorotov, N. C. Emley, J. Sankey, S. I. Kiselev, D. C. Ralph, and R. A. Buhrman, Science 307, 228 (2005).
- [73] C. Heide, P. E. Zilberman, and R. J. Elliott, Phys. Rev. B 63, 064424 (2001).

- [74] C. Heide, Phys. Rev. Lett. 87, 197201 (2001).
- [75] C. Heide, Phys. Rev. B **65**, 054401 (2001).
- [76] M. L. Polianski and P. W. Brouwer, Phys. Rev. Lett. 92, 026602 (2004).
- [77] M. D. Stiles, J. Xiao, and A. Zangwill, Phys. Rev. B 69, 054408 (2004).
- [78] Y. Ji, C. L. Chien, and M. D. Stiles, Phys. Rev. Lett. 90, 106601 (2003).
- [79] B. Ozyilmaz, A. D. Kent, J. Z. Sun, M. J. Rooks, and R. H. Koch, Phys. Rev. Lett. 93, 176604 (2004).
- [80] see for example http://www.grandisinc.com/.
- [81] A. G. F. Garcia, I. N. Krivorotov, P. M. Braganca, D. C. Ralph, and R. A. Buhrman, Bull. Am. Phys. Soc. 50, (2005).
- [82] Prof. R. Buhrman (Private Communication).
- [83] J. M. Slaughter, W. P. Pratt, Jr., and P. A. Schroeder, Rev. Sci. Instrum. 60, 127 (1989).
- [84] S. F. Lee, Ph.D. thesis, Michigan State University, 1994.
- [85] S. F. Lee, Q. Yang, P. Holody, R. Loloee, J. H. Hetherington, S. Mahmood, B. Ikegami, K. Vigen, L. L. Henry, P. A. Schroeder, W. P. Pratt, Jr., and J. Bass, Phys. Rev. B 52, 15426 (1995).
- [86] P. R. J. Holody, Ph.D. thesis, Michigan State University, 1996.
- [87] K. F. Eid, Ph.D. thesis, Michigan State University, 2002.
- [88] H. Kurt, Ph.D. thesis, Michigan State University, 2005.
- [89] C. Fierz, S. F. Lee, J. Bass, W. P. Pratt, and P. A. Schroeder, J. Phys.: Condensed Matter 2, 9701 (1990).
- [90] W. P. Pratt, Jr., Q. Yang, L. L. Henry, P. Holody, W.-C. Chiang, P. A. Schroeder, and J. Bass, J. Appl. Phys. 79, 5811 (1996).
- [91] D. L. Edmunds, J. W. P. Pratt, and J. A. Rowlands, Rev. Sci. Instrum. 51, 1516 (1980).
- [92] A. Fert, J. L. Duvail, and T. Valet, Phys. Rev. B 52, 6513 (1995).
- [93] A. Fert and S. F. Lee, Phys. Rev. B **53**, 6554 (1996).
- [94] A. Sharma, N. Theodoropoulou, T. Haillard, R. Acharyya, R. Loloee, J. W. P. Pratt, J. Bass, J. Zhang, and M. A. Crimp, Phys. Rev. B 77, 224438 (2008).

- [95] J. Bass, in Metals: Electronic Transport Phenomena, Vol. 15a of Landolt-Bornstein New Series Group III, edited by K. H. Hellwege and J. L. Olsen (Springer, Berlin, 1982).
- [96] Dr. S. Wang and Dr. K. Xia (Private communication).
- [97] W. C. Chiang, Q. Yang, J. W. P. Pratt, R. Loloee, and J. Bass, The 41st annual conference on magnetism and magnetic materials 81, 4570 (1997).
- [98] B. C. Gundrum, D. G. Cahill, and R. S. Averback, Phys. Rev. B 72, 245426 (2005).
- [99] P. Schroeder, P. Holody, S. Lee, R. Loloee, W. P. Jr., and J. Bass, MRS Symposium Proc. 313, 47 (1993).
- [100] N. Theodoropoulou, A. Sharma, R. Loloee, J. W. P. Pratt, J. Bass, A. Fert, and H. Jaffres, J. Appl. Phys. 99, 08G502 (2006).
- [101] N. Theodoropoulou, A. Sharma, T. Haillard, R. Loloee, W. Pratt, J. Bass, J. Zhang, and M. Crimp, IEEE Trans. Magn. 43, 2860 (2007).
- [102] J. Zhang, M. Crimp, N. Theodoropoulou, A. Sharma, R. Loloee, W. P. Jr., and J. Bass, Mater. Res. Soc. Symp. Proc. 998, 0998 (2007).
- [103] J. Zhang, Ph.D. thesis, Michigan State University, 2007.
- [104] A. Sharma, J. A. Romero, N. Theodoropoulou, R. Loloee, J. W. P. Pratt, and J. Bass, J. Appl. Phys. 102, 113916 (2007).
- [105] S. S. Yan, Y. h. Liu, and L.-m. Mei, Phys. Rev. B 52, 1107 (1995).
- [106] J. W. Knepper and F. Y. Yang, Phys. Rev. B 71, 224403 (2005).
- [107] H. Kurt (unpublished).
- [108] T. Mühge, N. N. Garif'yanov, Y. V. Goryunov, G. G. Khaliullin, L. R. Tagirov, K. Westerholt, I. A. Garifullin, and H. Zabel, Phys. Rev. Lett. 77, 1857 (1996).
- [109] T. Mühge, K. Westerholt, H. Zabel, N. N. Garif'yanov, Y. V. Goryunov, I. A. Garifullin, and G. G. Khaliullin, Phys. Rev. B 55, 8945 (1997).
- [110] N. Theodoropoulou, A. Sharma, J. W. P. Pratt, J. Bass, M. D. Stiles, and J. Xiao, Phys. Rev. B 76, 220408 (2007).
- [111] N. Theodoropoulou, A. Sharma, J. W. P. Pratt, J. Bass, M. D. Stiles, and J. Xiao, J. Appl. Phys. 103, 07A705 (2008).
- [112] L. Landau and E. Lifshitz, Physik, Z. Sowjetunion 8, 153 (1935).
- [113] J. W. F. Brown, Micromagnetics (Interscience, New York, 1963).

- [114] M. D. Stiles and J. Miltat, in Spin dynamics in confined structures III, Topics in Applied Physics 101, edited by B. Hillebrands and A. Thiaville (Springer, NY, 2006), pp. 225-308.
- [115] D. C. Ralph and R. A. Buhrman, in *Concepts in spin electronics, Series on semiconductor science and technology*, edited by S. Maekawa (Oxford science publications, New york, 2006), pp. 195–238.
- [116] D. Ralph and M. Stiles, J. Magn. Magn. Mater. 320, 1190 (2008).
- [117] L. Berger, J. Appl. Phys. 89, 5521 (2001).
- [118] L. Berger, J. Appl. Phys. **93**, 7693 (2003).
- [119] M. D. Stiles and A. Zangwill, Phys. Rev. B 66, 014407 (2002).
- [120] F. J. Albert, N. C. Emley, E. B. Myers, D. C. Ralph, and R. A. Buhrman, Phys. Rev. Lett. 89, 226802 (2002).
- [121] L. Berger, J. Appl. Phys. **91**, 6795 (2002).
- [122] S. Zhang, P. M. Levy, and A. Fert, Phys. Rev. Lett. 88, 236601 (2002).
- [123] A. Shpiro, P. M. Levy, and S. Zhang, Phys. Rev. B 67, 104430 (2003).
- [124] J. E. Wegrowe, D. Kelly, Y. Jaccard, P. Guittienne, and J.-P. Ansermet, EPL (Europhysics Letters) 45, 626 (1999).
- [125] J. E. Wegrowe, X. Hoffer, P. Guittienne, A. Fbin, L. Gravier, T. Wade, and J.-P. Ansermet, J. Appl. Phys. 91, 6806 (2002).
- [126] E. B. Myers, F. J. Albert, J. C. Sankey, E. Bonet, R. A. Buhrman, and D. C. Ralph, Phys. Rev. Lett. 89, 196801 (2002).
- [127] S. Urazhdin, N. O. Birge, W. P. Pratt, Jr., and J. Bass, Phys. Rev. Lett. 91, 146803 (2003).
- [128] S. Urazhdin, H. Kurt, J. W. P. Pratt, and J. Bass, Appl. Phys. Lett. 83, 114 (2003).
- [129] J. Bass, S. Urazhdin, N. O. Birge, and W. P. P. Jr., Physica Status Solidi (a) 201, 1379 (2004).
- [130] I. N. Krivorotov, N. C. Emley, A. G. F. Garcia, J. C. Sankey, S. I. Kiselev, D. C. Ralph, and R. A. Buhrman, Phys. Rev. Lett. 93, 166603 (2004).
- [131] A. Brataas, Y. V. Nazarov, and G. E. W. Bauer, Phys. Rev. Lett. 84, 2481 (2000).
- [132] J. Slonczewski, J. Magn. Magn. Mater. 247, 324 (2002).

- [133] J. Xiao, Ph.D. thesis, Georgia Institute of Technology, 2006.
- [134] J. Xiao, A. Zangwill, and M. Stiles, The European Physical Journal B 59, 415 (2007).
- [135] A. Fert, V. Cros, J. M. George, J. Grollier, H. Jaffrs, A. Hamzic, A. Vaurs, G. Faini, J. B. Youssef, and H. L. Gall, J. Magn. Magn. Mater. 272-276, 1706 (2004).
- [136] J. Barnas, A. Fert, M. Gmitra, I. Weymann, and V. K. Dugaev, Phys. Rev. B 72, 024426 (2005).
- [137] P. M. Haney, D. Waldron, R. A. Duine, A. S. N. nez, H. Guo, and A. H. MacDonald, Phys. Rev. B 76, 024404 (2007).
- [138] P. Monod and S. Schultz, J. de Physique 43, 393 (1982).
- [139] Constitution of Binary alloys, 2nd ed., edited by M. Hanson (McGraw hill, New York, 1958), p. 585.
- [140] Q. Fowler, B. Richard, A. Sharma, N. Theodoropoulou, R. Loloee, W. P. Jr., and J. Bass, J. Magn. Magn. Mater. (In Press).
- [141] P. B. Visscher and D. M. Apalkov, J. Appl. Phys. 97, 10C704 (2005).
- [142] S. Urazhdin, N. O. Birge, J. W. P. Pratt, and J. Bass, Appl. Phys. Lett. 84, 1516 (2004).
- [143] H. Kurt, R. Loloee, W. P. Pratt, Jr., and J. Bass, J. Appl. Phys. 97, 10C706 (2005).
- [144] N. C. Emley, I. N. Krivorotov, O. Ozatay, A. G. F. Garcia, J. C. Sankey, D. C. Ralph, and R. A. Buhrman, Phys. Rev. Lett. 96, 247204 (2006).
- [145] L. Berger, J. Magn. Magn. Mater. 278, 185 (2004).
- [146] J. Hamrle, T. Kimura, T. Yang, and Y. Otani, Phys. Rev. B 71, 094434 (2005).
- [147] D. M. Edwards, F. Federici, J. Mathon, and A. Umerski, Phys. Rev. B 71, 054407 (2005).
- [148] Z. Wei, J. Basset, A. Sharma, J. Bass, and M. Tsoi, J. Appl. Phys. (In Press)
- [149] J. Bass, A. Sharma, Z. Wei, and M. Tsoi, J. of Magnetics (The Korean Magnetics Society) 13, 1 (2008).
- [150] W. H. Meiklejohn and C. P. Bean, Phys. Rev. 102, 1413 (1956).
- [151] H. Ohldag, A. Scholl, F. Nolting, E. Arenholz, S. Maat, A. T. Young, M. Carey, and J. Stöhr, Phys. Rev. Lett. 91, 017203 (2003).

- [152] A. Scholl, M. Liberati, E. Arenholz, H. Ohldag, and J. Stöhr, Phys. Rev. Lett. 92, 247201 (2004).
- [153] J. Nogus and I. K. Schuller, J. Magn. Magn. Mater. 192, 203 (1999).
- [154] A. E. Berkowitz and K. Takano, J. Magn. Magn. Mater. 200, 552 (1999).
- [155] H. Gomonay and V. Loktev, arXiv.org:0709.4172 (2007).
- [156] Y. Xu, S. Wang, and K. Xia, Phys. Rev. Lett. 100, 226602 (2008).
- [157] S. Urazhdin, C. L. Chien, K. Y. Guslienko, and L. Novozhilova, Phys. Rev. B 73, 054416 (2006).
- [158] H. Mehrer, N. Stolica, and N. A. Stolwijk, in *Diffusion in Solid Metals and Alloys*, edited by H. Mehrer (Landolt-Bornstein New Series, Group III, Springer, Berlin, New york, 1990).